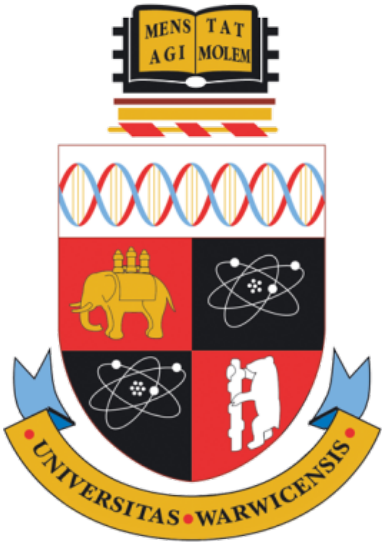

Measurement of the Neutrino-Proton Neutral Current Elastic Cross Section Using the ND280 Detector

by

Aaron Knight

Thesis

Submitted to the University of Warwick

for the degree of

Doctor of Philosophy

Physics

September 2018

Contents

List of Tables **v**

List of Figures **vii**

Acknowledgments **xi**

Declarations **xiii**

Abstract **xiv**

Chapter 1 Neutrino Oscillation Physics **1**

1.1 The Standard Model 1
1.2 A (Brief) History of Neutrino Physics 2
1.2.1 The Solar Neutrino Problem 4
1.2.2 The Atmospheric Problem 5
1.2.3 Experimental Confirmation of Neutrino Oscillations 5
1.3 Neutrino Oscillation Phenomenon 6
1.3.1 Derivation of the Neutrino Oscillation Probability 7
1.3.2 Matter Effects 9
1.4 Mass Hierarchy 10
1.5 Charge-Parity Violation in the Leptonic Sector 11
1.6 Summary of Neutrino Oscillation Measurements 12
1.6.1 Atmospheric Experiments 12
1.6.2 Reactor Experiments 13
1.6.3 Long Baseline Results 14
1.6.4 Short Baseline Neutrino Experiments 16

1.6.5 Future Neutrino Oscillation Experiments . . . 16
1.6.6 Current Knowledge of Oscillation Parameters . . . 17

Chapter 2 Neutrino Interactions **19**
2.1 The Weak Interaction . . . 19
2.1.1 The Glashow-Weinberg-Salam Theory . . . 20
2.1.2 The Structure of Weak Interactions . . . 21
2.2 Neutrino Interaction Processes . . . 22
2.2.1 Neutrino-Lepton Interactions . . . 23
2.2.2 Neutrino-Nucleon Interactions . . . 24
2.2.3 Nuclear Effects . . . 31
2.3 Generators . . . 34
2.3.1 GENIE . . . 35
2.3.2 NEUT . . . 36
2.3.3 NuWro . . . 36
2.3.4 NUANCE . . . 37
2.3.5 GiBUU . . . 37

Chapter 3 Neutral Current Elastic Interactions **38**
3.1 Weak Neutral Currents . . . 38
3.2 Neutral Current Elastic Interaction on a Free Proton . . . 39
3.3 The Proton Spin Crisis . . . 42
3.3.1 The Strange Form Factors . . . 43
3.3.2 Measuring Δs via the NCE Neutrino-Nucleon Interaction . . . 44
3.4 Neutral Current Elastic Data . . . 45

Chapter 4 The T2K Experiment **49**
4.1 Tokai To Kamioka . . . 49
4.1.1 Overview of T2K . . . 49
4.1.2 The Beamline . . . 50
4.1.3 The Near Detectors . . . 54
4.1.4 Super-Kamiokande . . . 62
4.1.5 Cherenkov Radiation . . . 62
4.1.6 Detector Design . . . 63
4.1.7 Background Reduction . . . 65

4.1.8 Super-Kamiokande Events . . . 66
4.2 The Ageing of ND280's Electromagnetic Calorimeter . . . 67
4.2.1 The Physics of Scintillators . . . 67
4.2.2 Analysing the Degradation of the ECal Scintillator Response . . . 69
4.2.3 Extrapolating Results to Predict the Response of the ECal in the Future . . . 73
4.2.4 Correcting for the Scintillator Degradation . . . 75
4.2.5 Conclusion . . . 75

Chapter 5 Measuring the NC0π Cross Section **78**
5.1 Cross Section Extraction . . . 79
5.2 Implementation . . . 80
5.2.1 Input Data and MC . . . 80
5.2.2 Python Analysis Package . . . 80
5.2.3 HighLAND 2 Software . . . 81
5.2.4 Corrections . . . 82
5.3 Event Generator Studies . . . 83
5.4 Samples . . . 83
5.4.1 Signal Sample . . . 83
5.4.2 Control Samples . . . 90
5.4.3 Data/MC Agreement in the Control Samples . . . 93
5.5 Evaluation of Systematics . . . 93
5.5.1 Flux Systematic . . . 93
5.5.2 Detector Systematics . . . 95
5.5.3 Theory Systematics . . . 100
5.5.4 Signal Efficiency . . . 103
5.5.5 Sideband Efficiencies . . . 105
5.5.6 Summary of Systematics . . . 107
5.6 Fitting Procedure . . . 107
5.7 Results . . . 109
5.7.1 Future Developments . . . 110

Chapter 6 Conclusion **112**

Appendix A Independent ECal Ageing Study **113**
A.1 Control Samples 113
A.2 Analysis Method 113
A.3 Results 115

Appendix B Fit Parameters **118**
B.1 Pre-Fit Parameters Table 118
B.2 Post-Fit Parameters Table 120
B.3 Description of the Fit Parameters 122

List of Tables

1.1 Oscillation parameters from global fits to multiple data sets [41]. 17

3.1 The strange form factor parameters extracted from a global fit to neutrino and electron scattering data provided by the BNL E734m HAPPEx, SAMPLE, G0 and PVA4 experiments [82]. 44

4.1 Parameters of the J-PARC main ring fast extraction. 51
4.2 The gas composition of the Time Project Chambers (TPCs) used in ND280. 56
4.3 A brief overview of ND280's ECals. 59

5.1 Table of the number of nucleons in the FGD 1 fiducial volume used in this analysis. 79
5.2 Table of MC POT used in this analysis. Water refers to the P0D water bags being filled with water and air refers to them being empty. 80
5.3 Table of purities by interaction topology. 88
5.4 Table of purities by interaction topology for the P0D sample. 92
5.5 Table of purities by interaction topology for the SMRD sample. 93
5.6 The binning used for the beam flux systematic in neutrino mode. 95
5.7 Evaluation of the efficiency of number of bunches passing each veto cut used to calculate the pile up systematic. 100
5.8 The signal efficiencies for the GENIE sample and NuWro samples. 104
5.9 The signal efficiencies for the GENIE sample and NuWro samples. 104
5.10 The efficiencies for the SMRD control sample for data and MC evaluated using cosmic muons. 106

5.11 The efficiencies for the SMRD control sample for data and MC evaluated using sand muon. 106
5.12 Table of total systematics for the signal sample in the NCE analysis which are added in quadrature. 107
5.13 Table of detector systematics for each sample in the NCE analysis. 107
5.14 Total number of events for each sample in the analysis in data as well as MC before and after fitting. These numbers include signal as well as background. 109
5.15 The errors which contribute to the NCE cross section measurement broken down by each uncertainty. 110

A.1 A summary of the y-offset and decay constant taken from the exponential fits for all ECal modules. 117

B.1 Table of the values and their errors for each parameter used in the fit before the fitting procedure has been carried out. 119
B.2 Table of the values and their errors for each parameter used in the fit after the fitting procedure has been carried out. 121
B.3 A description of each parameter used in the fitting procedure. 123

List of Figures

1.1 The particle content of the Standard Model of particle physics. Reproduced from Wikipedia.org [1]. 2

1.2 Variation in hadron production cross section around the Z^0 mass as a function of the number of active neutrino species [8] 4

1.3 Feynman diagrams of both charged current (1.3a) and neutral current (1.3b) interactions. 10

1.4 The two possible mass hierarchies depicted graphical with normal hierarchy on the left and inverted on the right [19]. 11

1.5 Left: 90% and 99% C.L. regions from T2K (blue lines) and NOνA (red lines) data, from the atmospheric Super-K results (green lines) and from the global fit of all the oscillation experiments (coloured regions). The star indicates the best fit point from the global analysis for normal mass ordering, while the black dot indicates the local minimum for inverted mass ordering. Right: $\Delta\chi^2$ profile as a function of the CP phase δ from T2K, NOνA and Super-K atmospheric and from the global fit (magenta line). The upper panels correspond to normal mass ordering while the lower panels show the results for inverted mass ordering. Taken from [41]. 18

2.1 A muon-neutrino interacting with an electron via the neutral current elastic channel. 23

2.2 ν_μ CC cross section data plotted as a function of neutrino energy on different targets. Also plotted is the prediction for the same interaction on a free nucleon with the value of M_A assumed to be 1.0 GeV. Plot taken from [51]. 24

2.3 $\bar{\nu}_\mu$ CC cross section data plotted as a function of neutrino energy on different targets. Also plotted is the prediction for the same interaction on a free nucleon with the value of M_A assumed to be 1.0 GeV. Plot taken from [51]. 25
2.4 The charged current quasi-elastic (CCQE) interaction. 25
2.5 The MiniBooNE data with the CCQE double differential cross section in Muon angle and energy predictions from different models. Plot from [60]. . 28
2.6 Resonant pion production from a charged current interaction. 30
2.7 Fermi momentum as a function of radial distance within a carbon nucleus for both the global and local RFG models. Plot taken from [5]. 33

3.1 The neutral current elastic neutrino-proton interaction 40
3.2 BNL E734 neutral current elastic differential cross section as a function of Q^2 in both neutrino and anti-neutrino modes. Plot taken from [80]. 45
3.3 The allowed regions at a 67% and a 90% confidence level for the value of M_A and η found by the BNL E734 experiment from the χ^2 fit of the MC prediction to the neutrino and anti-neutrino cross section data. Plot taken from [80]. 46
3.4 The MiniBooNE differential NCE cross section on CH_2 as a function of Q^2_{QE} with NCE-like background which has been subtracted. Plot taken from [84]. 47
3.5 MiniBooNE NCE/CCQE cross section ratio on CH_2 as a function of Q^2. Plot taken from [84]. 48

4.1 A diagram showing the T2K experiment from J-PARC to Super-Kamiokande. Diagram taken from [85] 50
4.2 Predicted flux for different off-axis angles, and the muon neutrino survival probability at 295 km [85]. 51
4.3 Overview of the T2K neutrino beamline showing fast extraction. Diagram taken from [85]. 52
4.4 A side view of the T2K secondary beamline. Diagram taken from [85]. . . 53
4.5 Exploded schematic of ND280 showing how the sub-detectors within it are arranged. 54
4.6 A schematic of a TPC used in ND280. Taken from [88]. 57
4.7 Schematic showing the composition of the π^0-detector reproduced from [91]. 58
4.8 Schematic of INGRID showing module configuration. Taken from [85]. . . 61

4.9 Schematic of Super-Kamiokande, taken from [85]. 64
4.10 Event displays showing (a) an electron neutrino and (b) a muon neutrino event in SK. Event displays taken from the Super-Kamiokande public website [96]. 67
4.11 A schematic showing a charged particle traversing several scintillator bars within an ECal module. 69
4.12 The Landau-Gaussian distribution of recorded charge deposited within a scintillator bar. The red line is the best fit to the data (blue line) with the Landau-Gaussian model. 71
4.13 The MPV from the Landau-Gaussian distribution fitted to the charge distributions as a function of time. Here the the x, y and z labels in the titles for the Barrel ECal plots refer to the orientation of the bar in the global ND280 co-ordinate system. The uncertainty on each data point is calculated using equation 4.5. The blue line fitted to the data points is an exponential function given in equation 4.4 and is used to characterise the degradation of the scintillator bar. 72
4.14 The exponential fits for the ageing extrapolated up to 2030. The green band shows a 68% confidence interval on this extrapolation and the yellow band shows a 95% confidence interval. 74
4.15 The corrected data (red) as a function of time for the ECal plotted by bar type. 76

5.1 The differential cross section as a function of Q^2 for CCQE and NCE interactions with 1 and 2 protons in the final state. The red line shows the prediction of the nominal model in NuWro whereas the green line is the TEM implemented in NuWro. 84
5.2 TPC proton pull for different particle types. The red arrows show the range in which tracks are accepted as being proton-like. The plot is POT normalised. 86
5.3 TPC muon pull plotted by different particle types. The red arrow shows where the cut is applied. 87
5.4 The muon decay process. 87
5.5 Plots showing how the purity and the efficiency of the signal sample evolves with each cut 89

5.6 Proton kinematics and $\cos\theta$ plots after all cuts for the signal sample 89
5.7 MC timing information for true signal events and true OOFV neutrons which dominate the background in the signal sample. 90
5.8 Proton kinematics and $\cos\theta$ plots after all cuts for the P0D sample 91
5.9 Proton kinematics and $\cos\theta$ plots after all cuts for the SMRD sample . . . 92
5.10 Each point shows measurements by a single TPC of the energy loss and momentum of positively charged particles produced in neutrino interactions. The expected relationships for muons, positrons, protons, and pions are shown by the curves. Figure taken from [85] 96
5.11 GEANT4 validation plots used to motivate the neutron secondary interaction systematic. Data from the Dubna and IHEP experimental databases is compared to different cross section models in the GEANT4 package. Plots taken from T2K technical note 131 [106]. 101

A.1 Total charge deposited per track length plotted for the bottom right barrel module including cosmic muon data from runs 2-4. 114
A.2 Scintillator ageing result for the DS ECal. 115
A.3 Scintillator ageing plots for the barrel ECal. 116

Acknowledgments

To begin with I would like to thank my supervisors, Prof. Gary Barker and Dr. Steve Boyd, for their support during my time at Warwick. The advice and guidance you have given me over the last four years has helped me grow as a physicist while ensuring all my work is completed on time. I would also like to thank Dr. David Hadley for all the help you have given me, your knowledge and expertise has been invaluable throughout my PhD. To everyone else who I have had the pleasure of sharing office P450 with over the last four years and the rest of the Elementary Particle Physics Group at Warwick, you all created such a wonderful environment to work and learn in.

Past and present T2K collaborators, your efforts to produce high quality physics has been inspirational. Without the expertise of so many who have spent years designing and building the experiment, developing the software, performing service tasks and analyses, and taking physics data, my PhD would not have been possible. I would like to give special thanks to those collaborators who I spent time with on my long term attachment in Tokai for a T2K data taking run. The entertainment you provided was a welcome distraction from work and made the experience more enjoyable. I must not forget the residents of Tokai who have endured numerous T2K collaborators descending on their village over the years and have made us all feel so very welcome. I will dearly miss my lunch time visits to "station ramen" and nights spent in Pono Pono, along with all the other restaurants in which I ate far too much delicious food and drank far too irresponsibly.

I must now thank those who have supported me outside of physics. My mother

and father, Sharon and Paul, who have supported me throughout my life no matter what, along with my two brothers, Glen and Craig. Without the sacrifices you have made to ensure I get the best possible opportunities in life, I would not be where I am today.

My partner, Lauren, for making sure I took time for myself when I needed it, ensuring that I stayed motivated and for convincing me to get our dog, Haku, the Shiba-Inu, who is simultaneously a comfort and a nuisance.

To my friends at home in Portsmouth who, no matter how long it has been since we have seen each other, have always been there for me. You all have refused to change over the last decade and provide me with a constant in life.

Finally, to everyone who I have shared accommodation with over the last four years who have made living in Coventry bearable and, on occasion, enjoyable.

Declarations

The material presented in this thesis has not been submitted for examination at another institute nor has it been published elsewhere. My own work is presented unless stated otherwise.

Chapter 4 gives a description of the T2K experiment. Since it was formed the T2K collaboration has been contributed to by hundreds of people from a number of different countries. One of the tasks that I have performed on T2K is a study into the ageing of the electromagnetic calorimeters which I collaborated on with a former University of Lancaster PhD student, Iain Lamont. I also worked closely with the calibration group implementing an algorithm to correct for the degradation of the electromagnetic calorimeters seen in the study.

In chapter 5 my physics analysis is presented which is my own work which I collaborated on with Dr. David Hadley. However, this work makes use of the HighLAND 2 software framework developed by others within the T2K collaboration and includes systematics evaluated by previous analysers. The analysis also uses systematics evaluated by others that are not contained within the HighLAND 2 software. The P0D efficiency and the neutron secondary interaction systematic were computed by collaborators on T2K.

Abstract

The T2K experiment, based in Japan, is a long baseline neutrino oscillation experiment. It is the charged current quasi-elastic (CCQE) interaction that is the dominant process in the T2K beam line and the collaboration, along with other experiments, have exerted a lot of effort into better understanding the CCQE channel. The neutral current elastic (NCE) channel on the other hand has not been studied by T2K.

Measurements of neutrino cross sections from a number of different experiments that make use of various target materials have shown that our understanding of neutrino interactions is incomplete. There exists tension between data sets for experiments with lighter nuclei as target, such as hydrogen, and those that use heavier nuclei such as carbon. This has led to the existence of the axial mass problem. In order to better understand this, new models known as 2p-2h models have been developed. However, it is unclear which, if any, of these models correctly describe neutrino interactions.

A correct model describing neutrino interactions should be able to successfully model both charged current and neutral current interactions simultaneously. The NCE interaction provides a complimentary measurement to the CCQE channel. Comparing the NCE and the CCQE processes may lead to degeneracy between models being broken and allow for a better understanding of neutrino interactions.

Using ND280's fine-grained detector (FGD) as target, a measurement of the NCE cross section is presented. As ND280 is primarily sensitive to interactions on protons, the NCE interaction is studied by observing the protons that are the product of such a process. The total NCE cross section is reported in this thesis to be $(2.72 \pm 0.41) \times 10^{-40}\text{cm}^2$ nucleon^{-1}.

Chapter 1

Neutrino Oscillation Physics

1.1 The Standard Model

The Standard Model (SM) of particle physics is a theory which describes the fundamental particles found in the Universe. It describes the particles of matter, with half-integer spin called fermions and the particles associated with three of the four fundamental forces; the gravitational force is not part of the SM. The particles associated with the forces have spin 1 and are known as bosons, the Higgs bosons is also included in the SM and has spin 0. Together the fermions and bosons of the SM are able to account for the rich variety of particles observed to date and can describe how these particles interact with one another.

There are twelve fermions in the SM which can be further split into two categories; quarks and leptons. Quarks have color charge and therefore can take part in strong interactions along with both weak and electromagnetic interactions. There are six flavours of quark (as shown in figure 1.1) in the SM which can never observed as free particles due to the asymptotic freedom of the strong force which binds quarks into composite particles known as hadrons. Hadrons can be further categorised into baryons which describe three quarks bound together, and mesons comprised of a quark and anti-quark pair. An example of a baryon would be a proton which is made up of two up quarks and a down quark.

There are also six leptons within the SM, three of which carry electrical charge: the electron, the muon and the tau. There are also three leptons which are electrically neutral: the electron neutrino, the muon neutrino and the tau neutrino. Leptons do no carry color charge and therefore are unable to participate in strong interactions. All flavours of lepton can interact via the weak nuclear force which will be discussed in greater detail in

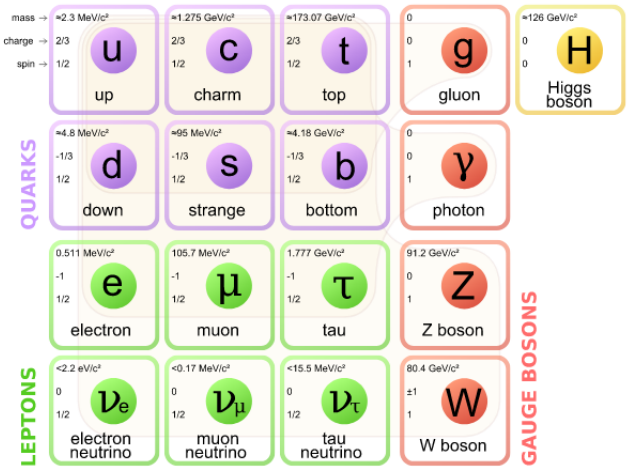

Figure 1.1: The particle content of the Standard Model of particle physics. Reproduced from Wikipedia.org [1].

chapter 2.1 of this thesis.

The neutrino in the SM is a massless particle but as will be seen in the following chapter a massless neutrino cannot undergo flavour oscillations - a phenomenon in which a neutrino changes flavour as it propagates - as it requires the different neutrino weak states to have different masses. The neutrino must therefore have a non-zero mass to allow for flavour oscillations to occur.

1.2 A (Brief) History of Neutrino Physics

During the early part of the 20th century, scientists began to understand the properties of radioactivity and demonstrated that three types of radioactive decay can occur: α, β and γ. It was the energy spectra of the β particle which became a worrying problem for physicists; as nuclei underwent this decay process, only two particles appeared to be produced and energy conservation appeared to be violated. The energy of the emitted electron was able to take any value between 0 and some maximum value, Q_{max}, resulting in energy being unaccounted for.

In 1930, in an attempt to solve this problem, Austrian physicist, Wolfgang Pauli, first hypothesised the existence of a particle which could explain beta-decay while conserv-

ing energy. Pauli's particle had a very small mass, was electrically neutral and a very small cross section making it incredibly difficult to detect. In December 1930 Pauli penned a letter to a group of physicists in Tübingen in which he admitted that his solution seemed "improbable" and described it as a "desperate remedy" [2].

Four years later, Enrico Fermi, as part of his theory on weak interactions, proposed his own version of Pauli's "desperate remedy" calling it the neutrino, deriving its name from the Italian for "little neutral one". A key difference between the two particles is that Fermi's neutrino was not a nuclear constituent but is a product of β-decay [3] and it is this neutrino which is part of the Standard Model.

The first indirect detection of neutrinos came in 1956 by Cowan and Reines at the Savanna River Reactor experiment in South Carolina [4]. Anti-neutrinos were detected from inverse beta decay, as shown in equation 1.1, which occurred within the nuclear reactor

$$\bar{\nu}_e + p^+ \rightarrow n^0 + e^+. \tag{1.1}$$

Six years later, an experiment at the Brookhaven National Laboratory (BNL) was able to show that the muon neutrino was a distinct particle [6], different to that which had been observed in South Carolina. The experiment used a proton beam to produce pions that were then allowed to decay into a muon and muon neutrino in the decay process $\pi^+ \rightarrow \mu^+ + \nu_\mu$. The neutrinos produced in this decay process were then detected using an aluminium spark chamber.

The third neutrino flavour to be discovered was the tau neutrino in 2000 by the DONUT (Direct Observation of NU Tau) collaboration [7], a particle thought to exist after the discovery of the tau lepton in 1974. The detection method was to look for muon-like tracks produced in neutrino interactions which contained a kink close to the interaction vertex. This kink was interpreted to be the production of a tau lepton (which would have been produced with a tau neutrino) which subsequently decayed into a muon and hence confirming the existence of the tau neutrino.

Measurements of the Z-width [8] lead to the conclusion that, for $m_\nu < \frac{1}{2}m_Z$, there are only three flavours of neutrino which can couple to the weak interaction vertex as shown in figure 1.2. However, this does not mean that there are only three neutrino flavours. Further neutrino flavours are possible, so called sterile neutrinos, but these would be unable to take part in weak interactions.

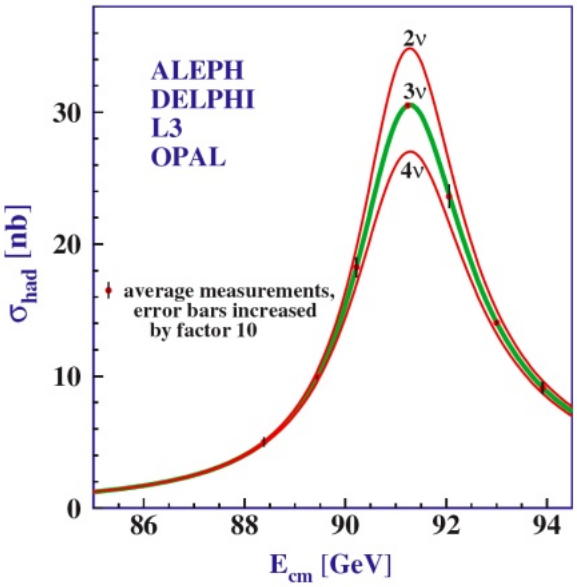

Figure 1.2: Variation in hadron production cross section around the Z^0 mass as a function of the number of active neutrino species [8]

1.2.1 The Solar Neutrino Problem

Using the Standard Solar Model [9] it is possible to predict the expected flux of electron neutrinos on Earth which are produced in nuclear reactions within the Sun. During the late 1960s the Homestake Experiment (sometimes referred to as the Davis Experiment) set out to experimentally measure the solar neutrino flux via a radiochemical method [10]; a large tank of pure C_2Cl_4 was used as target and detected neutrinos captured via the reaction

$$^{37}\mathrm{Cl} + \nu_e \rightarrow {}^{37}\mathrm{Ar} + e^- \tag{1.2}$$

Approximately once a month helium would be bubbled through the target material in order to remove the argon atoms produced by the neutrino interactions. As they decayed they were counted, thereby allowing the electron neutrino flux to be determined.

The Homestake Experiment found that the solar neutrino flux did not agree with the theoretically predicted flux; approximately one third of the expected flux was measured. The experiment ran until 1994, during its operational lifetime it was subject to

many improvements in order to find the origin of the disagreement between theory and data but no cause was found. After 24 years of data taking it was concluded that the measured solar neutrino flux was one third of the theoretically predicted flux; a disagreement which became known as the Solar Neutrino Problem. Other experiments such as SAGE [11] and GALLEX [12] were designed to detect solar neutrinos at lower energies but higher flux by using gallium as target. These experiments reported a smaller deficit in their observations suggesting the phenomenon had an energy dependence. Physically motivating a non-standard solar model to explain this energy-dependent deficit was a fruitless endeavour. The only idea left was that the neutrinos were changing flavour as they propagated between the Sun and the detectors on Earth, a phenomenon first predicted by Pontecorvo in 1957 [13] and now referred to as neutrino flavour oscillations.

1.2.2 The Atmospheric Problem

In addition to experiments measuring the flux of solar neutrinos, experiments such as the Super-Kamiokande (SK) experiment in Japan, set out to also measure neutrinos produced within Earth's atmosphere. Cosmic rays collide with Earth's upper atmosphere producing showers of various particles which decay into muons and the associated muon neutrino.

The ratio of muon neutrino to electron neutrino events were measured as a function of zenith angle; determination of the angle with respect to the zenith angle can be used to figure out the baseline over which the neutrino has travelled. A double ratio of the predicted rate to the expected rate for each flavour of neutrino was used in order to cancel systematic uncertainties. It was found that, when compared to the expected rate, the measured rate was lower than predicted, an indication that either muon neutrinos are disappearing or electron neutrinos are appearing and became known as the Atmospheric Neutrino Anomaly. Super-Kamiokande was also able to show that the flux varied as a function of zenith angle.

1.2.3 Experimental Confirmation of Neutrino Oscillations

A large water Cherenkov detector known as the Sudbury Neutrino Observatory (SNO) experiment containing 1,000 tonnes of heavy water, D_2O, was able to experimentally show that neutrinos underwent flavour oscillations by comparing the observed solar neutrino flux in the charged current (CC) and neutral current (NC) channels [14]. For discussions on charged current and neutral current interactions see sections 2.2.2.1 and 3.2 respectively.

A solar neutrino of flavour α interacts with a deuterium atom in the water producing a neutrino of flavour α, a proton and a neutron via the reaction

$$\nu_\alpha + {}^2\mathrm{D} \rightarrow \nu_\alpha + p + n \tag{1.3}$$

It is then possible for the neutron produced in this interaction to interact with another deuterium atom producing a tritium atom and a 6.3 MeV photon shown below

$$n + {}^2\mathrm{D} \rightarrow {}^3\mathrm{T} + \gamma \tag{1.4}$$

The SNO experiment was able to identify that a neutral current interaction had occurred by detecting the photon emitted when the neutron was captured.

Neutral current interactions are flavour independent; a neutrino of any flavour is able to take part in the interaction. This allows for the total solar neutrino flux to be determined. The heavy water used as SNO's target material only contains electrons with no muons or taus present. This means that only electron neutrinos are able to contribute to the CC signal. The measured solar neutrino flux in the NC channel matched what theory predicted however the CC channel still showed the deficit [15] which had been observed in previous experiments. This was taken to be confirmation that the flavour eigenstate of a neutrino changes as the neutrino propagates. This was then verified by SK, a discovery which won Arthur B. McDonald and Takaaki Kajita the 2015 Nobel Prize in Physics [16].

1.3 Neutrino Oscillation Phenomenon

As mentioned, the SM neutrino is a massless particle with flavour states identical to its mass states. However, as will be seen, it is not possible for this massless neutrino to undergo flavour oscillations. Instead, it is proposed that the flavour eigenstates exist as a superposition of mass eigenstates, described by equation 1.5, an idea originally theorised by Pontecorvo.

$$\begin{pmatrix} \nu_e \\ \nu_\mu \\ \nu_\tau \end{pmatrix} = U_{PMNS} \begin{pmatrix} \nu_1 \\ \nu_2 \\ \nu_3 \end{pmatrix} \tag{1.5}$$

Where U_{PMNS} is the 3 by 3 unitary rotation matrix called the Pontecorvo-Maki-Nakagawa-Sakata Matrix [17]. It is possible to parameterise the U_{PMNS} it terms of three mixing angles

$(\theta_{12}, \theta_{23}, \theta_{13})$ and phase which violates charge-parity (CP) conservation, δ_{CP}.

$$
\begin{aligned}
U_{PMNS} &= \begin{pmatrix} U_{e1} & U_{e2} & U_{e3} \\ U_{\mu 1} & U_{\mu 2} & U_{\mu 3} \\ U_{\tau 1} & U_{\tau 2} & U_{\tau 3} \end{pmatrix} \\
&= \overbrace{\begin{pmatrix} 1 & 0 & 0 \\ 0 & c_{23} & s_{23} \\ 0 & -s_{23} & c_{23} \end{pmatrix}}^{\text{Atmospheric}} \overbrace{\begin{pmatrix} c_{13} & 0 & s_{13}e^{-i\delta_{cp}} \\ 0 & 1 & 0 \\ -s_{13}e^{i\delta_{cp}} & 0 & c_{13} \end{pmatrix}}^{\text{Reactor/Accelerator}} \overbrace{\begin{pmatrix} c_{12} & s_{12} & 0 \\ -s_{12} & c_{12} & 0 \\ 0 & 0 & 1 \end{pmatrix}}^{\text{Solar}}
\end{aligned} \tag{1.6}
$$

Where the following notation has been adopted:

$$
\begin{aligned}
s_{\alpha\beta} &= \sin\theta_{\alpha\beta} \\
c_{\alpha\beta} &= \cos\theta_{\alpha\beta}
\end{aligned} \tag{1.7}
$$

where $\theta_{\alpha\beta}$ denotes the mixing angles with α, $\beta = 1, 2$ or 3 and $\alpha \neq \beta$. The mixing angles used to parameterise the matrix are determined by measurements using solar, reactor/accelerator or atmospheric neutrinos and is common to describe each component in terms of these different regimes.

If neutrinos are their own anti-particles, a type of particle known as Majorana particles, two extra phases, α_1 and α_2, are needed. A fourth matrix is then needed in equation 1.6 given below

$$
U_{Majoranna} = U_{PMNS} \times \begin{pmatrix} 1 & 0 & 0 \\ 0 & e^{i\alpha_1/2} & 0 \\ 0 & 0 & e^{i\alpha_2/2} \end{pmatrix} \tag{1.8}
$$

These Majorana phases do not effect the oscillation probability and so therefore will not be discussed further.

1.3.1 Derivation of the Neutrino Oscillation Probability

Neutrinos are created in weak (flavour) eigenstates denoted by ν_α along with their associated lepton, α. If a neutrino is produced at position $\vec{x} = 0$ at time $t = 0$ then there is some probability that it will have oscillated into a neutrino of flavour β, ν_β, when it is

detected at some later time. In the following discussion the probability for a neutrino to have oscillated will be derived (in natural units so that $c = \hbar = 1$).

Assuming mixing, the neutrino flavour eigenstate, ν_α, can be expressed as a superposition of its mass eigenstates, ν_i, in bra-ket notation

$$|\nu_\alpha\rangle = \sum_i U_{\alpha i}|\nu_i\rangle \tag{1.9}$$

Propagating the neutrino as a free particle, its evolution is described by the time-dependent Schrödinger equation

$$i\frac{d}{dt}|\psi_i(t)\rangle = H|\psi_i(t)\rangle \tag{1.10}$$

The simplest solution to equation 1.10 is the mass states propagate as plane waves

$$|\nu_i(t)\rangle = e^{-iE_i t}|\nu_i(0)\rangle \tag{1.11}$$

Unitarity of the mixing matrix, U, implies that

$$|\nu_i\rangle = \sum_\alpha U^*_{\alpha i}|\nu_\alpha\rangle \tag{1.12}$$

Substituting 1.12 into 1.9 results in

$$|\nu_\alpha(t)\rangle = \sum_\beta \left(\sum_i U^*_{\alpha i} e^{-iE_i t} U_{\beta i}|\nu_\beta\rangle \right) \tag{1.13}$$

Defining a transition amplitude from a neutrino of flavour α to flavour β as

$$\begin{aligned} A(\nu_\alpha \to \nu_\beta) &= \langle \nu_\beta(t)|\nu_\alpha(0)\rangle \\ &= \sum_i U^*_{\alpha i} U_{\beta i} e^{-iE_i t} \end{aligned} \tag{1.14}$$

Using this definition of the transition amplitude the probability of a flavour oscillation occurring can be written as

$$P\left(\nu_\alpha \to \nu_\beta\right) = \left|A\left(\nu_\alpha \to \nu_\beta\right)\right|^2 \tag{1.15}$$

Leading to the equation

$$P\left(\nu_\alpha \to \nu_\beta\right) = \sum_{i,j} U^*_{\alpha i} U_{\beta i} U_{\alpha j} U^*_{\beta j} e^{-i(E_i - E_j)t} \tag{1.16}$$

Neutrinos are ultra-relativistic with $|\vec{p}| \gg m_i$. Using this knowledge, the energy of a neutrino can be expressed as

$$E = \sqrt{p^2 + m^2} \approx |p| + \frac{m^2}{2\vec{p}} \tag{1.17}$$

Assuming that $p_i = p_j$, the energy difference, $E_i - E_j$, in equation 1.16 can be written in terms of the difference in neutrino mass squared

$$E_i - E_j \approx \frac{m_i^2 - m_j^2}{2|\vec{p}|} = \frac{\Delta m_{ij}^2}{2|\vec{p}|} \tag{1.18}$$

Using the fact that $t = L$ and that $\vec{p} = E$ for ultra-relativistic neutrinos allows for the oscillation probability to be expressed as

$$P\left(\nu_\alpha \to \nu_\beta\right) = \sum_{i,j} U^*_{\alpha i} U_{\beta i} U_{\alpha j} U^*_{\beta j} \exp\left(-i \frac{\Delta m_{ij}^2 L}{2E}\right) \tag{1.19}$$

This expression shows that the probability of an oscillation occurring is dependent on the difference in mass squared, the distance over which the neutrino has to oscillate and the energy of the neutrino. If the SM neutrino is considered it can be seen that the Δm_{ij}^2 term is zero and therefore the probability of an oscillation occurring is also zero. This leads to the conclusion that neutrinos must be massive and have non-zero mass differences between the mass eigenstates for flavour oscillations to be explained.

1.3.2 Matter Effects

Neutrinos are able to take part in both charged current and neutral current interactions, examples of which are pictorially depicted in figure 1.3, and as they propagate they can pass though ordinary matter - matter which contains electrons without muons or taus present. As neutrinos propagate through this electron rich medium they are subjected to matter effects which are a result of coherent interactions; interactions in which the outgoing neutrino is in the same state it was in before the interaction occurred. These interactions

add an effective potential to the Hamiltonian causing the electron neutrino to have an effective mass in the medium it is propagating.

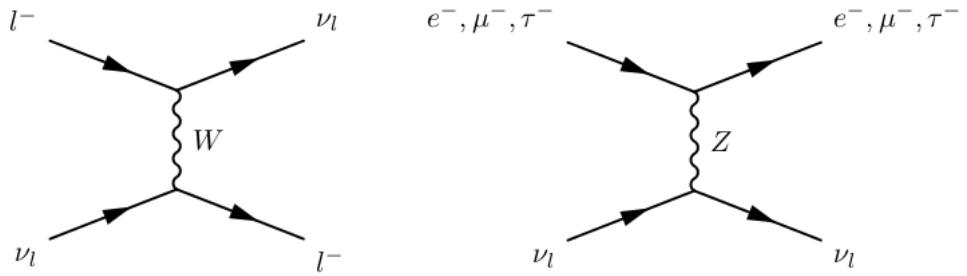

(a) Charged current interaction. (b) Neutral current interaction.

Figure 1.3: Feynman diagrams of both charged current (1.3a) and neutral current (1.3b) interactions.

As NC interactions are flavour independent, all neutrino flavour states are affected, resulting in each neutrino flavour's potential changing by equal amounts. Electron neutrinos however can also interact with the electrons in the matter via the charged current channel again altering the potential further and causing it to feel a different potential when compared to the other flavours. The difference in the potential leads to effective mass-splittings in matter which are different from those in a vacuum and, as the oscillation probabilities are dependent on the mass-splitting, these also are affected [18].

Neutrino oscillations in a vacuum can only provide information about the square of the mass-splitting. Matter effects, on the other hand, allow for measurements of the signs of the mass splittings due to the way they effect the effective mass of the neutrino.

1.4 Mass Hierarchy

Current knowledge of neutrino masses leads to two separate mass hierarchies being possible: "normal" hierarchy and "inverted" hierarchy. A comparison of solar neutrino oscillations with reactor neutrino oscillations shows that ν_2 is more massive than ν_1. The magnitude of the third neutrino mass state, ν_3, on the other hand is presently not known. This means that ν_3 could be the heaviest mass state (normal hierarchy) or it could be lighter than the other two mass states (inverted hierarchy), graphically depecited in figure 1.4.

Determination of the mass hierarchy is of the utmost importance for CP violation

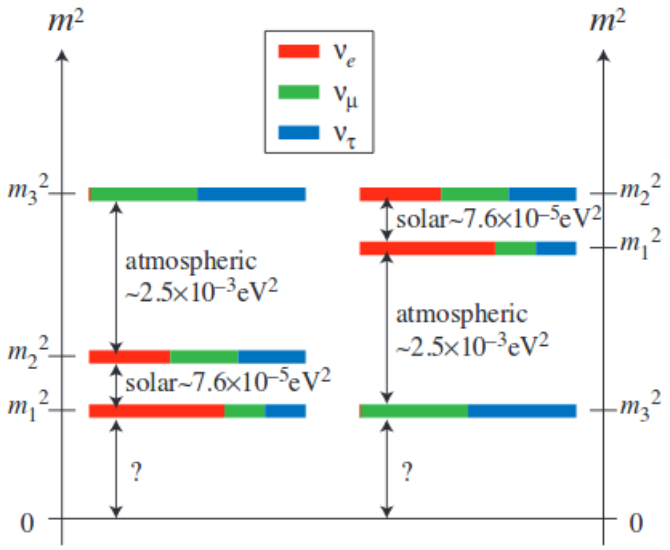

Figure 1.4: The two possible mass hierarchies depicted graphical with normal hierarchy on the left and inverted on the right [19].

searches. Neutrinos and anti-neutrinos feel different matter effects causing an asymmetry in the oscillations that can be misinterpreted as CP violation.

The absolute neutrino mass is still unknown. Neutrino oscillation measurements are sensitive the squared mass difference but do not provide any information about the absolute mass of neutrinos. The absolute neutrino mass scale has been constrained by measurements of the Cosmic Microwave Background (CMB) [20], measurements of the endpoint of the beta decay spectrum [21] as well as observations of neutrino-less double beta decay [22]. An overview of current limits of the neutrino mass is given in reference [23].

1.5 Charge-Parity Violation in the Leptonic Sector

One of the unanswered mysteries of modern physics is why there is a lack of anti-matter seen in the Universe. Cosmological models predict that matter and anti-matter were produced in equal amounts when the Universe was created, however today a matter-anti-matter asymmetry is observed. To explain the absence of anti-matter certain conditions must be

met: Baryon number must not be conserved, charge conservation must be violated and finally CP conservation must also be violated. These three conditions must also be met outside of thermal equilibrium [24].

It has been observed that CP symmetry is violated in the quark sector. This has however proved insufficient to explain the matter-anti-matter asymmetry when included in Baryogenesis models. To date, CP violation has not been observed in the leptonic sector, though if observed, could explain why today's Universe is matter dominated. Differences between neutrino and anti-neutrino oscillations would demonstrate leptonic CP violation. As can be seen in equation 1.20 [25], for a small θ_{13} the CP asymmetry, in the absence of matter effects, can be large especially at low neutrino energies.

$$\begin{aligned} \mathcal{A}(\nu_\mu \to \nu_e) &= \frac{P\left(\nu_\mu \to \nu_e\right) - P\left(\bar{\nu}_\mu \to \bar{\nu}_e\right)}{P\left(\nu_\mu \to \nu_e\right) + P\left(\bar{\nu}_\mu \to \bar{\nu}_e\right)} \\ &\approx \frac{\Delta m^2_{21} L}{4E_\nu} \frac{\cos\theta_{23} \sin 2\theta_{12}}{\sin\theta_{23} \sin\theta_{13}} \sin\delta_{CP} \end{aligned} \tag{1.20}$$

1.6 Summary of Neutrino Oscillation Measurements

After neutrino oscillations were verified to be physical phenomenon, a number of experiments were designed and constructed to measure the oscillation parameters. Various methods have been implemented to probe different areas of phase space to gain a greater understanding of neutrino oscillations.

1.6.1 Atmospheric Experiments

Atmospheric neutrino oscillation experiments look for the disappearance of muon neutrinos, which are produced in the decay of pions that are the result of collisions of cosmic rays with nuclei in Earth's atmosphere. This type of experiment is used to measure $\sin^2\theta_{23}$ and Δm^2_{23}, more recently they have been used to constrain the mass hierarchy and the sterile neutrino signal.

One such atmospheric neutrino oscillation experiment is the instrumented cubic kilometer of ice at the south pole named IceCube [26]. The experiment uses Photo-Multiplier Tubes (PMTs) to detect Cherenkov radiation from neutrino interactions in the ice sheet itself. Primarily, IceCube was designed to detect cosmic neutrinos, but it does have the capability to detect those produced in the atmosphere using an area of the ice

sheet which has a higher density of PMTs - a section referred to as DeepCore. The best measurements for neutrinos with reconstructed energies from 5.6 to 56 GeV set limits of $\Delta m^2_{32} = 2.31^{+0.11}_{-0.13} \times 10^{-3}$ eV^2 and $\sin^2\theta_{23} = 0.51^{+0.07}_{-0.09}$. Assuming normal mass hierarchy these results are consistent with the results from accelerator and reactor-based experiments [26]. A planned future upgrade to IceCube called PINGU (acronym for Precision IceCube Next Generation Upgrade) also aims to determine the neutrino mass hierarchy.

1.6.2 Reactor Experiments

As the name suggests, reactor experiments use nuclear reactors as their neutrino source allowing them to have a significant flux of anti-electron neutrinos. Reactor experiments use near and far detectors at various baselines allowing them to effectively reduce uncertainties, a technique also implemented by accelerator based neutrino experiments. These experiments attempt to measure θ_{13} by searching for the disappearance of anti-electron neutrinos.

Double Chooz is one such reactor experiment located in France. It is the successor to the Chooz experiment which, in 1999, published the limit $\theta_{13} < 0.1$ [27] using only a far detector located 1050 m from the reactor. The limit set showed that θ_{13} is small and therefore atmospheric neutrino oscillations could not be caused by $\nu_\mu \rightarrow \nu_e$. The far detector was replaced and an identical near detector was installed at a baseline of 400 m; both detectors contain 8.8 tonnes of gadolinium-doped scintillator surrounded by non-doped scintillator. The experiment's best measurement to date is $\sin^2 2\theta_{13} = 0.09^{+0.032}_{-0.029}$ [28].

The Kamioka Liquid Scintillator Anti-neutrino Detector (KamLAND) [29] was located in the same mine as SK and detected the anti-electron neutrino flux from 56 Japanese reactors with a mean baseline of 180 km. The experiment was also able to make measurements of solar and geo-neutrinos. The experiment stopped taking data and in 2011 a balloon of xenon-doped liquid scintillator was installed into the tank, transforming the experiment into a neutrino-less double beta decay experiment under the name KamLAND-Zen. Using the data taken while operating, it set limits of $\tan^2\theta_{12} = 0.452^{+0.035}_{-0.03}$, $\sin^2 2\theta_{13} = 0.020^{+0.016}_{-0.016}$ and $|\Delta m^2_{21}| = 7.50^{+0.016}_{-0.016}$ [29].

In China the Daya Bay reactor experiment uses six identical detectors, each providing 20 tonnes of gadolinium-doped liquid scintillator as interaction mass and situated within 2 km of six nuclear reactors. The design of the experiment is such that all mea-

surements of event rate are relative and systematic errors can be cancelled. In 2012, Daya Bay published the first evidence of a non-zero θ_{13} mixing angle at 5.2σ. Best results are $\sin^2 2\theta_{13} = 0.0841 \pm 0.0027\,(\text{stat.}) \pm 0.0019\,(\text{syst.})$ and the squared mass difference for normal mass hierarchy $\Delta m^2_{32} = (2.45 \pm 0.06\,(\text{stat.}) \pm 0.06\,(\text{syst.})) \times 10^{-2}$ eV^2 and inverted mass ordering $\Delta m^2_{32} = (-2.56 \pm 0.06\,(\text{stat.}) \pm 0.06\,(\text{syst.})) \times 10^{-2}$ eV^2 [30].

Reactor Experiment for Neutrino Oscillations (RENO) [31] is a South Korean based experiment which also makes use of six reactors. Making use of two identical detectors positioned at flux weighted average baseline of 410 m and 1440 m. Both detectors consist of gadolinium-doped liquid scintillators. Analysis of the data produced a best measurement of $\sin^2 2\theta_{13} = 0.101 \pm 0.08\,(\text{stat.}) \pm 0.010\,(\text{syst.})$ [31].

1.6.3 Long Baseline Results

Artificial neutrino beams generated using accelerators are used in long baseline oscillation experiments to study neutrino flavour oscillations over a distance of a few hundred kilometers. When compared to other neutrino sources, accelerator based neutrino experiments have good control over the beam spectrum. Use of timing-triggers and the time-bunched structure of the neutrino beam allow for accelerator based neutrino experiments to distinguish atmospheric and cosmological backgrounds from the neutrino beam itself, thereby giving good control over these backgrounds.

KEK To Kamioka (K2K) [32] was the first long baseline neutrino oscillation experiment proposed to study neutrino oscillations. With a baseline of 250 km, a ν_μ beam was produced at KEK in Tsukuba, Japan, and directed towards SK which the experiment used as a far detector. As with the reactor experiments, K2K also made use of a near detector, with both near and far detector placed on the beam axis. After five years of data taking between 1999 and 2004, K2K was able to set constraints on the atmospheric parameters, $\sin^2 2\theta_{23}$ and $|\Delta m^2_{32}|$, at 4.2σ. Under the two neutrino hypothesis, the best fit was $\Delta m^2_{23} = 2.8 \times 10^{-3}$ eV^2 with $\sin^2 2\theta_{23} = 1$ [32].

The Main Injector Neutrino Oscillation Search (MINOS) [33] was a long baseline experiment based in the USA. The beam, which is produced at Fermilab using the Main Injector Accelerator, has energy of a few GeV. As with other long baseline experiments, MINOS makes use of two detectors placed in the usual near-far arrangement. The near detector is located around 1 km downstream and has a mass of approximately 980 tons. The far detector is situated in the Soudan Underground Laboratory in Northern Minnesota

and is similar in design to the near detector but is larger in size with a mass of 5.4 kt. The positioning of the two detectors gives the MINOS experiment a baseline of 735 km and it began taking data from the NuMI beam line in 2005 with the capability of running in neutrino and anti-neutrino modes. MINOS set out to measure the atmospheric parameters by searching for the disappearance of ν_μ in the beam and also searched for an indication of a non-zero value for the parameter θ_{13} by looking for the appearance of ν_e. In the three-flavour model, the atmospheric neutrino mass-splitting was measured to be $(2.42 \pm 0.09) \times 10^{-3}$ eV^2 for normal mass ordering, and for inverted mass ordering it was measured to be $-\left(2.48^{+0.09}_{-0.11}\right) \times 10^{-3}$ eV^2 [33].

Tokai to Kamioka (T2K) [34] was the second long baseline experiment, after K2K, to use SK as a far detector but was the first experiment to utilize off-axis placements of the near and far detectors, allowing for a more mono-energetic neutrino spectrum. Located 280m away from the target is the near detector complex housing two near detectors; INGRID the on-axis near detector and ND280 the off-axis near detector. The primary goals for the experiment were to a make a precise measurement of the mixing angle θ_{13} by looking for the appearance of ν_e in a ν_μ beam as well as improving upon the precision of the atmospheric parameters. The T2K experiment is described in greater detail in chapter 4. T2K reported measurements of the parameters θ_{23} and Δm^2_{23} in 2017 assuming normal mass hierarchy and in both neutrino and anti-neutrino mode. The results were $\sin^2\theta_{23} = 0.51^{+0.08}_{-0.07}$ and $\Delta m^2_{32} = 2.53^{+0.15}_{-0.13} \times 10^{-3}$ eV$^2/c^4$ for neutrinos and $\sin^2\bar{\theta}_{23} = 0.42^{+0.25}_{-0.07}$ and $\Delta\bar{m}_{23} = 2.55^{+0.33}_{-0.27} \times 10^{-3}$ eV$^2/c^4$ for anti-neutrinos [34].

NOνA (NuMI Off-axis Neutrino Experiment) [35] is an experiment which also makes use of the NuMI beam which began data taking in early 2014. The 14 kt far detector is located 810 km away at Ash River, Minnesota, and has a similar modular design to the near detector used. Like T2K, NOνA also exploits the off-axis technique for its detector placement giving the experiment a peak neutrino energy of 2 GeV leading to an L/E value of 405 km/GeV at the flux peak which is comparable to T2K. Their most recent published results report $\Delta m^2_{32} = (2.67 \pm 0.11) \times 10^{-3}$ eV^2 and $\sin^2\theta_{23}$ at the two statistically degenerate values $0.404^{+0.030}_{-0.022}$ and $0.624^{0.022}_{-0.030}$ both at the 68% confidence level. They also report disfavouring the inverted mass hierarchy for all values of δ_{CP} [35].

1.6.4 Short Baseline Neutrino Experiments

Between 1993 and 1998 the Liquid Scintillator Neutrino Detector (LSND) operated at the Los Alamos National Laboratory with a baseline of only 31 m. An accelerator was used to produce a beam of $\bar{\nu}_\mu$ up to energies of 53 MeV. It observed a small excess of $\bar{\nu}_e$ events, an observation which is consistent with sterile neutrinos with $\Delta m^2_{sterile} \approx 1$ eV^2. This result has come to be known as the LSND Anomaly [36].

MiniBooNE (Mini Booster Neutrino Experiment) was designed to test the LSND anomaly and look for oscillations at a similar L/E value to the LSND experiment. Making use of the Fermilab Booster accelerator for its neutrino production, MiniBooNE had peak energy of 0.6 GeV and a baseline of around 500 m. It was also able to operate in both polarities - neutrino and anti-neutrino mode. A mineral oil based detector is used to detect Cerenkov radiation from neutrino interactions. After 10 years of running it had observed significant excess at low energies in both modes of running with the anti-neutrino mode agreeing well with the LSND result, however there still exists some tension in the neutrino mode result [37].

1.6.5 Future Neutrino Oscillation Experiments

In the time since the experimental confirmation of neutrino oscillations, a number of experiments have probed the nature of these oscillations and have made precise measurements of the oscillation parameters. There is, however, much more to be learned, which future generation experiments hope to shed light on.

One such experiment is the Hyper-Kamiokande (HK) detector which is a proposed upgrade to SK [38]. HK would be located close to the SK site and would consist of a tank containing a megaton of water instrumented with ultra high sensitive photo-sensors in order to detected Cherenkov radiation. There are a significant number of physicists with expertise and experience using water Cherenkov detectors in neutrino physics and much of the infrastructure already exists. However, like SK, HK would not be able to distinguish between electrons and photons, and would also have a high threshold for reconstructing particles. Like its predecessor, HK would be able to detect neutrinos from different sources and would be able to be used as a far detector for a long baseline oscillation experiment.

T2K Phase 2 is a proposed extension to the data taking period for the T2K experiment [39]. It would allow for a further six years of data to be taken up until 2026 allowing T2K to accumulate a predicted 20×10^{21} protons of target (POT). This POT could be

made possible by an upgrade to the J-PARC beam line and with sufficiently high statistics the sensitivity to CP violation would improve. This phase of data taking would end, ready for the next generation experiment at J-PARC, Tokai to Hyper-Kamiokande (T2HK), with the Main Ring (MR) power upgraded to 1.3 MW.

The Deep Underground Neutrino Experiment (DUNE) is a proposed neutrino oscillation experiment in the USA with a very long baseline of 1300 km which dwarfs all long baseline experiments which have come before it [40]. It plans to measure both the first and second oscillation maxima by using a wide-band neutrino beam allowing it to access shape information to test the three-neutrino paradigm. It is proposed that the far detector for DUNE would be a large liquid argon time-projection chamber (TPC), the technology for which is currently poorly understood. Reconstructing events using this technology would also be a challenge which DUNE would have to overcome due to the high granularity of the detector.

1.6.6 Current Knowledge of Oscillation Parameters

Continued effort to better understand neutrino oscillations from collaborations around the world provide much needed data on the oscillation parameters. Global fits to many different data sets provide the best knowledge of these parameters and are summarised in the table 1.1. Note that NH and IH stand for normal hierarchy and inverted hierarchy respectively. The global results are compared to various experiments in figure 1.5.

Oscillation Parameter	Best Fit ($\pm 1\sigma$)
$\Delta m^2_{21}\left[10^{-5}\ \mathrm{eV}^2\right]$	7.56 ± 0.19
$\lvert\Delta m^2_{31}\left[10^{-3}\ \mathrm{eV}^2\right]\rvert$ (NH)	2.55 ± 0.04
$\lvert\Delta m^2_{31}\left[10^{-3}\ \mathrm{eV}^2\right]\rvert$ (IH)	249 ± 0.04
$\sin^2\theta_{12}/10^{-1}$	$3.21^{+0.18}_{-0.16}$
$\sin^2\theta_{23}/10^{-1}$ (NH)	$4.30^{+0.20}_{-0.18}$
$\sin^2\theta_{23}/10^{-1}$ (IH)	$5.96^{+0.17}_{-0.18}$
$\sin^2\theta_{13}/10^{-1}$ (NH)	$2.155^{+0.090}_{-0.075}$
$\sin^2\theta_{13}/10^{-1}$ (IH)	$2.140^{+0.082}_{-0.085}$
δ/π (NH)	$1.40^{+0.31}_{-0.20}$
δ/π (IH)	$1.40^{+0.26}_{-0.23}$

Table 1.1: Oscillation parameters from global fits to multiple data sets [41].

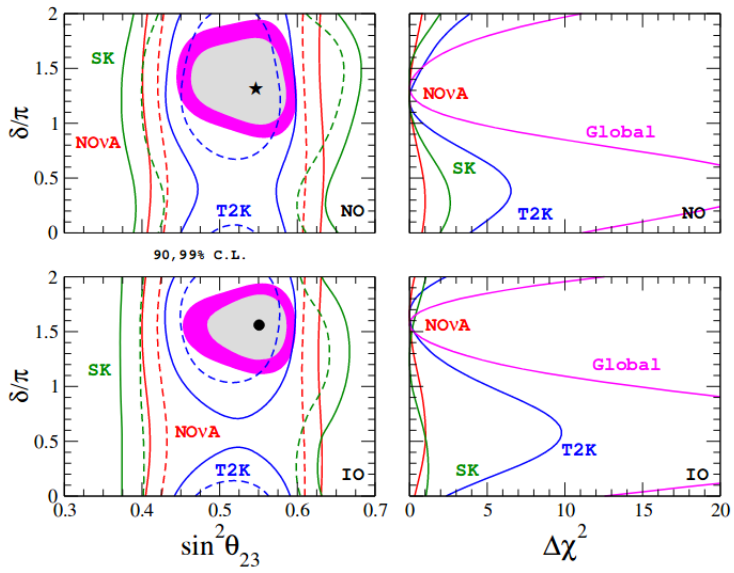

Figure 1.5: Left: 90% and 99% C.L. regions from T2K (blue lines) and NOνA (red lines) data, from the atmospheric Super-K results (green lines) and from the global fit of all the oscillation experiments (coloured regions). The star indicates the best fit point from the global analysis for normal mass ordering, while the black dot indicates the local minimum for inverted mass ordering. Right: $\Delta\chi^2$ profile as a function of the CP phase δ from T2K, NOνA and Super-K atmospheric and from the global fit (magenta line). The upper panels correspond to normal mass ordering while the lower panels show the results for inverted mass ordering. Taken from [41].

Chapter 2

Neutrino Interactions

Neutrinos are leptons which carry no electrical or color charge, allowing them to only take part in weak interactions. To gain an understanding of how neutrinos interact with matter, it is first necessary to understand the weak nuclear force. Understanding the processes through which the neutrino undergoes interactions will allow for better measurements of oscillation parameters to be made, and subsequently allow for a better understanding of the flavour changing phenomenon.

2.1 The Weak Interaction

It was Enrico Fermi who first proposed a theoretical framework for the weak interaction, by describing the beta decay of a neutron with a four-point interaction which was not mediated by a boson. If the particle fields are denoted by Φ it is possible to write down the matrix element for this interaction

$$M_{fi} = G_F g_{\mu\nu} \left[\bar{\Phi}_e \gamma^\mu \Phi_{\bar{\nu}_e}\right] \left[\bar{\Phi}_p \gamma^\nu \Phi_n\right] \tag{2.1}$$

where Φ denotes the particle fields and G_F is the Fermi constant which has been empirically measured from the lifetime of the muon. When the cross section for this interaction is calculated it becomes apparent that it has a problem. Bethe calculated the cross section for $\nu_e + n \to p + e^-$ [42] using Fermi's 4-point interaction model gaining the result

$$\sigma\left(n + \nu_e \to e^- + p\right) \approx E_\nu \left(\text{MeV}\right) \times 10^{-43} \text{ cm}^2 \tag{2.2}$$

The Fermi model predicts an unphysical cross section which increases without limit as a function of the neutrino energy.

2.1.1 The Glashow-Weinberg-Salam Theory

Over a decade later, during the 1960s, the Glashow-Weinberg-Salam (GWS) theory [43; 44; 45] was developed, unifying electromagnetism and the weak nuclear force. It included two charged bosons, W^+ and W^-, which mediates weak charged current (CC) interactions and a third, neutral boson which can be exchanged in weak neutral current (NC) interactions known as the Z^0 boson. At the time, weak neutral currents had not been observed experimentally, and so the prediction of their existence ignited searches for this new interaction mode which would confirm validity of the GWS model. The bosons associated with weak interactions are predicted to have non-zero mass.

The unification of the two fundamental forces is described by the $SU(2)_L \times U(1)_Y$ gauge group: L represents left-handed chirality and Y the hypercharge. The SU(2) gauge group has three gauge bosons represented by W^μ_α where $\alpha = 1, 2, 3$. The U(1) group has one gauge boson, B^μ. The weak currents are

$$\begin{aligned} J^\mu_W &= \bar{u}\frac{-ig_W}{2\sqrt{2}}\left(\gamma^\mu - \gamma^\mu\gamma^5\right)u \\ J^\mu_Z &= \bar{u}\frac{-ig_Z}{2}\left(g_V\gamma^\mu - g_A\gamma^\mu\gamma^5\right)u \end{aligned} \tag{2.3}$$

where J^μ_W and J^μ_Z are the charged and neutral weak currents respectively [46] with the Dirac spinors being denoted by u and $\bar{u}$. The variables g_V and g_A are the vector and axial vector weak couplings respectively and are dependent on the lepton which is involved in the interaction. The weak charge is denoted by g_W for charged current interactions and g_Z for neutral current interactions and are related to the electric charge $e = g_W \sin\theta_W = g_Z \cos\theta_W$.

The charged weak fields are defined to be

$$W^\mu_\pm = \frac{W^\mu_1 \mp iW^\mu_2}{\sqrt{2}} \tag{2.4}$$

These fields are associated with the $W^\pm$ boson which mediates charged current interactions. The theory also included two neutral bosons which are the result of the W^3 and B^μ fields

mixing together

$$\begin{aligned} A_\mu &= B_\mu \cos\theta_W + W^3_\mu \sin\theta_W \\ Z_\mu &= -B_\mu \sin\theta_W + W^3_\mu \cos\theta_W \end{aligned} \tag{2.5}$$

Here A_μ is a massless combination which is the photon of electromagnetic interactions and Z_μ is a neutral, massive combination which is the Z^0 boson. The massive bosons acquire their mass via the Higgs Mechanism [47]. The mass of the bosons have been measured to be [48]

$$\begin{aligned} M_W &= 80.385 \pm 0.015 \text{ GeV}/c^2 \\ M_Z &= 91.188 \pm 0.002 \text{ GeV}/c^2 \end{aligned} \tag{2.6}$$

The mass of the bosons cause the weak force to be very short ranged. The range, R, is inversely proportional to the mass of the boson which mediates the interaction

$$R \sim \frac{1}{M_{W,Z}} \tag{2.7}$$

The presence of a propagator introduced by the GWS theory to mediate the weak interaction requires the matrix element to be altered so that the boson is included in the interaction. The propagator term is

$$\frac{-ig_{\mu\nu}}{q^2 - M^2_{W,Z} + i\varepsilon} \tag{2.8}$$

where $\bar{\psi}$ and ϕ are Dirac spinors. The unitarity limit says that summation of the probabilities for all possible states must be equal to one. Fermi's original four-point interaction does not abide by this limit, however, the introduction of a massive propagator in the GWS theory ensures that the model is consistent with the unitarity limit.

2.1.2 The Structure of Weak Interactions

Other than the obvious flaw in Fermi's model of the cross section increasing with energy indefinitely, it also has another problem. During the 1950s, C.S. Wu designed and carried out an experiment to test parity violation in weak interactions. The experiment placed an array of Co^{60} atoms in a magnetic field causing their spins to align. The atomic nuclei then underwent beta decay resulting in Ni^{60} and an emitted electron. The direction of

the electron produced in this decay was measured to deduce if parity was conserved or not. What the Wu experiment was able to show was that parity is not conserved in weak interactions. Fermi's model was unable to violate parity conservation [49] as the interaction he proposed consisted of two vector currents which transform the same way under a parity transformation. The lack of parity violation in Fermi's model forced physicists to begin searching for a structure of the weak interaction which would violate parity.

The task of looking for an interaction structure which met the criteria for weak interactions began with the most general form of the matrix element describing a weak interaction

$$M \propto \left[\overline{u}_{\psi,f}\hat{O}u_{\psi,i}\right] \frac{1}{M^2 - q^2} \left[\overline{u}_{\phi,f}\hat{O}u_{\phi,i}\right] \tag{2.9}$$

Here, $\hat{O}$ is used to denote some combination of gamma matrices which produce the structure needed for weak interactions to violate parity. A total of 5 bilinear covariant expressions can be formed from the gamma matrices (scalar, pseudo-scalar, vector, axial vector and tensor) which can be combined in sixteen different combinations. The weak interaction was shown to have a vector-axial vector (V-A) structure of the form

$$\bar{\psi}\gamma^{\mu}\frac{1}{2}\left(1-\gamma^{5}\right)\phi \tag{2.10}$$

where $\bar{\psi}$ and ϕ are Dirac spinors. The reason the V-A structure allows for weak interactions to violate parity is due to the fact that the vector and axial vector components behave differently under parity transformations. Vector currents are parity-even when a parity transformation is applied to them, whereas the axial-vector interactions are parity-odd. The interference of these two interactions therefore allows parity to be violated. Equation 2.10 contains $\frac{1}{2}\left(1-\gamma^{5}\right)$ which is the left hand projection operator, so parity is explicitly violated.

2.2 Neutrino Interaction Processes

There are different processes through which neutrinos can interact. As the center-of-mass energy of the interaction increases, new particles can be produced from the interaction vertex and as the energy increases further the neutrino can probe the nucleon and interact with its constituent quarks. Each of these interaction processes will now be discussed.

2.2.1 Neutrino-Lepton Interactions

Before any discussion on neutrino-nucleon interactions, it is useful to study how neutrinos interact with other leptons. Nucleons are composite particles that have an internal quark structure, which complicates matters when calculating the neutrino interaction cross sections. Leptons on the other hand do not have this added layer of difficulty and are therefore well suited as a starting point. The interaction that will be explored is that of neutral current scattering process in which the neutrino interacts with a lepton as shown in figure 2.1.

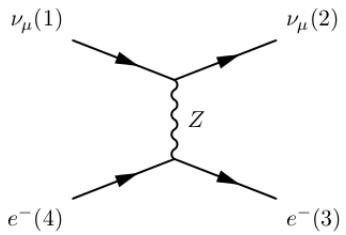

Figure 2.1: A muon-neutrino interacting with an electron via the neutral current elastic channel.

Denoting the Dirac spinors of each particle as u_i where $i = 1, 2, 3, 4$, and for $q^2 \ll M^2$, using the Feynman diagram to construct the matrix element for the interaction

$$M = \left[\bar{u}_2 \left(g_V^\nu - g_A^\nu \gamma^5\right) u_1\right] \frac{g_Z^2}{4M_Z^2} \left[\bar{u}_3 \left(g_V^e - g_A^e \gamma^5\right) u_4\right] \tag{2.11}$$

Using equation 2.11 the cross section is [50]

$$\frac{d\sigma}{dy} = \frac{m_e G_F^2 E_\nu}{2\pi} \left(\left(g_V + g_A\right)^2 + \left(g_V - g_A\right)^2 (1-y)^2 - \left(g_V^2 - g_A^2\right) \frac{m_e y}{E_\nu} \right) \tag{2.12}$$

The Bjorken variable, defined here to be $y = (q \cdot p) \,/\, (k \cdot p)$, has been used as the differential variable. Here q is the 4-momentum transferred to the nucleus in the interaction, p is the 4-momentum of the target and k is the 4-momentum of the incoming neutrino. As the energy of the interaction increases the last term in the equation 2.12 tends to zero.

Directly measuring such a cross section proves to be impractical since electrons within detectors will be bound in their orbitals to nuclei. At approximately 1 GeV, the

total cross section for the above interaction is of the order of 10^{-41} cm^2. This is an incredibly small cross section making the interaction unlikely even when compared to neutrino interactions on nucleons which have cross sections orders of magnitude larger.

2.2.2 Neutrino-Nucleon Interactions

In reality detectors are constructed out of materials comprising of more complex nuclei such as carbon and iron. Within the detector, rather than interacting with an electron bound in its atomic orbital, a neutrino is more likely to undergo an interaction with the atomic nucleus or its constituents. Neutrinos can interact via different processes which will now be discussed.

Figure 2.2 and 2.3 show the combined data sets for multiple experiments for neutrino and anti-neutrino modes respectively. Both plots compare data from various experiments to the theoretical prediction of the cross section from an interaction on a hydrogen nucleus modelled with $M_A = 1.0$ GeV (see section 2.2.2.1 for a discussion on the axial mass parameter, M_A). The anti-neutrino data is over a more limited energy range and can only provide a looser constraint on the axial mass parameter.

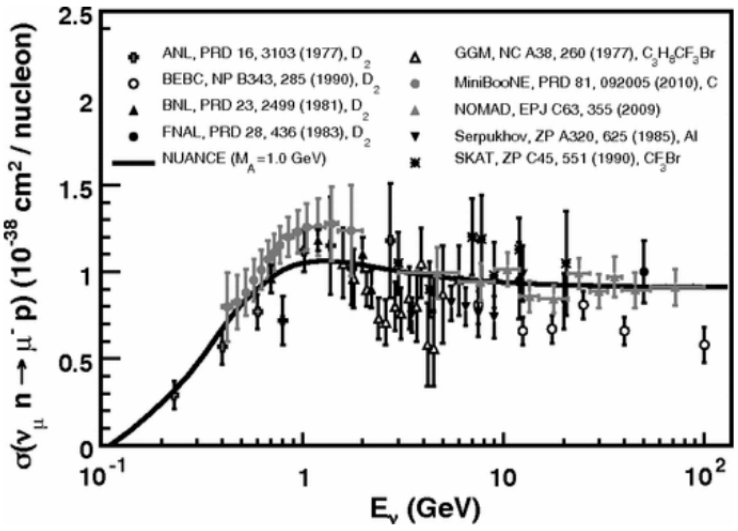

Figure 2.2: ν_μ CC cross section data plotted as a function of neutrino energy on different targets. Also plotted is the prediction for the same interaction on a free nucleon with the value of M_A assumed to be 1.0 GeV. Plot taken from [51].

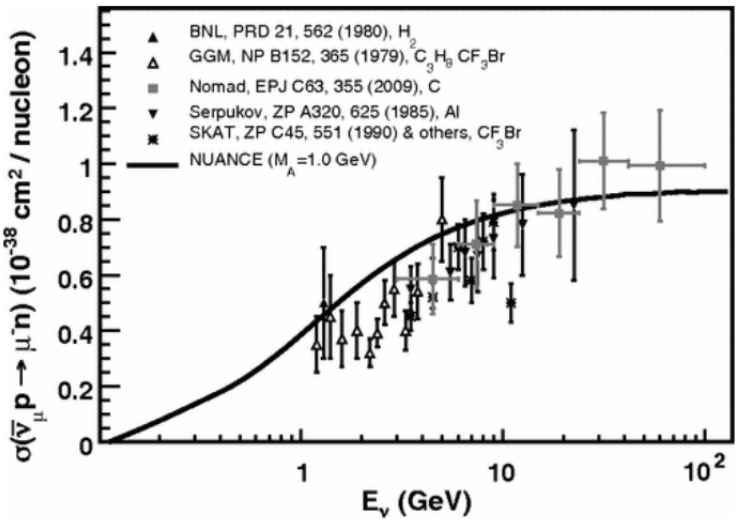

Figure 2.3: $\bar{\nu}_\mu$ CC cross section data plotted as a function of neutrino energy on different targets. Also plotted is the prediction for the same interaction on a free nucleon with the value of M_A assumed to be 1.0 GeV. Plot taken from [51].

2.2.2.1 Charged Current Quasi-Elastic Scattering

The charged current quasi-elastic (CCQE) interaction is the dominant process though which the neutrino interacts at neutrino energies below 1.5 GeV. This interaction produces a charged lepton, the flavour of which is dependent on the flavour of neutrino involved in the interaction. The isospin and the mass of the nucleon involved in the interaction also changes. The interaction is referred to as quasi-elastic because the lepton has changed from a neutrino in the initial state to a charged lepton in the final state. This interaction is depicted in figure 2.4.

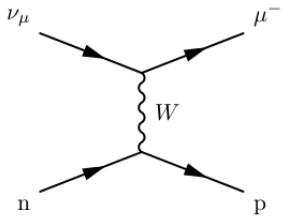

Figure 2.4: The charged current quasi-elastic (CCQE) interaction.

It is difficult to calculate the cross section of an interaction involving a nucleon analytically because the nucleon is an extended object. The cross section can be parameterised and measurements of these parameters are possible. Numerous studies have been carried out on the CCQE signal due to its importance in determining the flavour oscillation parameters precisely. In principle, CCQE interaction can be used to obtain the neutrino energy by examining the kinematics of the final state muon. However, identification of a muon and a proton from the interaction vertex within a detector is not definitive proof that a CCQE interaction has occurred due to nuclear effects which will be discussed in more detail in section 2.2.3. Even when a CCQE interaction is correctly identified, reconstructing the neutrino energy is not a trivial task as the Fermi motion (see section 2.2.3.1) and binding energy within the atomic nuclei in the interaction's initial state can introduce biases.

The formalism of Llewellyn-Smith can be used to write down the differential cross section as a function four momentum transferred squared denoted by Q^2 [52] as

$$\frac{d\sigma}{dQ^2} = \frac{G_F^2 M^2 \cos^2(\theta_c)}{8\pi E_\nu^2}\left[A\left(Q^2\right) \pm B\left(Q^2\right)\frac{(s-u)}{M^2} + C\left(Q^2\right)\frac{(s-u)^2}{M^4}\right] \tag{2.13}$$

The plus-minus symbol in the above equation is used to denote neutrino (plus) or anti-neutrino (minus) modes. The Fermi constant is denoted by G_F, M is the nucleon mass, θ_c is the Cabbibo angle and E_ν is the neutrino energy. Two of the terms in the cross section equation above contain $s-u$, where s and u are Mandlestam kinematic variables. The term $s-u$ is equal to $4ME_\nu - Q^2$. There are also three coefficients, $A\left(Q^2\right)$, $B\left(Q^2\right)$ and $C\left(Q^2\right)$, which contain the form factors and are expressed as

$$\begin{aligned}
A\left(Q^2\right) &= \frac{m_l^2+Q^2}{M_N^2}\Big[(1+\tau)(F_A)^2 - (1-\tau)(F_1)^2 + \tau(1-\tau)(\xi F_2)^2 \\
&\quad + 4\tau(\xi F_1 F_2) - \frac{m_l^2}{4M_N^2}\left((F_1+\xi F_2)^2 + (F_A+2F_P)^2 - 4(1+\tau)F_P^2\right) \\
B\left(Q^2\right) &= \frac{Q^2}{M_N^2} G_A (F_1+F_2) \\
C\left(Q^2\right) &= \frac{1}{4}\left[G_A^2 + (F_1)^2 + (F_2)^2\frac{Q^2}{4M_N^2}\right]
\end{aligned} \tag{2.14}$$

where the following notation has been adopted $\tau = Q^2/4M^2$, $\xi = (\mu_p/\mu_N - \mu_n/\mu_N) - 1$. The lepton mass is denoted by m_l and the proton and neutron magnetic moments by μ_p and μ_n respectively. The nuclear magneton is represented by μ_N.

The coefficients are constructed from the vector (F_i where i = 1, 2), axial vector (F_A) and pseudoscalar (F_P) form factors which contain all the information about the nucleon structure. The nucleon is initially assumed to be stationary with an internal charge distribution which is expressed by $\rho(r) = \rho_0 \exp(-Mr)$. The form factors are a Fourier transform of this distribution and described by a dipole of the form $F\left(Q^2\right) \propto \left(1 - Q^2/M_X^2\right)^{-2}$ where M_X is an empirical parameter [53].

Determination of the vector form factor can be made from electro-magnetic interactions as the vector component of the electroweak nucleon current contains the form factor. The dipole form for the vector form factor, for $Q^2 < 2.0$ GeV^2, is in good agreement with observations from electron scattering experiments [54], however as Q^2 increases the dipole form no longer describes the form factor.

The axial vector form factor is

$$F_A\left(Q^2\right) = \frac{F_A(0)}{\left(1 - Q^2/M_A^2\right)^2} \tag{2.15}$$

Here the form factor is parameterised by two parameters: $F_A(0)$ is a parameter which be found via measurements of beta decay and the nucleon axial mass, M_A.

The pseudoscalar form factor is expressed as a function of axial form factor as well as Q^2

$$F_P\left(Q^2\right) = \frac{2M^2}{Q^2 + m_\pi^2} F_A\left(Q^2\right) \tag{2.16}$$

A number of experiments which use different neutrino sources and target materials, over different energy ranges, have collected CCQE data to analyse. Using data obtained from bubble chamber experiments, M_A was found to be equal to 1.026 ± 0.021 GeV, a value in agreement with pion electroproduction data which found $M_A = 1.069 \pm 0.016$ GeV [55].

More recent experiments which have used targets such as carbon and oxygen have also made CCQE measurements with higher statistics. These experiments have extracted a value of M_A significantly larger than had been previously found. A notable result is the 2010 MiniBooNE value of M_A which was reported to be 1.35 ± 0.17 GeV [56]; a value which is approximately 30% larger than previous results. The analysis which yielded this result

did not take into account the 2p-2h (2 particle - 2 hole) contribution to the cross section when extracting the value for M_A. The 2p-2h contribution describes processes in which there are multiple nucleons involved in the interaction resulting in two particles in the final state. Models involving multiple nucleons in the final state, so called 2p-2h models, have been developed by Martini, et. al [57] and Nieves, et. al [58]. Interactions with one particle in the final state are referred to as 1-particle 1-hole (1p - 1h) and correspond to first order (tree level) diagrams and represent "true CCQE" interactions. Higher order diagrams represent 2p-2h interactions.

Another factor that needed to be accounted for was the way in which the cross section is altered by the Random Phase Approximation (RPA). The nuclear environment in which the neutrino is interacting can affect the boson which mediates the interaction before the interaction has occurred. RPA describes the correlations between the nucleons as well as polarisation of the medium, the result of which is that the cross section of an interaction is modified with a Q^2 dependency.

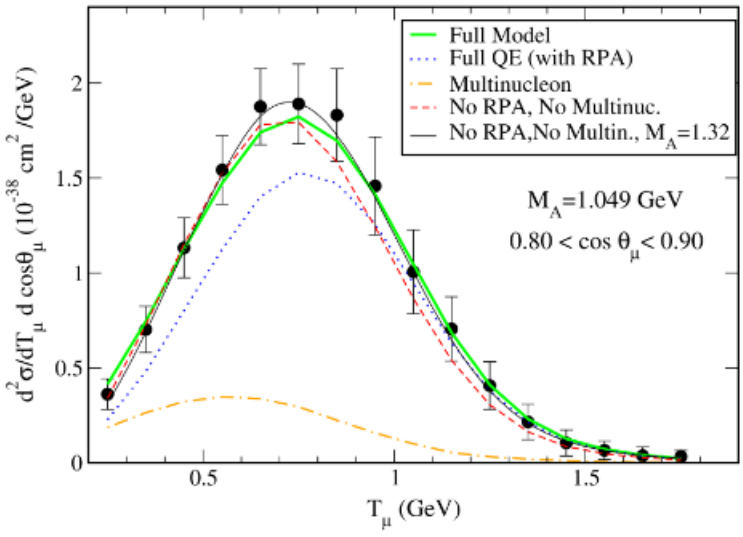

Figure 2.5: The MiniBooNE data with the CCQE double differential cross section in Muon angle and energy predictions from different models. Plot from [60].

Without taking into account the 2p-2h and RPA contributions to the cross section, the M_A parameter acted as a combination of the CCQE and 2p-2h interactions. Figure

2.5 shows the MiniBooNE data is in good agreement with a value of $M_A = 1.32$ GeV. The data is also shown to be described with $M_A = 1.049$ GeV, a value which is in better agreement with the value found from bubble chamber experiments, when 2p-2h effects are taken into account.

Other recent experiments which use complex nuclei as target have also published results with different values of M_A. The MINERνA experiment uses hydrocarbons as target, and in 2014 published a result consistent with $M_A \approx 1.0$ GeV. The Transverse Enhancement Model (TEM), a multi-nucleon correlation model, was included [59].

T2K has also published CCQE cross section results using ND280 and INGRID (see chapter 4 for a description of the T2K experiment and its detectors). In 2015, the CCQE cross section measured using the ND280 detector was published. A value of M_A was reported of $1.26^{+0.21}_{-0.18}$ GeV using the absolute muon momentum and angular distribution, though the analysis did not take into consideration the effects of 2p-2h on the cross section. A second value of $M_A = 1.43^{+0.28}_{-0.22}$ GeV was also reported when only shape information was used [61]. A second publication from the T2K collaboration reported the results using the INGRID detector. The events were separated by topology and the cross section for one or two track events were reported separately. A combined cross section was also presented. For one track events, and the combined cross section, agreement with a larger value of M_A was found. For the two track events, however, the value of M_A was found to be in agreement with the value extracted from bubble chamber experiments [62].

2.2.2.2 Resonant Interactions

As the energies involved in the neutrino interactions increase, new interaction processes become available and when the center-of-mass energy is sufficiently large it is possible that a nucleon excited state such as the Δ^+ or N^* are produced in the interaction. The Δ^+ baryon, for example, a short lived particle can be produced in an interaction before decaying into a pion and a nucleon which can then be observed. These resonances can be the product of both charged current and neutral current interactions and are the dominant interaction process in the energy range of about 1.5 GeV to 5.0 GeV. Figure 2.6 shows one such resonant interaction, in this example a neutrino interacts with a neutron via a W-boson producing a charged lepton and a positively charged delta baryon. This excited state decays rapidly into a pion carrying positive charge and a neutron.

Rein and Sehgal performed an analysis of the resonant single pion production cross

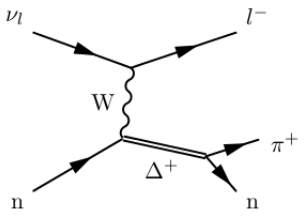

Figure 2.6: Resonant pion production from a charged current interaction.

sections, determining the cross section for resonances up to 2 GeV [63]. Increasing the energy of the interaction further can allow for a variety of resonances to be accessed leading to a variety of different particles in the final state including kaons, photons and multiple particles states all being possible.

Like elastic scattering, resonance production can be modelled using form factors allowing the nuclei to be treated as a point particle, these form factors do differ from those used in scattering interactions. It is assumed that resonant production have a dipole shape similar to the elastic form factors. The vector form factor is fitted to data obtained from electron scattering experiments and the axial form factor leaves two free parameters: C_5^A and M_A^{RES}. The resonance axial mass, M_A^{RES}, is usually studied and discussed separately from that of the CCQE axial mass. This is partly due to the axial mass parameter being treated as an effective parameter used to cover differences between what is experimentally observed and what theory predicts, differences which arise from effects which are not understood or are unknown.

2.2.2.3 Coherent Interactions

Coherent interactions describe the case where the neutrino interacts with the whole of the atomic nucleus rather than individual nucleons. After the interaction has occurred, the nucleus is in the same state as it was initially; it is in this sense that the interaction is coherent. Due to the higher mass of the target, coherent interactions tend to produce very forward going products which are usually pions. The interactions already discussed scale linearly with nuclear mass. The cross section for coherent interactions scale with the square of nuclear mass due to the neutrino-nucleus amplitudes summing coherently. This interaction mode has been well described theoretically for neutrino energies greater than 1-2 GeV, however, these models do not do as well at describing lower energy events. Though

little data is available in this region of phase space, the data sets which are available tend to show that the models over predict the cross section.

2.2.2.4 Deep Inelastic Scatterings

More energetic neutrinos can interact with individual quarks within the nucleon itself in a process known as deep inelastic scattering (DIS). This is the dominant process at neutrino energies greater than 10 GeV. Within the nucleon it is possible for quarks and anti-quarks to be created and annihilated if the time they exist is incredibly short. At lower values of Q^2, the neutrino sees a nucleon comprised of up and down quarks with some strange quark contribution (see section 3.3 for a discussion on nucleon strangeness). As the value of Q^2 increases, the neutrino can start to interact with the more massive quarks that exist temporarily within the nucleon due to the interactions between the valence quarks. Valence quarks are also able to take part in DIS neutrino interactions.

The interaction itself can be described by an elastic scattering process involving a neutrino and a quark but quarks are, due to the color confinement of Quantum Chromodynamics (QCD), bound together and never observed free. This means that the quark is not seen in the outgoing state, instead what is observed are hadronic jets which are produced as a result of nucleon fragmentation. A number of different products are possible in this interaction process and, as energies are increased, higher mass hadrons are able to be produced.

2.2.3 Nuclear Effects

Materials used in detectors are usually chosen based on a number of factors such as: cost, production, mechanical stability and the physics goals of the experiment. Using heavy nuclei as a target for neutrino interactions can provide a way to increase the size of the interaction data set, since interaction event rates increase with the mass of the target. However, complex atomic nuclei introduce effects which are poorly understood.

2.2.3.1 Fermi Motion

The nucleons inside nuclei are bound together and able to move about. The distributions of energy and momenta of the nucleons are poorly modelled in neutrino event generators. When a neutrino interacts with a nucleus it can, to first order, be thought of as it interacting with an individual nucleon with the notable exception of coherent interactions. This

assumption is called the impulse approximation. The mismodelling of the kinematics of nucleons within the nucleus cause uncertainties in neutrino interactions, especially those of lower energy. There are a number of models which have been developed and studied; to date it is unclear whether any of these models are correct.

The motion of nucleons in a nucleus is known as Fermi Motion (FM) and is assumed to be isotropic. Spectral Function (SF) models attempt to model the FM of the nucleons, an example of which is the global Relativistic Fermi Gas (RFG) model. This model assumes nucleons, which are fermions, do not interact with one another and move in some global nuclear potential. Each momentum state is filled up to the highest state, p_F, that is known as the Fermi Momentum. This feature of the global RFG model leads to a momentum cut off which is dependent on the number of nucleons in the nucleus, for example, $p_{F_{Carbon}} \approx$ 230 MeV/c. This implementation of the RFG model disagrees with data from electron scattering experiments [64].

This global RFG model can be improved upon by constructing a model in which the nucleons feel a potential based on their radial position within the nucleus; this is known as a Local Fermi Gas (LFG) model. In effect, this constructs a continuous series of RFG models, each with their own Fermi momentum which is dependent on the radial position, $p_F(r)$. LFG models do not show a momentum cut off as seen in RFG models, instead the momentum distribution takes a more Gaussian form. A comparison between the two models is shown in figure 2.7.

Nucleon-nucleon interactions, which are neglected in both RFG and LFG models, can cause the distributions of the initial nucleon momentum states to change as evident from electron scattering data [65]. There are models, also known as Spectral Function (SF) models, which include these interactions.

2.2.3.2 Final State Interactions

Further complications arise after the interaction has taken place. The hadronic products that are produced can undergo further interactions within the nuclear medium known as Final State Interactions (FSI). Scatterings within the nucleus could cause the particle to never be observed and can alter the particle's momentum. Interactions can also cause different products to be produced that exit the nucleus and result in the interaction to be misidentified. These effects are more common at low energies as the initial products from the neutrino interaction have a larger probability of interacting again before they exit

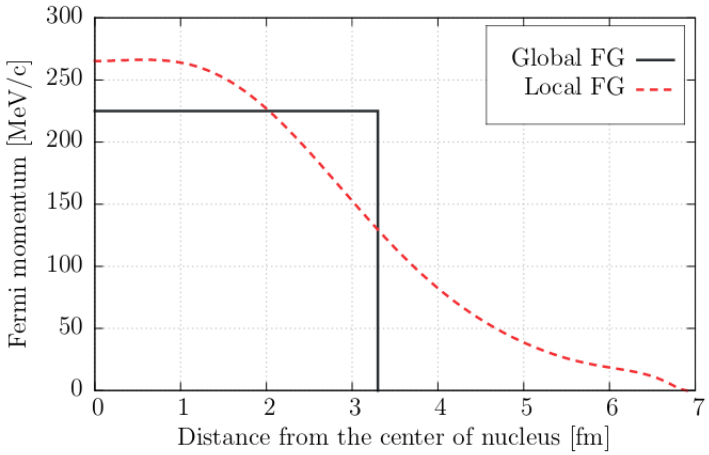

Figure 2.7: Fermi momentum as a function of radial distance within a carbon nucleus for both the global and local RFG models. Plot taken from [5].

the nucleus. In the range of energies where DIS is the dominant interaction process, the nucleus can break apart decreasing the chance for the products, which have high momenta, to interact again. Leptonic products are largely unaffected by FSI though they can undergo radiative effects which can alter the cross section [66].

It is difficult to constrain FSI with experimental data. It is also difficult to model FSI with neutrino generators which attempt to simulate the effect with a cascade model. The hadronic products which are simulated in an interaction are propagated through the nuclear medium in discrete steps, the size of which are dependent on the mean free path of the particle with each product treated independently. At each step the probability for each interaction process is calculated and an interaction is simulated if some criteria is met. This process is repeated until the hadron leaves the nucleus. External data sets are used to tune the mean free path of each hadron as well as the relative probability that an interaction process takes place. An alternative model has been implemented in the event generator called GiBUU, details of which will be discussed further in section 2.3.5

2.2.3.3 Pauli Blocking

Fermions which are in the final state of neutrino interactions, such as protons and neutrons, can be affected by Pauli blocking. Interactions can cause these fermions to have a change

in momentum, but being fermions they can only occupy a state that is vacant. This effect suppresses the cross section as it limits the phase space available to the final state particles. This effect is most notable for outgoing nucleons which have low momentum that are the product of low Q^2 interactions. This process, like FSI, is also poorly understood and can differ from model to model.

2.3 Generators

Event generators play a crucial role in neutrino physics analyses. Both oscillation measurements and cross section measurements rely on them. Different experiments in the past developed their own private generators, tailored to the energy range of their experiment as well as the target the detectors used. However, as the field has matured experiments have begun moving to more generic generators adopted by multiple experiments, allowing for better comparisons to be made between different data sets.

The generators produce Monte Carlo simulations of interactions, with different interaction processes being implemented on different target nuclei across different energy ranges. The process of simulating events is broken up into a number of distinct steps. The first step is to simulate a bare interaction. These interactions are usually simulated by use of pre-calculated total cross sections saved as a function of energy into splines or tables. This information allows the momentum as well as the direction of the outgoing particles to be determined. These particles are propagated then through a model of the nuclear medium generating final state interactions. The next step in the simulation chain is a detector simulation, allowing for a determination of events within the detector and is used by analysers to gain an understanding of the backgrounds important to their particular measurement.

Though event generators can allow for a useful insight into the dominant backgrounds that an analysis faces, their usefulness must be taken carefully. Different models can predict different background rates and different generators implement these models in a variety of ways. Using Monte Carlo simulations to develop an analysis can lead to a model dependence which can bias the results. Comparing cross section measurements to different generator predictions is common practice, however, little knowledge can be gained from these comparisons without understanding the differences between the generators. Even if the same model is implemented in two generators it does not mean that both generators will predict the same results. Different methods and data used can lead to different im-

plementations of a model. Interactions in the material surrounding the detector are not included in the simulations and must be generated separately before being combined with the simulation of events in the detector in the correct proportions.

It is useful to compare real data sets to those produced from a generator as a test of the model within the generator itself. When this type of comparison is made it must be kept in mind that models are only valid in certain energy ranges, outside this range of validity there is a transition to a different model which may not be well understood. Traversing this region between two models is usually accompanied by some ad hoc method so care must be taken when comparing data to model predictions in these areas of phase space.

Recently, there has been a vast amount of effort expended on modelling charged current interactions and implementing these in different generators. Neutral Current Meson Exchange Current (NC MEC) models, on the other hand, have been implemented in few generators, limiting generators that are available to neutral current analyses. This results in fewer comparisons between models and generators being made.

2.3.1 GENIE

As will be seen, the physics analysis which is the subject of this thesis makes use of the event generator known as GENIE [67]. GENIE is a modern example of a neutrino generator which is being adopted by more experiments and analyses. The core code of GENIE is written in C++, and was initially based on NEUGEN, a generator used by the Soudan 2 and MINOS experiments. With its modular structure, GENIE is very developer friendly, allowing for new modules to be included. The structure and implementation of GENIE was designed to allow it to be very generic and easily adopted by current and future experiments.

GENIE has similar models and interaction modes implemented as other generators but it will be useful to detail some of the properties of the generator. GENIE has many different interactions processes included in the event generation such as CCQE interactions as well as resonant and coherent pion production. Unlike other generators, GENIE 2.12 has an empirical NCE-MEC model implemented which can be used to estimate the background of a NCE analysis. The charged current implementation of this model produces consistent results with the same model implemented within NEUT.

Based on the value obtained from experiments using hydrogen and its heavier form,

deuterium, the axial mass, M_A, is set by default to 0.99 GeV in GENIE. This value is different from that found in the NEUT event generator which is defined to be 1.21 GeV, a value which was tuned to agree with the results found by the K2K experiment.

An official T2K production has been produced using GENIE 2.8.0 which was released in March 2013 in order to study events within ND280. The generator has the Relative Fermi Gas model as described by Bodek and Ritchie for all interactions. This model accounts for nucleon-nucleon correlations resulting in a high momentum tail. Final state interactions are handled by a sub-package known as INTRANUKE.

An updated version of the Rein and Sehgal model is implemented for both resonant and coherent pion production. For coherent interactions a term has been included to account for the lepton mass as well as the inclusion of more recent data sets than what was included in the original paper by Rein and Sehgal. Updated data sets have also been included for resonant interactions.

2.3.2 NEUT

NEUT [68] is the primary event generator used by the T2K collaboration and it has a long history. Adopted by the Super-Kamiokande experiment which verified neutrino oscillations, NEUT has its origins in the Kamiokande nucleon decay experiment and has been extensively developed over time, with many changes having been made to it. One such example is the addition of a re-weighting library allowing for analysers to carry out systematic uncertainty studies. The downside to using NEUT as a generator is that it is not publically available, restricting its usefulness to the neutrino community as a whole.

The Llewellyn-Smith model is used by NEUT to model CCQE interactions. Like GENIE, NEUT uses the Relative Fermi Gas model as its nuclear model however unlike GENIE the model as described by Smith and Moniz is implemented. Another similarity with GENIE is that pion production is modelled using the Rein-Seghal model. Final state interactions are handled internally by NEUT using the cascade model. NEUT includes the Nieves model for charged current interactions but does not include any 2p-2h model for neutral current interactions.

2.3.3 NuWro

Another event generator of note is NuWro [69; 70]. Developed in Poland by a group of theorists, NuWro, like GENIE, was written in the C++ and is used for testing and

developing new models.

The axial mass value is set to 1 GeV in NuWro, a value which is in agreement with the value of M_A determined by the early bubble chamber experiments. A number of nuclear models are included and can be turned on and off using a parameters file, the models include: Benhar spectral function, relative Fermi Gas, local Fermi Gas and random phase approximation.

Like other generators which have been discussed, NuWro has the Nieves model implemented for charged current interactions. One advantage NuWro has over other generators is the fact that it also has the Transverse Enhancement Model implemented for both charged current and neutral current channels. This allows for a comparison of the predictions of both these channels to be made.

2.3.4 NUANCE

A FORTAN based generator, NUANCE [71] was widely used but is no longer maintained and is not used by modern experiments. It was adopted by experiments such as K2K and MiniBooNE, though MiniBooNE maintained their own private version which they had made a number of changes to.

2.3.5 GiBUU

The Giessen Boltzmann-Uehling-Uhlenbeck Project, more commonly known as GiBUU [72], is an event generator intended for use in nuclear physics, however, it is used by neutrino experiments. As mentioned in section 2.2.3.2, the implementation of FSI in GiBUU is different from the cascade model usually found in neutrino generators. GiBUU analytically solves transport equations and propagates all the products through the nuclear medium together.

Chapter 3

Neutral Current Elastic Interactions

To date there is far less data available for NC interactions than for CC interactions. The NCE interaction, where a neutrino interacts with a nucleon via a Z^0 boson with no pion production in the final start, is an important channel to study as it provides a complimentary measurement to CCQE as well as providing information on the strange quark contribution to the proton spin (see section 3.3).

In addition to this, study of the NC channel has other benefits. As total neutrino flux is independent of flavour changes in the Standard Model, neutral current interactions can be used to constrain the neutrino flux in oscillation measurements. NCE interactions are an important background to understand for measurements which rely on neutron capture as the interaction can knock out a neutron with no other visible particle in the detector. One such measurement is the search for the diffuse supernova background at SK-Gd, the upgrade to Super-Kamiokande once the water has been doped with water-soluble gadolinium. Before exploring the NCE interaction a general discussion on weak neutral currents will be given.

3.1 Weak Neutral Currents

After the GWS theory predicted the existence of weak neutral currents, experimentalists set out to observe these interactions. Two of the first experiments to search for weak neutral currents made use of the Alternating Gradient Synchrotron facility at BNL and

the Proton Synchrotron at CERN, however neither experiment was able to prove their existence. The Heavy Liquid Bubble Chamber at CERN placed an experimental limit on the NC/CC ratio of 3% [73]. This limit deterred other searches for weak neutral currents for many years.

The Gargamelle experiment [74] was a large bubble chamber, located at CERN, in operation from 1970 until the discovery of an irreparable crack in 1979 forced it into an early retirement. The experiment used the Proton Synchrotron to create a neutrino beam to look for interactions in both neutrino and anti-neutrino modes. During the 9 years of data taking the experiment produced numerous results, the most notable of which was published in 1973 when it showed the first experimental evidence for neutral weak currents [74]. Out of approximately one million photographs taken of interactions within the detector, one was identified as a NCE electron scattering event. The criteria used to look for a signal event was a forward going electron with energy greater than 300 MeV. The Harvard-Penn-Wisconsin-Fermilab (HPWF) experiment at FNAL confirmed the findings of Gargamelle.

Further searches were carried out by the Gargamelle bubble chamber looking for evidence of neutrino-nucleon weak neutral current deep-inelastic scatterings (DIS).

$$\nu + N \rightarrow \nu + X \tag{3.1}$$

Here X denotes hadronic final state whereas N is the nucleon in its initial state [75]. About 160 such DIS events were observed. Observations of this channel were also made by the Columbia-Illinois-Rockerfelller (CIR) [76] and the Harvard-Pennsylvania-Wisconsin (HPWB) collaborations [77]. The HPWB collaboration was able to show that, like the charged current weak interactions, neutral current weak interactions also have the same V-A structure and therefore are also able to violate parity conservation.

3.2 Neutral Current Elastic Interaction on a Free Proton

The NCE interaction, as shown in figure 3.1, is kinematically identical to the CCQE interaction discussed in the previous chapter and is the simplest process through which a neutrino can interact with a nucleon. The neutrino-proton elastic scattering interaction has played a vital role in understanding weak neutral currents.

Consider a neutrino interacting with a proton via the exchange of a Z^0 boson. The

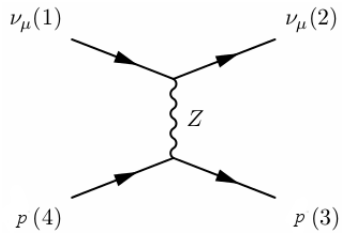

Figure 3.1: The neutral current elastic neutrino-proton interaction

4-momenta of the incoming and outgoing particles involved is described by

$$\begin{aligned} q_1 &= (E_\nu, \vec{p}_\nu) \\ q_2 &= (E_{\nu'}, \vec{p}_{\nu'}) \\ p_1 &= (M_N, 0) \\ p_2 &= (E_N, \vec{p}_N) \end{aligned} \tag{3.2}$$

where the subscript N is used to denote the nucleon which in this case is the proton. It is assumed that the nucleon is initially at rest and that the exchange of a Z^0 boson transfers momenta to the nucleon causing it to recoil. As the neutrino is unseen in the detector the only observable from the interaction vertex is the nucleon. The 4-momentum transfer squared, Q^2 is calculated from

$$Q^2 = 2M_N T_N \tag{3.3}$$

Here the mass of the outgoing nucleon and its kinetic energy are denoted by M_N and T_N respectively. This expression is independent of the nucleon scattering angle, with respect to the neutrino, allowing detectors unable to resolve the scattering angle to make such a measurement. If a detector were able to determine the scattering angle of the nucleon, θ_N, it would be possible to calculate the reconstructed energy

$$E_\nu = \frac{M_N}{\cos\theta_N \left(1 + 2M_N/T_N\right)^{\frac{1}{2}} - 1} \tag{3.4}$$

In order to calculate the NCE cross section, the matrix element for the interaction must first be expressed. Applying the Feynman rules which describe electroweak interac-

tions [78], the matrix element for $\nu + N \rightarrow \nu + N$ is

$$M = -\left(\frac{ig}{4\cos\theta_W}\right)^2 \bar{\nu}\left(q_2\right)\gamma^\mu\left(1-\gamma_5\right)\nu\left(q_1\right) i\frac{\left(g_{\mu\nu} - q_\mu q_\nu/M_Z^2\right)}{q^2 - M_Z^2}\langle N\left(p_2\right)|J_Z^\nu|N\left(p_1\right)\rangle \quad (3.5)$$

where θ_W is the Weinberg angle and J_Z^ν is the neutral weak current that was defined in section 2.1.1.

Considering the case where the momentum transferred in the interaction is low, $q^2 \ll M_Z^2$, the propagator term in equation 3.5 can be simplified as shown below

$$-i\frac{\left(g_{\mu\nu} - q_\mu q_\nu/M_Z^2\right)}{q^2 - M_Z^2} \rightarrow -i\frac{g_{\mu\nu}}{M_Z^2} \quad (3.6)$$

Defining the Fermi constant as

$$G_F = \frac{\sqrt{2}g^2}{8M_W^2} = \frac{\sqrt{2}g^2}{8M_Z^2\cos\theta_W} \quad (3.7)$$

The matrix element for the NCE interaction becomes

$$M = \frac{i}{2\sqrt{2}}G_F\bar{\nu}\left(q_2\right)\gamma_\mu\left(1-\gamma_5\right)\nu\left(q_1\right)\langle N\left(p_2\right)|J_Z^\mu|N\left(p_1\right)\rangle \quad (3.8)$$

The leptonic current in the matrix element, expressed by the terms denoting the neutrino, exhibits the vector-axial vector (V-A) structure of the weak interaction. This is a relatively simple expression when compared to the complexity of the hadronic current expressed within the bra-ket notation.

$$\langle N\left(p_2\right)|J_Z^\mu|N\left(p_1\right)\rangle = \langle N\left(p_2\right)|F_1\left(Q^2\right)\gamma_\mu + F_2\left(Q^2\right)\frac{i\sigma^{\mu\nu}q_\nu}{2M_N} + F_A\left(Q^2\right)\gamma^\mu\gamma_5|N\left(p_1\right)\rangle \quad (3.9)$$

The above nucleon weak current contains three nucleon form factors, $F_1\left(Q^2\right)$, $F_2\left(Q^2\right)$ and $F_A\left(Q^2\right)$. $F_1\left(Q^2\right)$ represents the Dirac form factor and $F_2\left(Q^2\right)$ the Pauli form factor and are the vector contribution to the nucleon weak current. The nuclear axial vector component of the hadronic neutral current is represented by $F_A\left(Q^2\right)$. These form factors were introduced and discussed in section 2.2.2.1.

Finally, the differential cross section for this interaction process, as a function of

Q^2, is

$$\frac{d\sigma}{dQ^2} = \frac{\overline{|M\left(Q^2\right)|^2}}{64\pi E_\nu^2 M_p^2} \tag{3.10}$$

where $\overline{|M|^2}$ denotes the spin-averaged matrix element squared which makes use of the matrix element that is defined above [53]. The NCE differential cross section can be expressed [79] in a similar form to the cross section for the CCQE interaction (equation 2.13)

$$\frac{d\sigma}{dQ^2} = \frac{G_F^2 Q^2}{2\pi E_\nu^2}\left(A\left(Q^2\right) \pm B\left(Q^2\right) W + C\left(Q^2\right) W^2\right) \tag{3.11}$$

Where $W = 4E_\nu/M_N = Q^2/M_N^2$ and $A\left(Q^2\right)$, $B\left(Q^2\right)$ and $C\left(Q^2\right)$ are functions that contain the form factors which were introduced in the discussion on the CCQE cross section. Expressing the cross section in this form will allow for a clearer discussion on how this cross section can be used to probe the strangeness of the nucleon.

3.3 The Proton Spin Crisis

Weak neutral current measurements opened up the possibility to study the structure of nucleons (protons and neutrons) via (anti-)neutrino-proton interactions. Nucleons are composite particles with an internal structure of quarks which are bound together via the strong nuclear force. A nucleon contains three valence quarks, which continually interact with one another through the exchange of gluons. Quark-anti-quark pairs can be produced which only exist for the briefest of moments, creating a "sea" of quarks/anti-quark pairs around the nucleon.

It was assumed that total spin of the proton was solely the due to the spin of the constituent quarks. However, during the 1980s an experiment named the European Muon Collaboration (EMC) [80] was able to experimentally measure the spin of the proton via muon-proton scattering. The conclusions drawn from this experiment was that valence quarks only contributed partly to the total spin of the proton [81]; this became known as the "proton spin crisis" and is still not resolved today.

3.3.1 The Strange Form Factors

The neutrino-proton NCE interaction is sensitive to the strange contribution to the quark structure of the nucleon. The form factors which describe the nucleon composition must be extended to include the contribution from strange quarks. It is assumed that the extensions to the form factors take the familiar dipole form as introduced in the discussion on the CCQE interaction (see section 2.2.2.1). The extension to the form factors take into account that the internal structure of the proton is more complex than just two up quarks and a down quark bound together but instead is possible for strange quarks to be created within the nucleon. The axial form factor becomes

$$F_A\left(Q^2\right) = \frac{1}{2}\frac{F_A\left(0\right)}{\left(1+Q^2/M_A^2\right)}\tau_3 + F_A^s\left(Q^2\right) \tag{3.12}$$

Here the term $F_A^s\left(Q^2\right)$ is the strange contribution to the axial form factor and τ_3 is +1 for protons and -1 for neutrons. The axial mass, M_A is the familiar dipole cutoff mass and $F_A\left(0\right)$ is determined by beta decay experiments. The additional $F_A^s\left(Q^2\right)$ factor which contains the information about the strange quark contribution to the nucleon structure

$$F_A^s\left(Q^2\right) = \frac{1}{2}\frac{\Delta s}{\left(1+Q^2/M_A^2\right)^2} \tag{3.13}$$

The nucleon spin which is carried by the strange quark is denoted by Δs. The vector form factors must also be modified to take strangeness into account

$$F_1^s\left(Q^2\right) = \frac{1}{6}\frac{-r_s^2 Q^2}{\left(1+Q^2/M_1^2\right)^2} \tag{3.14}$$

$$F_2^s\left(Q^2\right) = \frac{\mu_s}{\left(1+Q^2/M_2^2\right)^2} \tag{3.15}$$

Again, these form factors are assumed to have a dipole form. M_1 and M_2 are the masses of the strange vector form factors which are commonly assumed to be equal to the vector cutoff mass, M_V. The strange radius of the nucleon is r_s and μ_s is the strange magnetic moment of the nucleon. The values of the form factor parameters Δs, r_s and μ_s are given in table 3.1.

Parameter	Fit Value
Δs	-0.30 ± 0.42
r_s	-0.071 ± 0.096
μ_s	0.053 ± 0.029

Table 3.1: The strange form factor parameters extracted from a global fit to neutrino and electron scattering data provided by the BNL E734m HAPPEx, SAMPLE, G0 and PVA4 experiments [82].

3.3.2 Measuring Δs via the NCE Neutrino-Nucleon Interaction

The NCE neutrino-nucleon interactions, as well as electron scattering, allows for the structure of the nucleon to be probed. These experiments therefore allow a better understanding of the strangeness of the nucleon. The NCE neutrino-nucleon cross section is well understood and, unlike electron scattering, it is unaffected by other SM interactions. It also has no model dependencies or SU(3) flavour assumptions. It can also be defined entirely by the kinematics of the nucleon in its final sate.

The sensitivity of the NCE interaction to the strange contribution to the nucleon is evident at value of low Q^2 in equation 3.11. The term containing the function $C\left(Q^2\right)$ dominates making it sensitive to the axial form factor, $F_A\left(Q^2\right)$. The axial mass parameter can be extracted from a measurement of the NCE cross section and compared to the value gained from observations of CCQE interactions. Including the extension to the form factors to account for strangeness, Δs, it is possible to make a measurement of the contribution strange quarks have to the proton spin.

In order to determine the contribution of spin which the strange quark has on the total nucleon spin, it must be extracted from the strange axial form factor, F_A^s. The adopted method for making a measurement of Δs is to form cross section ratios. One such ratio is the neutrino-proton NCE cross section and the neutrino-neutron NCE cross section

$$\frac{\sigma\left(\nu p \rightarrow \nu p\right)}{\sigma\left(\nu n \rightarrow \nu n\right)} \tag{3.16}$$

If the $\Delta s = 0$, the cross section for NCE neutrino-proton interaction would be lower than the cross section for the same interaction involving the neutron. A negative value for Δs would mean that the cross section from the proton would be higher. It is not always possible to distinguish protons and neutrons, for detectors with this issue another ratio can be used. The ratio of the neutrino-proton NCE cross section to the cross section of

the CCQE interaction can be used. The CCQE interaction is not sensitive to Δs. This method allows for flux systematics, as well as some other systematics, to cancel.

3.4 Neutral Current Elastic Data

There is very little data available for the NC channel. During the 1980s the BNL E734 experiment carried out analyses on the neutrino-proton NCE cross section in both neutrino and anti-neutrino modes, using large enough datasets to evaluate M_A as well as the strange quark contribution to the nucleon spin. Figure 3.2 shows the result published by the BNL E734 experiment in 1987 for the NCE differential cross section on a carbon target in both neutrino and anti-neutrino modes. Both neutrino and anti-neutrino modes were fitted over a range of Q^2 between 0.4 GeV and 1.1 GeV. A combined fit to both data sets was carried out resulting in the axial mass value to be determined to be $M_A = 1.06 \pm 0.05$ GeV/c^2, in addition to this $\sin^2\theta_W = 0.218^{+0.039}_{-0.047}$ was also reported. The axial mass value obtained from this fit is in good agreement with values attained from experiments using hydrogen and deuterium as targets. At the time of its publication the world-average value for M_A was 1.032 ± 0.036 GeV/c^2 [80].

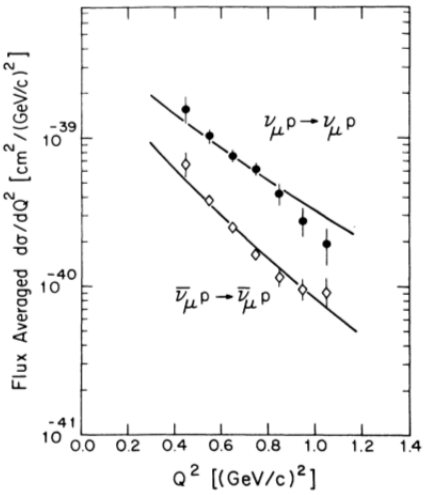

Figure 3.2: BNL E734 neutral current elastic differential cross section as a function of Q^2 in both neutrino and anti-neutrino modes. Plot taken from [80].

The value extracted for M_A by BNL E734 has its limitations. The neutrino flux

was calculated from the rate of CCQE events which could potentially bias the result. A prediction of the cross section was modelled using $M_A = 1.02$ GeV/c^2, a value which is in agreement with M_A that was extracted from the neutral current analysis.

A value for Δs was also extracted from the BNL E734 data by defining a variable $\eta = -\Delta s / F_A(0)$. It was found that $\eta = 0.12 \pm 0.07$, allowing Δs to be determined to be negative [80]. Electron scattering experiments have also made measurements of Δs via DIS interactions which the BNL E734 result is in agreement with [83]. The allowed region for M_A and η as found by BNL E734 is shown in figure 3.3.

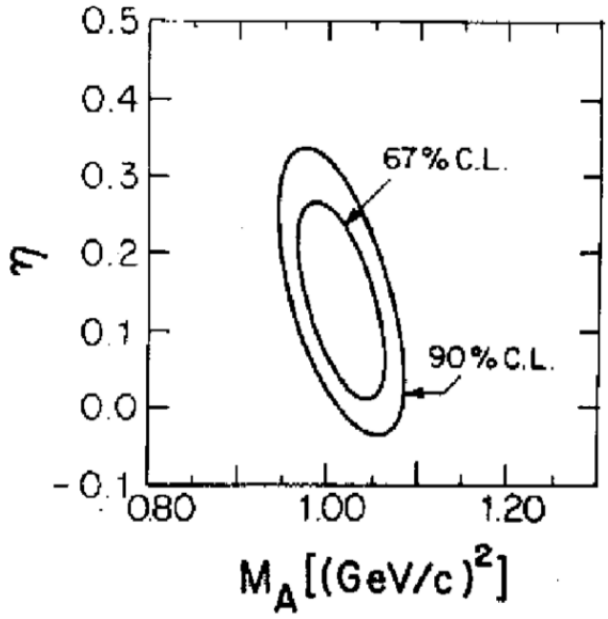

Figure 3.3: The allowed regions at a 67% and a 90% confidence level for the value of M_A and η found by the BNL E734 experiment from the χ^2 fit of the MC prediction to the neutrino and anti-neutrino cross section data. Plot taken from [80].

There has been no experiment with the specific goal of measuring the NCE channel since BNL E734. There have been experiments constructed which are sensitive to the interaction and able to collect NCE data with high statistics. MiniBooNE is one of the few recent experiments which have published results on the NCE cross section [84]; their result is shown in figure 3.4. The total 4-momentum transferred was determined by measuring the total kinetic energy of outgoing particles from the NCE vertex as described in 3.3, with

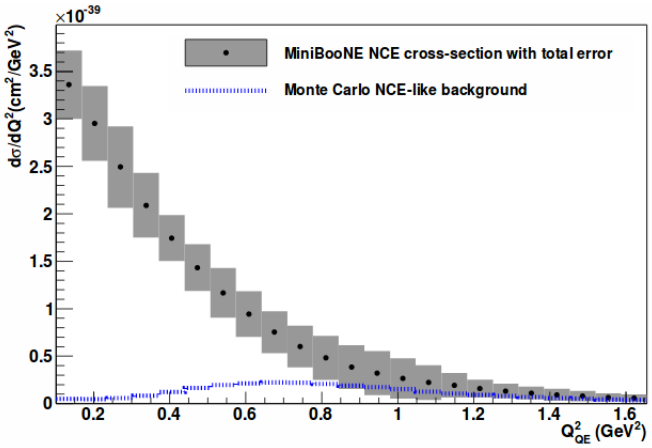

Figure 3.4: The MiniBooNE differential NCE cross section on CH_2 as a function of Q^2_{QE} with NCE-like background which has been subtracted. Plot taken from [84].

the assumption that the nucleon is at rest initially.

The MiniBooNE experiment published a differential cross section for the CCQE interaction that, when compared to the relativistic Fermi Gas model, was approximately 30% greater than expected [84]. The result of the NCE differential cross section analysis was then compared to this by plotting a ratio of the two as a function of Q^2, a method which, as mentioned, allows for a reduction in flux uncertainty. For this NCE/CCQE ratio to be made, Q^2 for the CCQE case is defined by the kinematics of the muon produced in the interaction under the assumption that the target is a stationary neutron. For NCE, Q^2 is still defined by the kinematics of the outgoing nucleon.

Figure 3.5 shows the result of the ratio compared to two Monte Carlo predictions generated using NUANCE, each with a different value of M_A. Each MC production also has a different value of κ which is used to denote a Pauli blocking scaling factor parameter. A value of κ was chosen to best match the data and encompasses nuclear effects which were not modelled or estimated. It can be seen from the plot that both MC predictions, one with $M_A = 1.23$ GeV and the other with $M_A = 1.35$ GeV, are in agreement with the data within experimental uncertainties. Under the assumption that $\Delta s = 0$, the NCE sample from the MiniBooNE experiment was able to determine $M_A = 1.39 \pm 0.11$ GeV with $\chi^2_{min}/\text{DOF} = 26.9/50$ [84].

In order to extract a value for Δs the MiniBooNE experiment used the ratio $\nu p \to \nu p$

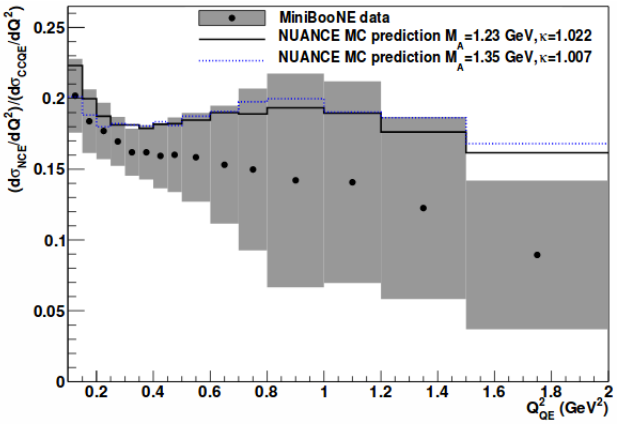

Figure 3.5: MiniBooNE NCE/CCQE cross section ratio on CH_2 as a function of Q^2. Plot taken from [84].

to $\nu N \rightarrow \nu N$ where p and N denote a proton and a nucleon respectively. The ratio $\nu p \rightarrow \nu p$ to $\nu n \rightarrow \nu n$ where n represents a neutron has greater sensitivity to Δs, however, the detector can only detect a neutron if it undergoes a strong interaction with a proton after the initial interaction has occurred. At low energies, below 350 MeV which is the Cherenkov threshold for protons in MiniBooNE, this interaction is hard to discern from a single proton event. Using the proton to nucleon ratio for the energy range of 350 MeV to 800 MeV, MiniBooNE found $\Delta s = 0.08 \pm 0.26$ in agreement with the value found in BNL E734 [84].

Chapter 4

The T2K Experiment

4.1 Tokai To Kamioka

Long baseline (LBL) neutrino oscillation experiments are designed to study how a neutrino beam, generated using accelerators, changes composition over the distance of usually a few hundred kilometers. In order to carry out oscillation analyses, LBL experiments make use of (at least) two detectors, one located near to the point of the beam production referred to as the near detector, and the other placed at furthest end of the experiment known as the far detector.

4.1.1 Overview of T2K

Tokai to Kamioka (T2K) [85] is a long baseline neutrino oscillation experiment located on Honshu, Japan's largest island, and is collaborated on by physicists globally. The Japan Proton Accelerator Research Complex (J-PARC) located in Tokai-mura, Ibaraki, hosts the near detector complex as well as producing the neutrino beam which is aimed at the far detector, Super-Kamiokande (SK), 295 km away. A diagram of the T2K baseline is shown in figure 4.1.

The T2K physics programme had a number of physics goals. The main goal was to measure the mixing angle θ_{13} via the observation of the appearance of ν_e in a ν_μ beam. As well as a precision measurement of θ_{13}, T2K hoped to provide a precision measurement of oscillation parameters in ν_μ disappearance [85]. However, the physics capabilities of the T2K experiment are not limited to neutrino oscillation measurements. The near detector, ND280 (Near Detector 280) enables a number of neutrino interactions to be studied via

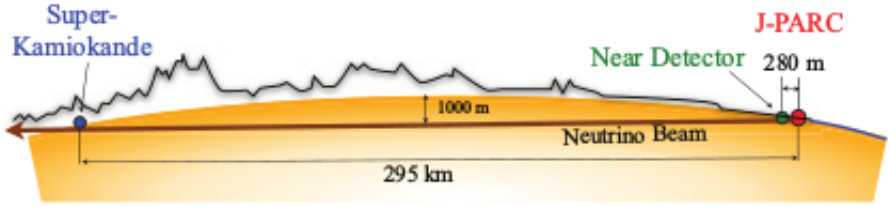

Figure 4.1: A diagram showing the T2K experiment from J-PARC to Super-Kamiokande. Diagram taken from [85]

cross section measurements.

T2K was the first long baseline neutrino oscillation experiment to position its near and far detectors off of the beam axis. As seen in chapter 2 neutrino oscillations have an energy dependency as well as being dependent on the distance which they travel. The production of T2K's neutrino beam provides the experiment with neutrinos with a wide spread of energies. However, placing the detectors 2.5° off-axis allows for a more mono-energic neutrino beam peaked at 0.6 GeV corresponding to an oscillation maxima at the far detector, shown in figure 4.2. Using this information the T2K L/E value is calculated to be approximately 491 km/GeV.

4.1.2 The Beamline

The neutrino beam used for T2K is generated in three stages. The beam production starts with a linear accelerator which initially accelerates H^- ions up to 400 MeV which are then converted to H^+ (protons) via charge-stripping foils when they are injected into the Rapid Cycling Synchrotron (RCS). The RCS is the next step in the production of the neutrino beam in which the protons loop around the synchrotron twenty-five times every second and are accelerated to an even higher energy of 3 GeV. Every cycle of the RCS contains two proton bunches. The beamline is shared between various experiments and around 95% of the bunches from the RCS are supplied to the muon and neutron beamlines in the Material and Life Science Facility (MLS). The remaining 5% of bunches are injected into the Main Ring (MR) which increases the energy of the protons by an order of magnitude. Multiple cycles of both the LINAC and RCS are used to fill the MR. The 30 GeV protons cycling the MR at 0.3 Hz can be extracted at two points - the slow extraction point and the fast

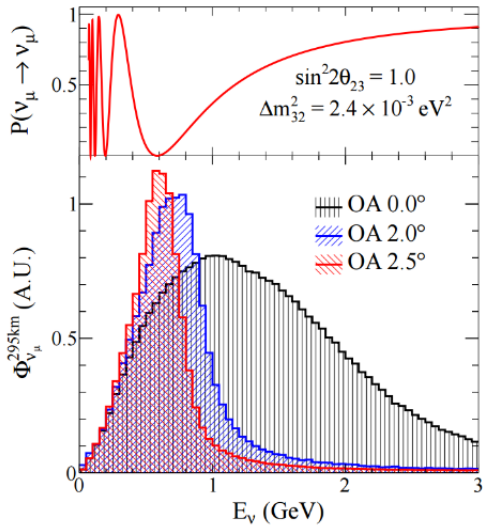

Figure 4.2: Predicted flux for different off-axis angles, and the muon neutrino survival probability at 295 km [85].

extraction point. The slow extraction point is where bunches are taken for experiments in the hadron hall and fast extraction is for the neutrino beamline [85]. The fast extraction point which supplies T2K with its beam is shown in figure 4.3. It is referred to as fast extraction due to all the proton bunches circling the main ring being extracted within a single turn by a set of five kicker magnets. To discriminate various backgrounds in the different detectors used by T2K, the time structure of the proton beam that is extracted is crucial. The MR fast extraction parameters are given below.

Circumference	1567 m
Beam Power	$\sim$ 750 kW
Beam Kinetic Energy	30 GeV
Spill Cycle	$\sim$ 0.5 Hz
Number of Bunches	8 per spill
RF Frequency	1.67 - 1.72 MHz
Spill Width	$\sim$ 5 μsec

Table 4.1: Parameters of the J-PARC main ring fast extraction.

The fast extraction consists of a primary and secondary beamline. The primary beamline

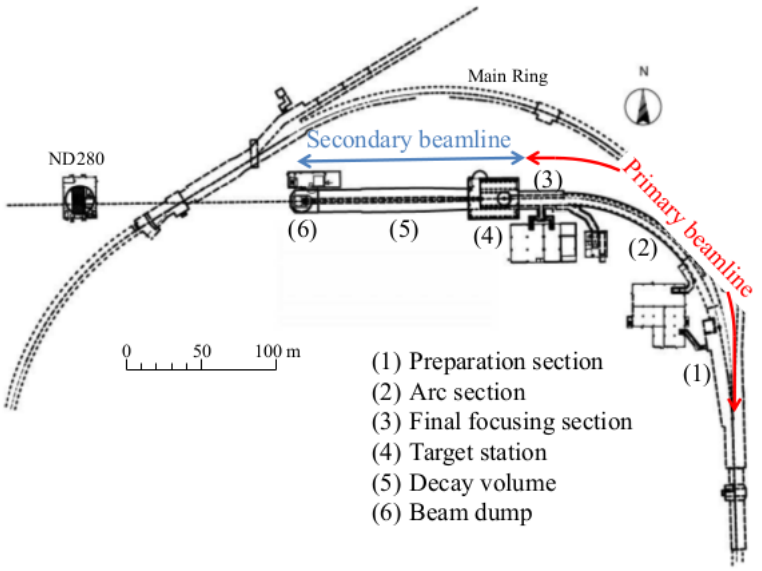

Figure 4.3: Overview of the T2K neutrino beamline showing fast extraction. Diagram taken from [85].

extracts a spill containing eight proton bunches from the MR using five superconducting kicker magnets to do so and directs the beam towards SK. It is here where a number of beam monitors are stationed to measure various aspect of the proton beam. Twenty-one Electrostatic Monitors (ESMs) are used to accurately measure the position of the beam as well as nineteen Segmented Secondary Emission Monitors (SSEMs) that make measurements of the beam profile. Also used are fifty Beam Loss Monitors (BLMs) and five current transformers that are used to measure the beam intensity allowing for a calculation of delivered POT (Protons On Target).

The target station, graphically depicted in figure 4.4, houses a 91.4 cm long and 2.6 cm diameter piece of graphite used as target for the proton beam as well as an Optical Transition Radiation (OTR) monitor which measures the beam direction and intensity. The size of the target results in approximately 85% of the protons interacting to produce pions and kaons. The mesons produced in the proton-carbon interactions within the graphite then enter the secondary beamline.

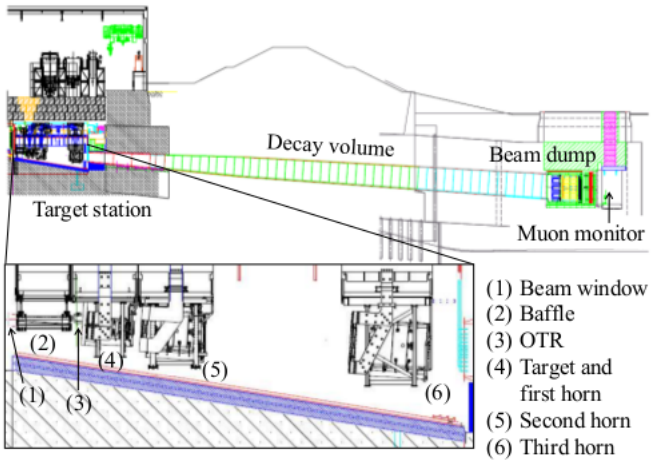

Figure 4.4: A side view of the T2K secondary beamline. Diagram taken from [85].

Three magnetic horns are used to focus the beam in the secondary beamline each with a current ±250 kA. The polarity of the current can be flipped allowing for either positive or negative charged particles to be selected and choose either neutrino or anti-neutrino mode to run in. The charged particles from the target then decay into muon neutrinos and muons via the decays $\pi \to \mu\nu$, $K \to \mu\nu$ and $K \to \pi\mu\nu$ (with some electron

and electron neutrino contamination) within a 96 m long decay pipe. At the end of the decay pipe waits a cooled 75 tonne graphite beam dump that is used to absorb unwanted components of the beam, however, muons of energy greater than approximately 5 GeV are able to pass through it. A Muon Monitor (MUMON) is located after the beam dump and detects muons on a bunch by bunch basis in order to measure the neutrino beam direction and intensity [86].

4.1.3 The Near Detectors

Located 280 m downstream of the target sits the near detector complex, housing both of the near detectors that are used by the T2K experiment. The purpose of these detectors are to measure the composition, the neutrino energy spectrum and interaction rates of the unoscillated beam near to its point origin. The first of these near detectors to be discussed is the off beam axis detector, ND280.

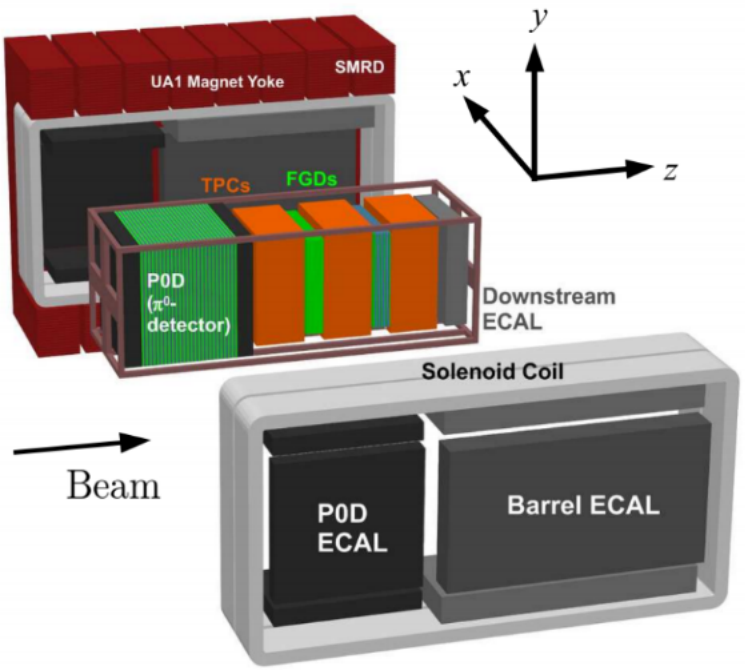

Figure 4.5: Exploded schematic of ND280 showing how the sub-detectors within it are arranged.

4.1.3.1 Near Detector 280

ND280 is made up of a number of sub-detectors, shown in figure 4.6, each designed for a specific purpose. The basket encases the inner detector which can be divided into two regions, the most upstream of which contains the π^0-Detector (P0D). The rest of the inner detector volume is dedicated to housing the tracker section of ND280 that consists of three Time Projection Chambers (TPCs) with two Fine-Grained Detectors (FGDs) separating them. The tracker region was designed to measure the charged particles that are the product of neutrino interactions. The inner detector is surrounded by a lead-scintillator sampling Electromagnetic Calorimeter (ECal) used to compliment the reconstruction capabilities of the inner detector via the detection of photons. All of these sub-detectors are surrounded by the repurposed UA1 magnet which provides a 0.2 T magnetic field allowing for sub-detectors to measure the charge and momentum of particles. The magnet return yokes are instrumented with plastic scintillators which form the Side Muon Range Detector (SMRD).

Different interaction processes have different event signatures in the detector. A CCQE interaction would be identified by a proton-like track and a muon-like track being produced from the same interaction vertex. The neutral current elastic interaction can either have a proton or a neutron exiting the nucleus depending on which nucleon was involved in the interaction. Due to neutrons being difficult to reconstruct within ND280, the NCE interaction, which is the topic of this thesis (see chapter 5), is studied by searching for a proton coming from the interaction vertex with no other particle present.

4.1.3.1.1 Fine-Grained Detectors

The tracker region of ND280 contains two Fine-Grained Detectors (FGDs) providing approximately 1.1 tonnes of target mass each and were designed to meet strict criteria. Each FGD is 36.5 cm thick ensuring that only the most penetrating particles that have been produced in a neutrino interaction such as muons to enter one of the Time Projection Chambers (TPC). However, particles with short ranges, such as recoil protons, generally do not make it into a TPC. To be able to resolve individual particle tracks and measure the particle's direction the FGDs must have granularity fine enough to do so. This granularity is achieved by scintillator bars made from single extruded polystyrene that have a square cross section of 9.6 mm arranged in either the x or y direction perpendicular to the beam axis.

The scintillator bars are organised into XY-modules containing 192 horizontal scintillator bars glued to a further 192 vertical scintillator bars in an alternating pattern. Wavelength shifting fibres guide the scintillated light to multi-pixel photon counters which digitises the light signals. Each scintillator bar is read out from one end while the other end is mirrored by deposition of aluminum which improves the light detection efficiency of each bar. There are 15 such modules make up FGD1, the most upstream FGD, whereas FGD2 only contains 7. The remaining space in FGD2 is taken up by 6 water modules made up of sheets of thin-walled, hollow corrugated polycarbonate with ends that are sealed with polyurethane sealant. Each water module is 2.5 cm thick and are kept at below atmospheric pressure via a pump system ensuring if a leak occurs the electronics remain dry. The photosensor response, saturation and non-linearity of the bars are calibrated via an LED-based light injection system which flashes the exposed ends. For further information on the FGD design and performance see [87].

4.1.3.1.2 Time Projection Chambers

The other sub-modules that make up ND280's tracker region are three Time Projection Chambers (TPCs) which are interspaced by the FGDs. The TPCs use the magnetic field generated by the UA1 magnet to measure the momenta and charge of the particles, and are able to provide particle identification (PID) via measurements of energy loss (dE/dx).

Identical by design, all of the TPCs contain a mixture of gas, a breakdown of which can be found in table 4.2. Predominantly made up of argon, the gas was chosen for its high drift velocity with little diffusion. The gas ionises as a charged particle passes through it and under the influence of an electric field (in the x-direction parallel to the magnetic field direction), the electrons drift towards Micromegas [89] readout pads away from central cathodes.

Compound	Fraction
^{40}Ar	95%
CF_4	3%
C_4H_{10}	2%
O_2	< 10 ppm
H_2	< 100 ppm
CO_2	< 100 ppm

Table 4.2: The gas composition of the Time Project Chambers (TPCs) used in ND280.

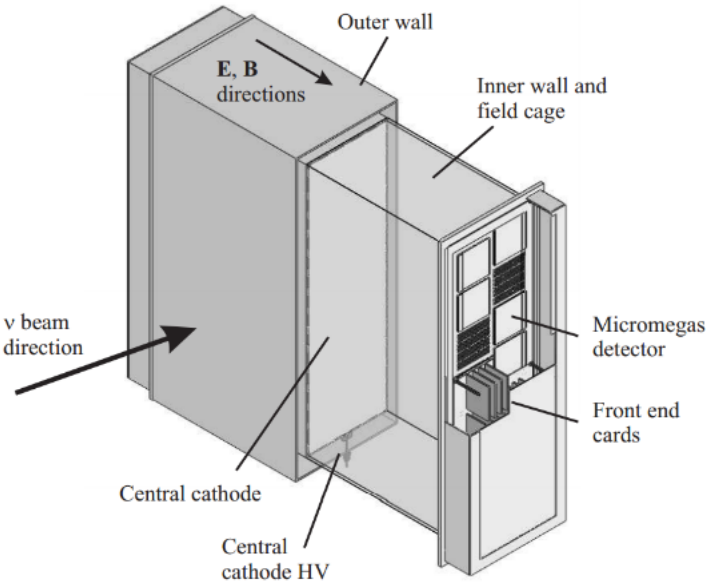

Figure 4.6: A schematic of a TPC used in ND280. Taken from [88].

The spatial resolution of the TPCs is dependent on the track angle and the drift distance but can achieve spatial resolution better than 1 mm allowing for momentum resolution of approximately $0.1p_{\perp.}$ / (GeV/c). For minimum ionising particles, the resolution has been determined to be $7.8 \pm 0.2\%$ allowing the TPC to discriminate between muons and electrons with the probability of a muon being misidentified as an electron being 0.2% for particles of energy less than 1 GeV/c. For further information on the design and performance of the TPCs see [90].

4.1.3.1.3 Pi-Zero Detector

The π^0 detector, known as the P0D, is the most upstream sub-detector in ND280. The primary goal for the P0D is to measure the cross sections of neutrino interactions which produce π^0s, the most important of which is the NCπ^0 cross section as it is a dominant source of background for the $\nu_\mu \rightarrow \nu_e$ signal at the far detector. The signal for the NCπ^0 interaction is two electromagnetic-like objects reconstructed in the P0D. The two objects are assumed to be photons produced for the π^0 decay.

Within the P0D are layers of triangular scintillator that are fitted together to form

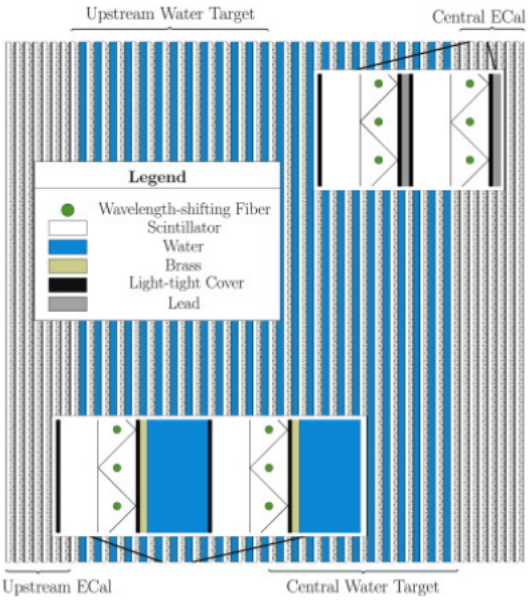

Figure 4.7: Schematic showing the composition of the π^0-detector reproduced from [91].

flat layers and are arranged in either the x or y direction. The scintillator layers are separated from one another by a pouch that can either be filled with water or be left empty. These two configurations are known as "water" and "air" configurations and by comparing data between the two allows for cross section measurements on water to be made. Neutral current pi-zero production measurements on water are performed using the P0D in order to constrain the uncertainty on the ν_e appearance studies at SK. Interleaved between water pouch and scintillator layer is a thin layer of brass as shown in figure 4.7.

The most upstream and downstream layers within the P0D do not contain water pouches. In these regions of the P0D thin layers of iron are sandwiched between the scintillators. These two sections of the P0D are called the upstream ECal and central ECal. As will be seen in section 4.1.3.1.4, the P0D is encapsulated by ECals [91].

4.1.3.1.4 Electromagnetic Calorimeter

The purpose of the ECal is to measure the energy of particles that are escaping the inner detector. The ECal in ND280 consists of thirteen modules split into three distinct sections. The P0D ECal that surrounds the π^0 detector; the barrel ECal which wraps around the

tracker section; and the downstream ECal located downstream of the tracker and occupies the last 50 cm of the basket.

The tracker-ECal consists of the barrel and downstream ECals and is so called because it surrounds the tracker section of the detector. The role of the tracker-ECal is to detect photons escaping the inner detector and measure their energy and direction allowing for better reconstruction of events. Identification of other charged particles is also possible with the tracker-ECal and can help discriminate electrons, muons and pions. Each module consists of alternating layers of scintillating polystyrene with a cross section of 40 mm x 10 mm and sheets of lead 1.75 mm thick that are bound to each other. Produced at the Fermi National Accelerator Laboratory (FNAL), the scintillator bars used in the ECal are made from extruded polystyrene doped with organic fluors at concentrations of 1% PPO (2,5-Diphenyloxazole) and 0.03% POPOP (1,4-bis(5-phenyloxazol-2-yl) benzene) with a layer of TiO_2 0.25 mm thick covering the surface providing light reflection and isolation. An overview of some of the properties of the ECals can be found in table 4.3. More detail on the bars can be found in the ECal technical paper [92].

	DS ECal	Barrel ECal
Length (mm)	2300	4140
Width (mm)	2300	1676 (top/bottom) 2500 (side)
Depth (mm)	500	462
Weight (kg)	6500	8000 (top/bottom) 10,000 (side)
Number of layers	34	31
Bar Orientation	x/y	Longitudinal and perpendicular
Number of Bars	1700	2280 Longitudinal (top/bottom) 1710 Longitudinal (sides) 6144 Perpendicular (top/bottom) 3072 Perpendicular (sides)
Number of MPPCs	3400	4560 Longitudinal (top/bottom) 3420 Longitudinal (sides) 6144 Perpendicular (top/bottom) 3072 Perpendicular (sides)

Table 4.3: A brief overview of ND280's ECals.

Thick layers of lead (4.00 mm) between plastic scintillators are used in the P0D-ECal allowing a greater efficiency of detecting photons from interactions within the P0D.

As mentioned, the P0D's primary goal is to detect π^0s produced in neutrino interactions, and to be able to do this effectively, detecting photons and being able to distinguish them from muons is key. This design of the P0D-ECal allows for 150 MeV photons to be tagged with efficiency greater than 95%. The increase in lead thickness leads to a reduction in the number of scintillator layers as the size of the ECal modules is constrained by the space between the basket, containing the inner detector, and the magnet.

Over time, due to various physical effects, which are discussed in section 4.2, the performance of the scintillator bars within the ECal degrade. This degradation alters the amount of scintillator light that is detected and is referred to as scintillator ageing, a phenomenon that will be discussed further in section 4.2.

4.1.3.1.5 Side Muon Range Detector

Plastic scintillators numbering 440 in total are attached to the magnet return yoke of ND280, referred to as the SMRD, these plastic scintillators are used for multiple purposes. They form part of ND280's cosmic trigger, helping identify cosmic ray muons that enter the detector, as well as allowing measurements of momenta for muons with a high angle relative to the beam direction referred to as escaping muons. The neutrinos in the beam can interact with material around the detector, the products of such interactions can enter ND280. The SMRD can identify these events.

The scintillator bars are positioned in air gaps between the iron return yokes resulting in different size bars being used. All of the scintillator bars measure 875 mm long and 7 mm in height. Vertical modules, which there are 248, have bars that are 175 mm wide whereas there are 192 horizontal modules consisting of bars 167 mm wide. Each pair of yokes is labelled with a number from 1 to 8, with 1 being the most upstream pair and 8 the most downstream pair, all of which have three layers of scintillators on the top and bottom. The sides of the yokes are also instrumented though the number of layers is dependent on each yoke. Like the top and bottom, yokes 1 through to 5 all have 3 layers, yoke 6 however contains 4 layers and the final two yokes both have 6 layers [93].

4.1.3.2 INGRID

Interactive Neutrino GRID (INGRID) is the second near detector used by T2K located in the same pit as ND280 but unlike ND280, it is placed on the beam axis. The purpose of INGRID is to measure the beam intensity and direction as well as providing daily nominal

beam intensity measurements with sufficient statistics. The detector has the capability of measuring the neutrino event rate with 1.7% uncertainty.

INGRID consists of 14 identical modules arranged in the shape of a plus symbol spanning 10 m in both the x and y directions. There are also 2 modules not a part of the plus pattern which are used to evaluate the axial symmetry of the beam. The observation of the number of neutrino events in each INGRID module also allows for the determination of the beam center to a precision better than 10 m at 280 m corresponding to a 0.4 mrad precision [85]. The composition of an INGRID module is alternating layers of iron, which is used as interaction mass, and scintillator. This sandwich of iron and scintillator is then surrounded by planes of scintillators used to veto activity from outside each modules.

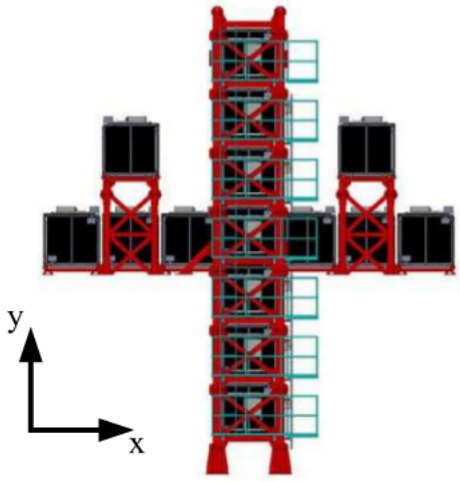

Figure 4.8: Schematic of INGRID showing module configuration. Taken from [85].

At the center of the plus arrangement of INGRID modules is the Proton Module which is similar in design to the other modules. However, the proton module does not contain any iron and has better tracking capabilities due to the use of smaller scintillator bars. The proton module is used to evaluate and improve current monte carlo modelling of charged current quasi-elastic events from identification of muons and protons from this interaction channel.

4.1.4 Super-Kamiokande

Located in the Mozumi mine under Ikenoyama (Mount Ikeno) in Kamioka, Gifu, Japan, is Super-Kamiokande (SK), T2K's far detector at a baseline of 295 km. Initially proposed in 1987 - data taking beginning in 1996 - it is a large water Cherenkov detector containing 50,000 tonnes of pure water that uses 13,000 photo-multiplier tubes (PMTs) to detect Cherenkov radiation. The original goal of SK was to search for proton decays, however, it also has the ability to observe neutrino interactions from various natural and man-made neutrino sources. Super-Kamiokande sits under 1 km of rock overburden that shields it from cosmic ray muons which have a rate of ~ 2 Hz within the mine, a reduction compared to the surface rate of 5 orders of magnitude [94].

During its operational lifetime it has been used as the far detector for the K2K experiment (1999 - 2004) and T2K (2009 - present). Since it began operating, four different run periods have been defined for SK based on the detector configuration:

- SK-1 (1996 - 2001)
- SK-2 (2002 - 2005)
- SK-3 (2006 - 2008)
- SK-4 (2008 - Present)

On the 12th of November 2001, one of the Photo-Multiplier Tubes (PMTs - described in further detail in 4.1.6.3) used in SK to detect light failed. It imploded suddenly resulting in a shockwave travelling through the water causing further PMTs to fail. Approximately half of the PMTs were lost to the accident; the remaining PMTs were re-arranged within the detector to cover as much of the inner surface as possible.

4.1.5 Cherenkov Radiation

As a charged particle, such as an electron or a muon, propagates through a dielectric medium with a speed greater than the local speed of light within the medium, electromagnetic radiation called Cherenkov radiation is produced. This optical phenomenon can be thought of in an analogous way to that of a sonic boom. The light that is produced is

emitted in a cone along the direction of the particle's trajectory; the angle between the particle's path and the leading edge of the cone is given by

$$\cos\theta_C = \frac{1}{n\beta} \tag{4.1}$$

Here θ_C is the angle in question, n is the refractive index of the medium and β is the ratio of the particle's speed to the speed of light. The photons cannot propagate beyond the leading edge of this cone resulting into an "optical shockwave". The ultra-pure water contained within the detector has a refractive index of 1.33 at 580 nm. Using this information the threshold for Cherenkov radiation within Super-Kamiokande is determined for different particles; for electrons the threshold is 0.76 MeV and muons is 158.7 MeV.

It is also possible to determine the number of photons produced per unit track length per unit wavelength using the following equation [95]

$$\frac{d^2N}{dxd\lambda} = \frac{2\pi\alpha}{\lambda^2}\left(1 - \frac{1}{n^2\beta^2}\right) \tag{4.2}$$

N represents the number of photons produced, x is the track length of the particle and λ is the wavelength. As in equation 4.1, n and β denote the refractive index and ratio of speeds respectively. The fine structure constant is represented by α and is equal to 1/137. For Super-Kamiokande, in the wavelength range of 300 nm to 550 nm, approximately 400 photons per centimeter of track length can be expected.

4.1.6 Detector Design

Super-Kamiokande is cylindrical in shape and is divided into two volumes referred to as the Inner Detector (ID) and the Outer Detector (OD). The detector is a self-supporting structure constructed from stainless steel and stands at 42 m height with a diameter of 39 m. A diagram of SK is shown in figure 4.9.

The T2K Global Positioning System (GPS) system provides synchronisation between the beam spill timestamps from J-PARC and the neutrino event trigger timestamps at Super-Kamiokande at the 50 ns scale. Making it possible to determine whether neutrino has originated at J-PARC or is from another source.

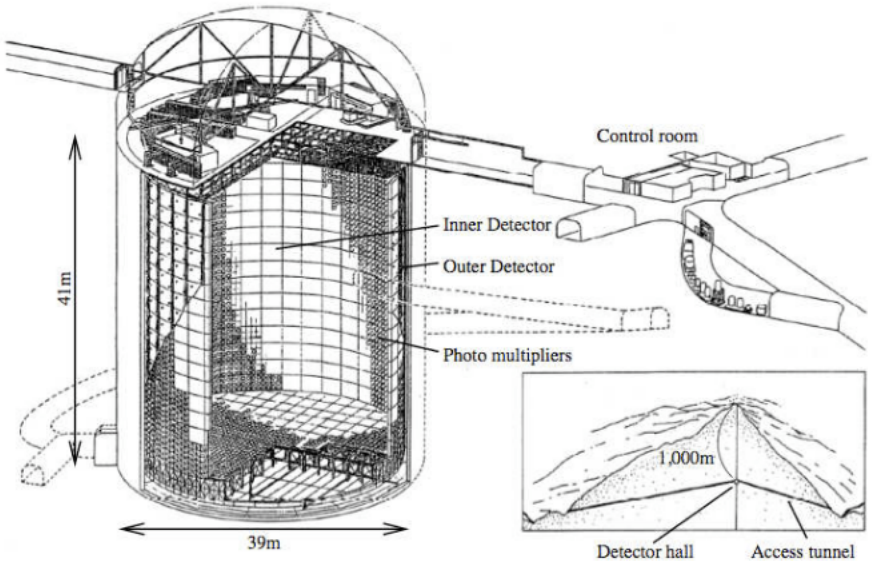

Figure 4.9: Schematic of Super-Kamiokande, taken from [85].

4.1.6.1 The Inner Detector

The ID is a cylinder measuring 36.2 m high with a diameter of 33.8 m able to hold 32 k tonnes of water, 25 k tonnes of which are defined to be the fiducial volume (FV). It is optically isolated by black sheets of polyetlyene terephthalate (PET) that line the wall of the ID between the PMTs to prevent any light leaks. During SK-1, 11,146 PMTs of 50 cm diameter were used giving a total coverage of approximately 40%, though the accident in 2001 resulted in over half of these being lost. For the second run period, the remaining PMTs (5,182 in total) were rearranged to give 19% photocathode coverage. In 2006, repair work was carried out, with new PMTs installed there are now 11,129 PMTs in SK's inner detector giving a total of 40% coverage once again. A stainless steel frame separates the inner and outer detector volumes and it is on this frame that the PMTs are instrumented. [85].

4.1.6.2 The Outer Detector

The OD is the 2 m of water that surrounds the ID. Reflective white sheets of plastic commercially called Tyvek are attached to the stainless steel frame facing outwards in

order to reflect light back into the OD. At 400 nm, Tyvek's reflectivity is approximately 90%. Like the ID, the OD is instrumented with PMTs totaling 1,885 in number, though these PMTs have a smaller diameter than those used in the ID. Measuring 20 cm in diameter and facing outwards, the PMTs are used to veto events from outside the detector such as cosmics or radioactivity from the surround rocks. The photocathode of each PMT in the OD has a wavelength shifting cover that increases the light collection efficiency by 60%. The covers reduce the timing resolution from 13 ns to 15 ns, however, the importance of light collection efficiency is far more import than timing resolution for vetoing external events [85].

4.1.6.3 Photo-Multiplier Tubes

As mentioned, SK is a water Cherenkov detector that uses PMTs to detect the photons emitted for interactions within the water. The PMTs used were developed by Hamamatsu Photonics K.K who closely worked with Kamiokande collaborators to design a PMT that met their specifications - the result was the Hamamatsu R3600 PMT [94]. The PMTs are sensitive to light with wavelength in the range of 300 nm to 600 nm, the region of the electromagnetic spectrum in which the Cherenkov radiation from interactions in SK can be found. The quantum efficiency of each is approximately 20%.

Photoelectrons are produced when a photon interacts with the cathode within the PMT. This photoelectron signal is amplified by a gain of 10^7 via a chain of 11 dynodes. The PMTs are sensitive to the geomagnetic field produced by the Earth. To minimise this effect, 26 Helmholtz coils are fitted to the walls of the tank, reducing the field from 450 mG to 50 mG.

4.1.7 Background Reduction

The detector is subject to a number of backgrounds which steps have been taken to reduce as much as possible. As mentioned, the detector is located beneath 1,000 m of rock in order to reduce the number of cosmic rays able to make it into the detector. Further steps are also taken to reduce other backgrounds.

4.1.7.1 Water Purification

The Cherenkov radiation produced within the detector must travel some distance before it is detected by a PMT; the water must therefore be as transparent as possible to keep

the photon yield at a detectable level. The water used is obtained from the mine itself and passed through a number of processes to purify it. The first step in the process is to pass the water through a 1 μm filter to remove any large particles before the water is sent to a heat exchanger that is used to cool the water to 13°C. This step is to limit the growth of any bacteria found in the water. The next stage in ensuring the water remains pure is removing heavy ions via use of a cartridge polisher. Here the water is also exposed to a ultra-violet steriliser to ensure any remaining bacteria is killed before being subjected to reverse osmosis. Radon and other gases which can be dissolved in the water are removed by use of a vacuum degassifier system. The final stage of water purification before being returned to the tank is to pass the water through ultra-filters that are able to remove any remaining particles larger than about 10 nm. To maintain the high level of water purity, about 60 tons of water every hour must be circulated through this system [94].

4.1.7.2 Air Purification

The rock that the mine is dug into is leaking radon into the air within the mine; unfortunately, radon can be dissolved in water. There is an air gap between the surface of the water and the top of the tank that can allow the radon rich air to come into contact with the water within the tank. The radon present in the water accounts for some of the low energy background observed. The walls of the experimental hall are coated with a polyurethane material to minimise the amount of radon able to leak into the air and to further minimise the contamination, (radon-free) air from outside the mine is continuously circulated around [94].

4.1.8 Super-Kamiokande Events

For neutrino oscillation analyses on T2K, it is important to be able to distinguish between electron and muon neutrinos within SK. Fortunately, it is easy to determine the flavour of a neutrino from the event display. When an electron neutrino interacts in the water and an electron is produced, as the electron propagates through the medium, Cherenkov radiation is emitted. However, the electron can undergo further scatterings causing the ring of light that is observed to be fuzzy as can be seen in figure 4.10a. Muons are largely unaffected by scattering interactions as they propagate within SK and the rings of Cherenkov radiation that are observed are sharper, shown in figure 4.10b.

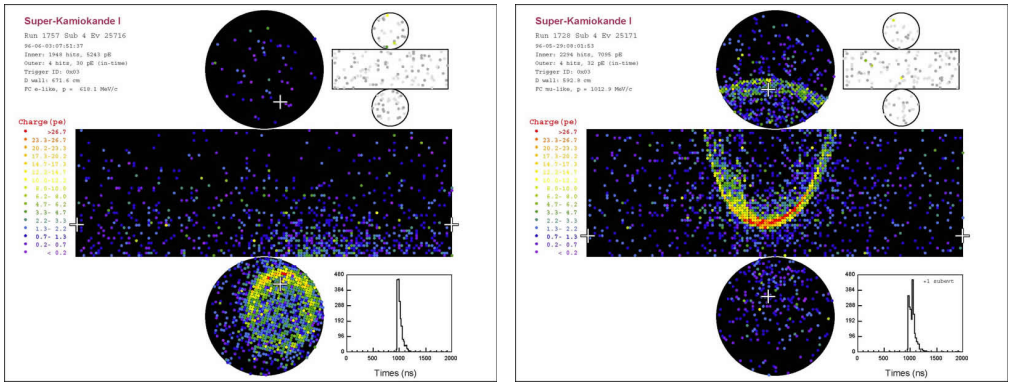

(a) Electron neutrino event in SK.

(b) Muon neutrino event in SK.

Figure 4.10: Event displays showing (a) an electron neutrino and (b) a muon neutrino event in SK. Event displays taken from the Super-Kamiokande public website [96].

4.2 The Ageing of ND280's Electromagnetic Calorimeter

It is known that over time plastic scintillators degrade and as a result produce less light. This effect has been seen in previous experiments, such as MINOS [97], that use similar plastic scintillator bars. This section details an analysis that studied this effect on the ECals in the near detector, ND280. The results of this study are then used to calibrate the charge of the recorded hits in the ECal so that, from an analysis point of view, the ECal will not have aged.

4.2.1 The Physics of Scintillators

As a particle passes through a scintillating material, it is possible for the electrons in the medium to be excited into a more energetic, yet unstable state. The process through which the electron returns to a state of equilibrium is via the emission of a photon - this process is known as scintillation. The difference between the energy of the excited state and the ground state is equal to the energy of the photon emitted. The detection of a particle via radiation produced in this manner is one of the oldest methods of particle detection and is still widely used to this day.

Scintillation can occur in crystals, noble gases and liquids, as well as in plastics from which the ECals are constructed. The following discussion will focus on plastic scintillators of the type used in the ECal. A plastic base structure is used that has fluors (chemical

compounds that possess the ability to re-emit light) added to it in varying amounts - usually two different fluors are used and are referred to as the primary and secondary fluor. The particle initially interacts with the primary fluor that is passing through the scintillator, causing it to be excited into an unstable state. De-excitation of this primary fluor produces a photon that is of sufficient energy to be in the ultra-violet (UV) region of the electromagnetic spectrum. It is this UV light that promotes the secondary fluor into an excited state that is then followed by the emission of a photon in the visible part of the spectrum that is then detected [98].

As mentioned in section 4.1.3.1.4, the scintillator bars used in the ECal consists of extruded polystyrene doped with organic fluors at concentrations of 1% PPO (2,5-Diphenyloxazole) and 0.03% POPOP (1,4-bis(5-phenyloxazol-2-yl) benzene). The PPO acts as the primary fluor and scintillates light at 385 nm at the peak of its spectrum which lies in the UV range of the electromagnetic spectrum. The UV light emitted then excites the PPO causing it to emit violet light of 410 nm at the peak of its spectrum when the fluor undergoes the radiative process that returns it to its ground state.

The degradation of the plastic scintillator bars used in ND280's ECals is the result of a number of effects:

- Thermo-oxidative processes occurring within the bar itself; these chemical reactions produce peroxides that absorb photons with energy which is in the region of the scintillating light. Over time the amount of peroxides builds up, which has the overall effect of the number of photons being detected by the sensor decreasing over time.

- Internal and surface defects can be caused by chemical and mechanical stress. Cracks in the scintillator bar can inhibit the propagation of the photons through the material to the sensor

- Diffusion of low molecular components of the scintillator bar can cause a yellowing of the interior and surface.

More information of the processes that cause plastic scintillators to degrade can be found in [99]. The ageing of the ECals is due to a combination of these effects.

4.2.2 Analysing the Degradation of the ECal Scintillator Response

Two independent studies were performed to study the degradation of the plastic scintillator bars used in ND280's ECal modules. The first study involved studying the light yield from cosmic ray muons that cross multiple ECal bars. A control sample of cosmic muons is defined to study the rate of degradation of the ECals. The sample must contain particles that enter the ECal and cross several scintillator bars. A diagram depicting a particle passing through several scintillator bars is shown in figure 4.11. A second study was also performed independently of the study detailed below. Like the first study, a control sample of cosmic muons was used to determine how much the light yield has decreased. Unlike the first study which divides the ECal up into bar directions, the second study studies looks at the ageing in each ECal module. Further details of the second study can be found in appendix A. The two analyses were developed in parallel and provided a means to cross check the results.

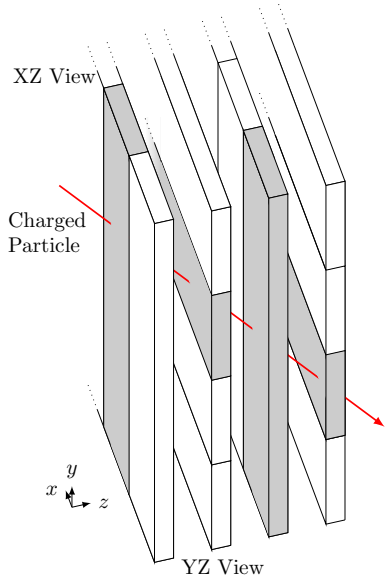

Figure 4.11: A schematic showing a charged particle traversing several scintillator bars within an ECal module.

4.2.2.1 Analysis Methodology

In order to study how the average response of the electromagnetic calorimeter has degraded over time, a control sample that is well understood must be defined. A sample of cosmic muons was used, as they will deposit approximately equal amounts of energy into each scintillator bar as they propagate through the detector. Due to the size of the data set, the study is not statistically limited.

Corrections applied to it to ensure each track is comparable to the other tracks in the sample. The longer the track is within a scintillator bar the greater amount of charge is deposited within it. The further the hit is in the bar from the sensor, the more light that is lost along the bar. To take this into account, corrections based on the angle of the track and the distance from the sensor is applied to each recorded hit.

As well as corrections applied to the data sample, each event must pass a series of cuts to be included in the study. One requirement is that the track must not be a clipping muon, that is, a muon which only passes through the edge of the ECal. The track must be sufficiently long enough for it to traverse several bars and deposit enough charge in them. The position where the extrapolated reconstructed muon track passes through the bar must be at least a 150 mm from the end of the bar to remove any edge effects from the study. Finally, the track in the ECal must be a charged particle.

To study the ageing of the ECal, the charge distribution of all the recorded hits are binned into specific time periods. For each bin, the recorded charge distribution is fitted with a Landau-Gaussian function [100]. The form of the fit to the data, $f(x)$, is

$$f(x) = N \int L(x, p_0, p_1) \times G(x, \sigma)\, dx \tag{4.3}$$

where N is a normalisation factor, $L(x, p_0, p_1)$ is the Landau function with p_0 is the Most Probable Value (MPV) and p_1 is the Landau width. The Gaussian distribution that is convoluted with the Landau is denoted by $G(x, \sigma)$. The σ variable denotes the width of the Gaussian distribution. This fit is appropriate to use to model the charge distribution as the Landau is able to describe the energy loss of the particle as is propagates through the material in the ECal while the Gaussian characterises the electronic noise [101]. The MPV is the variable of most interest when characterising the degradation of the scintillator bars. Figure 4.12 shows an example of one such charge distribution for all the bars in the DS ECal. The limits of the Landau-Gaussian fit are calculated using an iterative method that reduces the range over which the function fitted in each iteration until the value of

$\chi^2/\text{NOF} < 25.0$, where NOF stands for number of degrees of freedom. For each time period defined, this fitting procedure is repeated allowing for each fitted parameter to be studied as a function of time.

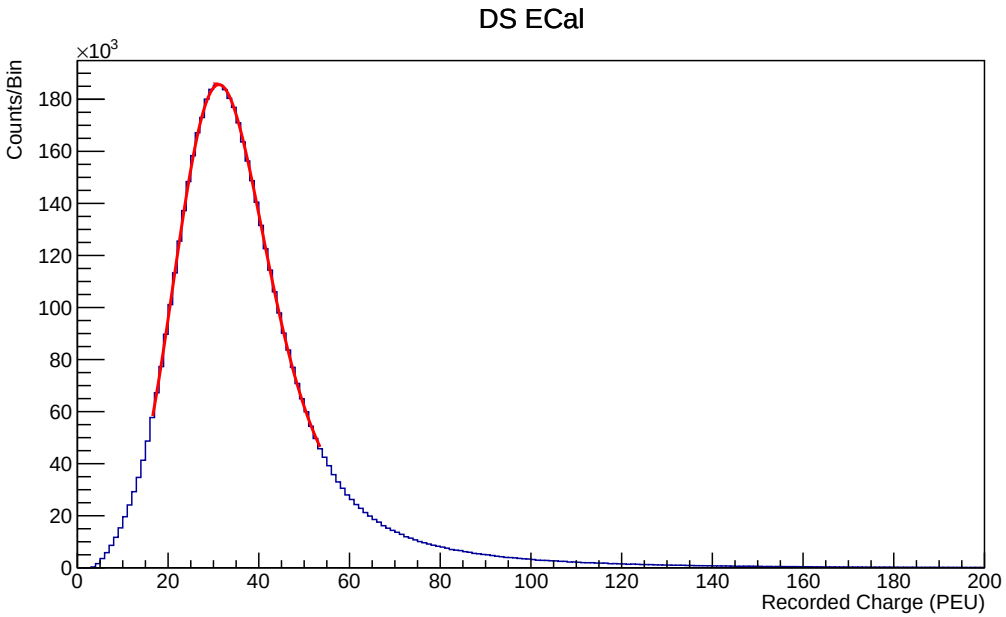

Figure 4.12: The Landau-Gaussian distribution of recorded charge deposited within a scintillator bar. The red line is the best fit to the data (blue line) with the Landau-Gaussian model.

4.2.2.2 Results

Plotting the MPV in bins of approximately one month allows for the degradation of the ECal to be quantified. Figure 4.13 shows how the MPV changes over time. As expected the response gradually decreases over time, an effect that can easily be seen by eye.
Fitting the plots with an exponential function allows for this decay to be quantified. The exponential function takes the form shown in equation 4.4 where $\bar{Q}$ is the MPV charge recorded, A is the y-offset which is the minimum charge that the ECal will tend to and B is a scaling factor. The decay constant is $1/\kappa$ and t is the time since 2010 (the year which

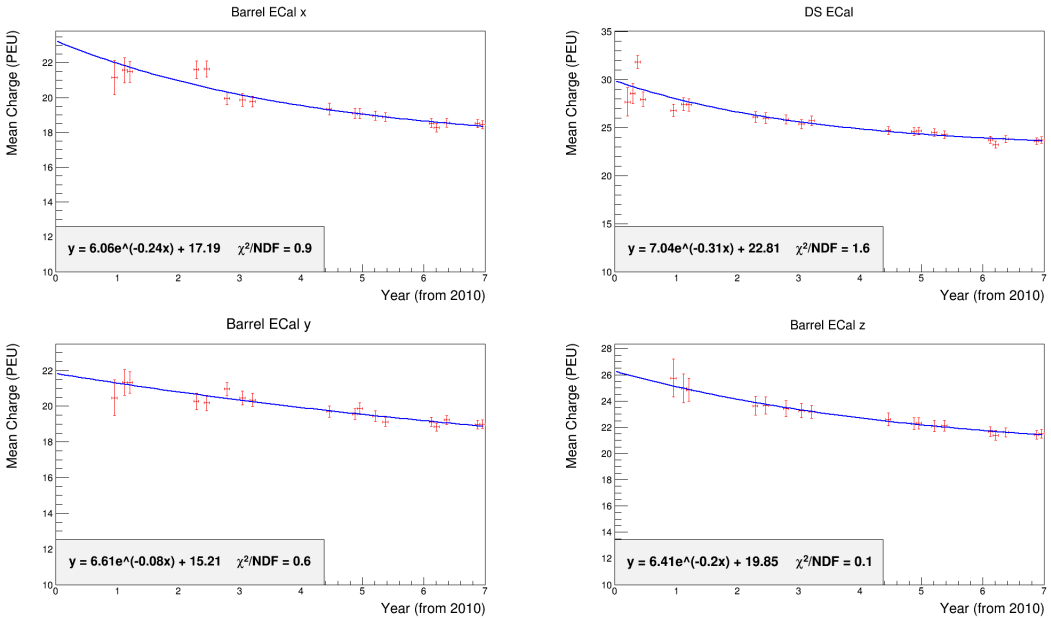

Figure 4.13: The MPV from the Landau-Gaussian distribution fitted to the charge distributions as a function of time. Here the the x, y and z labels in the titles for the Barrel ECal plots refer to the orientation of the bar in the global ND280 co-ordinate system. The uncertainty on each data point is calculated using equation 4.5. The blue line fitted to the data points is an exponential function given in equation 4.4 and is used to characterise the degradation of the scintillator bar.

ND280 started taking data).

$$\bar{Q} = A + Be^{\kappa t} \tag{4.4}$$

The statistical uncertainty on the fit is not sufficient due to some bins containing few events resulting in large errors. Instead a "standard-error" like approach, given in equation 4.5, has been adopted defining the uncertainty on the MPV in figure 4.13 to be the Landau width, w, divided by the square root of the total number of hits, N. This method allows for more sensible errors to be determined.

$$\sigma_{MPV} = \frac{w}{\sqrt{N}} \tag{4.5}$$

It should be noted that this exponential does not take into account the effects that temperature has on the degradation. The model used treats each data point as being independent, however temperatures are not 100% stable as a function of time and so each data point is not truly independent. Unfortunately, temperature data was unavailable so including the temperature dependence into the model was not possible. Not taking the temperature into account will cause the χ^2 of the fits to be different than they otherwise would be.

4.2.3 Extrapolating Results to Predict the Response of the ECal in the Future

It is possible, using the results of the study, to predict how well the ECal will be functioning at some later date; this is important in planning for the operational life times of next generation experiments. Figure 4.14 shows the current fit to the ageing study extended to 2030 (under the current timetable Hyper-Kamiokande will start taking data in 2026).

Due to the exponential characteristics of the response decay, the scintillators tend asymptotically to some non-zero value. Currently, the ageing study has not given any reason to be concerned with the level the scintillators will be operating at during the HK's operational life time. The extrapolation of the data predicts that the scintillator bars in the DS ECal and those aligned in the z-direction will perform at minimum 60% of the original light yield of the bars at 95% confidence level by 2030. The bars aligned in the x and y directions will perform at 40% of their original light output at the 95% confidence level. At a 68% confidence level the worst any bar orientation is expected to have decayed

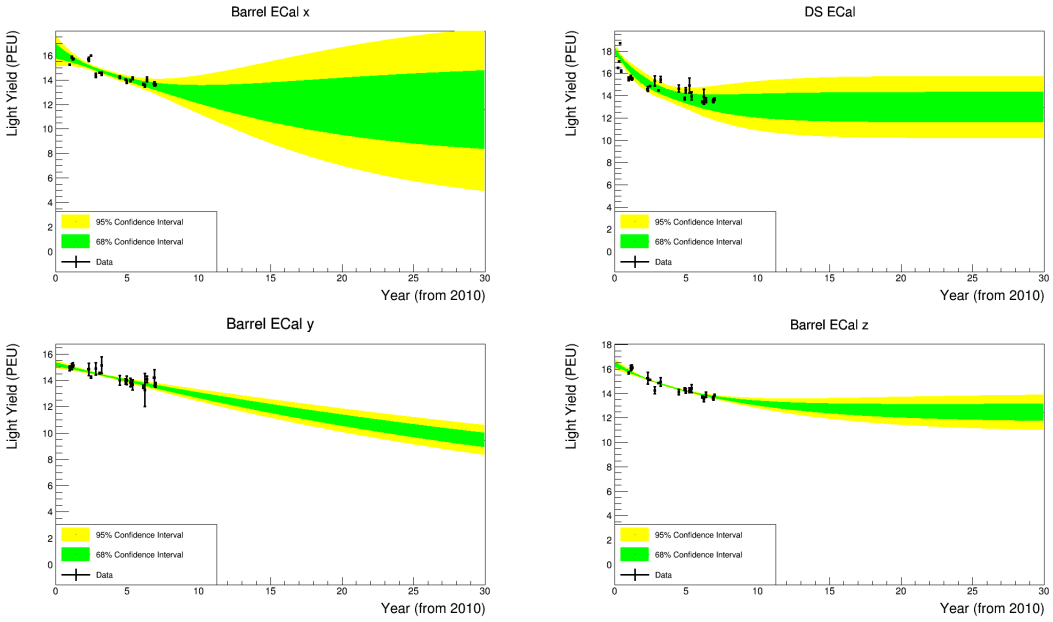

Figure 4.14: The exponential fits for the ageing extrapolated up to 2030. The green band shows a 68% confidence interval on this extrapolation and the yellow band shows a 95% confidence interval.

to is 56% of their original scintillation level.

The data from future T2K data taking runs will be added to these plots allowing for a better understanding of how the scintillators are ageing and how well they are expected to perform moving into the period when the next generation of neutrino experiments are operational. It is important to further monitor the degradation of the bars, as more data is added to the plots the fit that describes the ageing could be better described by a different function, or some event could occur that could cause a greater amount of light loss in the scintillators. Any change in the model will have repercussions for the future prediction as well as the calibration that corrects for the ageing effect.

4.2.4 Correcting for the Scintillator Degradation

Once the ageing of the scintillator bars has been characterised, it is then possible to implement a correction within the calibration software that allows for a flatter distribution of MPV charge in the ECal with respect to time. The correction uses the results from the study to make it appear that the scintillator bars used have not aged since data taking began in 2010. The function, $f(t)$, was defined to correct for the degradation of the ECals.

$$f(t) = \frac{(A+B)}{A + B\exp^{\kappa t}} \tag{4.6}$$

Here A represents the initial value of charge deposited within the scintillator bar and C is the y-offset which is the minimum value of charge is predicted that the ECal scintillators should to. The parameter κ is the decay constant and the $(t - t_0)$ term corrects for the time offset so that the 1^{st} of January 2010 is the initial time in the correction. Figure 4.15 shows the effect of this correction on the data.

4.2.5 Conclusion

The degradation of the scintillators used within the ECals can be described by an exponential model. The ageing can be parameterised for each ECal module using MIPs and studying how the total charge deposited per track length varies with time in a specific module. The function of time plots show an exponentially decreasing trend with a decay constant of approximately 4-5 years for most of the ECals. Since ND280 first started taking data in 2010, the light output from the plastic scintillator bars used in the ECals has dropped by 10-15% across all the ECal modules.

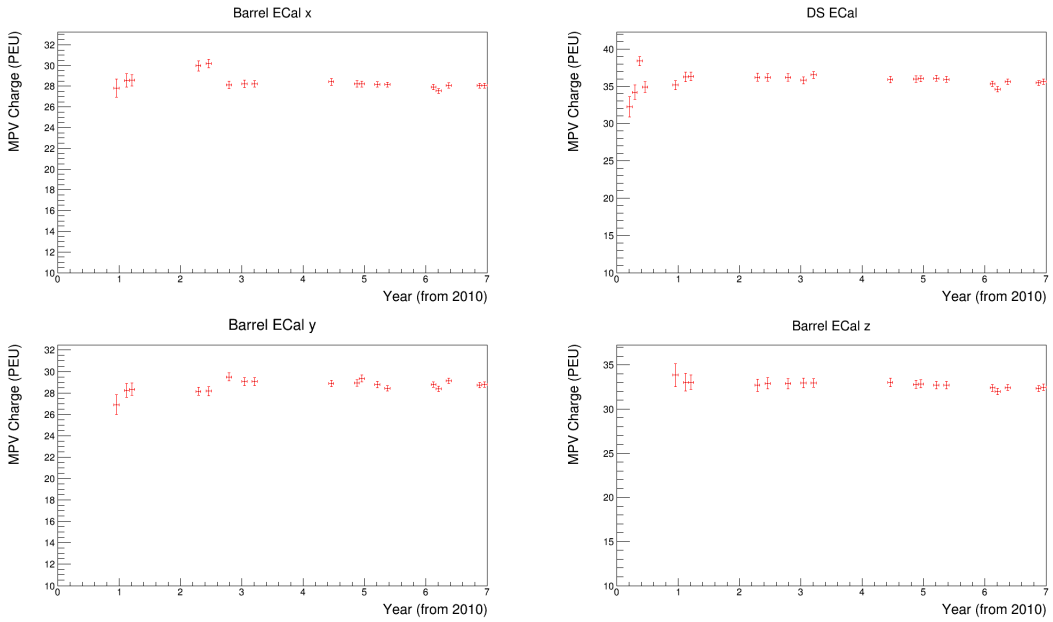

Figure 4.15: The corrected data (red) as a function of time for the ECal plotted by bar type.

At worst the ECals are predicted to have approximately 60% loss of light collection for the Hyper-Kamiokande era. Though this is a significant amount of light loss the underlying causes are understood and the effect is well modelled with the available data. The correction based on this data is therefore able to calibrate the ECals appear as though they have not degraded at all.

Chapter 5

Measuring the NC0π Cross Section

For long baseline neutrino experiments, such as T2K and the proposed Hyper-K experiment, CCQE interactions are the dominant process through which the neutrino interacts. CCQE interactions will also be the dominant interaction process for DUNE at the second oscillation maximum. Though there has been significant effort in measuring quasi-elastic interactions, they are still poorly modelled.

The NCE channel, though experimentally more challenging, can provide a complimentary measurement to the CCQE channel. As mentioned, there exists some tension between data sets which have been used to determine the value of the axial mass parameter via CC interactions. Data sets which have used heavier nuclei as a target, such as the MiniBooNE result, have reported a value of M_A $\sim$30% larger than the values found from bubble chamber experiments, which made use of hydrogen and deuterium as target [37]. Models have been developed and shown to account for the difference which has been observed, however, it is still unclear which, if any, of these models are correct [57; 58].

A correct model of neutrino interactions should be able to describe both CC and NC interactions simultaneously. Simultaneous measurements of both channels could allow models to be constrained and potentially allow for models to be discriminated from one another. A measurement of the neutrino-proton neutral current cross section with no pions in the final state will now be presented.

5.1 Cross Section Extraction

The cross section is calculated using the following formula

$$\sigma = \frac{N_{data} - N_{bkgd}}{N_{nuc} \times \varepsilon \times \int_{0\text{GeV}}^{30\text{GeV}} \Phi_{E_\nu} dE_\nu} \tag{5.1}$$

where the number of background events, N_{bkgd}, is subtracted from the number of signal events, N_{data}. The signal efficiency is denoted by ε and Φ_{E_ν} is the neutrino beam flux. The N_{nuc} variable accounts for the number of nucleons in the FGD 1 fiducial volume.

The total flux integrated cross section will be reported. As the number of background events is subtracted from the total number of signal events detected this measurement will serve to set an upper limit for the NCE cross section on carbon.

The number of target nucleons must be accounted for in order to quote a result for the NCE interaction on a nucleon. To calculate the number of nucleons in the fiducial volume the density per centimeter squared is multiplied by the number of XY modules found in the FGD1 FV, the area of each XY module and by Avoagadro's number. The number of XY modules in the FGD1 FV is 14. One complexity to consider in this calculation is that the FGD1 is comprised of a number of different nuclei, the density of each must be accounted for which is done using table 5.1. The area of each XY module is 30,590 cm^2 [111].

Nuclei	Area Density [g/cm^2]	Number of Nucleons
C^{12}	1.849 ± 0.0092	$(4.77 \pm 0.02) \times 10^{29}$
O^{16}	0.079 ± 0.0048	$(2.05 \pm 0.12) \times 10^{28}$
H^{1}	0.158 ± 0.0021	$(4.07 \pm 0.01) \times 10^{28}$
Ti^{48}	0.036 ± 0.0059	$(9.16 \pm 1.52) \times 10^{27}$
Si^{28}	0.022 ± 0.0043	$(5.62 \pm 1.11) \times 10^{27}$
N^{14}	0.003 ± 0.0021	$(7.99 \pm 5.41) \times 10^{26}$
Total	2.147 ± 0.0144	$(5.54 \pm 0.04) \times 10^{29}$

Table 5.1: Table of the number of nucleons in the FGD 1 fiducial volume used in this analysis.

The total number of nucleons is found to be $(5.54 \pm 0.04) \times 10^{29}$ and is in agreement with the number of nucleons reported in previous T2K cross section analyses [112]. The integrated neutrino beam flux is determined to be $(1.47 \pm 0.12) \times 10^{13}$ neutrinos cm^{-2}.

5.2 Implementation

In this section, the input data and MC as well as the software used in the analysis is presented. The analysis was developed using both C++ and Python programming languages. It was developed blind meaning that only Monte Carlo was studied while the analysis was developed; data was looked at when the final result was extracted.

5.2.1 Input Data and MC

The analysis was developed using Monte Carlo (MC), which was processed by the ND280 computing group using official software. Production 6B, which was used for the MC, was produced using v11r31 of the ND280 software and GENIE version 2.8.0. This analysis makes use of MC from T2K data taking runs 2 - 4, using both water and air configurations (here water refers to the P0D water pouches being filled and air signifies that they are empty). Production 6M is the recommended processing for real data by ND280's computing group, and is used for the data in this analysis. It is based on v11r35p5 of the ND280 software and includes the most up-to-date calibrations. Run 1 was not included as a number of changes were made between run 1 and run 2; these changes include the barrel ECal being installed and properties of the beam changing. Run 1 contains little data and its inclusion in the analysis would not make any significant difference. A full breakdown of the MC POT of each run is included in table 5.2. Data from T2K runs 2 through to 4 was used in this analysis, equating to a total POT of 6.78×10^{20} for data.

	MC POT $[\times 10^{21}]$
Run 2 Water	1.21
Run 4 Air	3.73
Run 2 Air	9.36
Run 3 Air	3.25
Run 4 Water	3.73

Table 5.2: Table of MC POT used in this analysis. Water refers to the P0D water bags being filled with water and air refers to them being empty.

5.2.2 Python Analysis Package

The NCE analysis package t2k-phys-ndfgd, developed in Python, is independent of the ND280 software framework and stored in a private repository.

The Python package fits the number of events in the control samples to measure the out-of-fiducial-volume (OOFV) background seen in the signal sample. In addition to this the flux, cross section and some of the detector systematics are evaluated within the framework. The package makes use of T2KReWeight v1r25 in order to study the cross section systematics, to negate the need for re-running large amounts of Monte Carlo.

5.2.3 HighLAND 2 Software

HighLAND 2 (High Level Analysis at the Near Detector 2) is a software package which was developed for analyses which makes use of T2K's near detector, ND280. For this analysis a new analysis package was developed using v2r11p1 of the HighLAND 2 software. Initially the analysis files produced by the ND280 computing group are reduced in size and saved as "mini trees" which allows for faster processing. The mini trees are then able to be analysed using the NCE analysis package.

The HighLAND 2 software contains many packages developed by different analysis groups on ND280. Alongside these packages, a number of tools have been implemented which can be used across different analyses. These include tools for plotting, methods that apply various cuts to the data and MC, and corrections which can be applied to both data and MC. Also included are a number of systematics that have been previously evaluated for analyses. This analysis has made use of a number of these features.

There are core packages in the HighLAND 2 framework which the analysis makes used of. The HighLAND Tools package contains a number of classes which have core tools that other HighLAND packages make use of. These classes include tools used for producing visual representations of the data, a base class which handles reading and writing the data as well as looping over the events, and parameters which can turn systematics and corrections on and off. The HighLAND IO package handles the interface between the input files which are oaAnalysis files or HighLAND 2 flat/mini trees and the HighLAND Tools package.

The baseAnalysis package provides the user with basic analysis framework on which more complex analyses can be developed. The basic analysis applies data quality checks and corrections to the data as well as providing a framework in which a number of systematics can be evaluated. The basic analysis package also saves standard variables with the ability to add further variables to a ROOT tree which can be used by an analyser. For the NCE analysis a new package called nceAnalysis was created in which the selection was

implemented. A number of detector systematics were evaluated using this analysis package.

5.2.4 Corrections

When the data and MC are in disagreement, and this disagreement is well understood; such as there being a hardware failure e.g. dead channels, or the disagreement has been studied using control samples, a correction is applied to allow for better data/MC agreement. The corrections which have been applied to the data and MC in this analysis are as follows

Data Quality Correction: The data quality corrections corrects data quality flags for data. For the periods

- 22/03/2010 20:52 to 23/10/2010 13:53
- 16/04/2010 15:13 to 16/04/2010 17:16
- 26/05/2010 15:41 to 01/07/2010 00:00

the data was flagged as being good quality. However, during these periods a Front End Board (FEB) for one of the FGDs was not working. This correction changes the data quality flag to bad for these periods.

TPC Energy Loss: Corrections are applied to the energy loss in the TPC, dE/dx, and are applied to both the data and MC. The energy loss in the TPC is re-evaluated with updated parameters which are used in the dE/dx calculation. The mean energy loss is evaluated at the truth level and a comparison between data and MC is made using different control samples for each particle type. In addition to this the data and MC are normalised. The overall effect of this correction is a better estimation of the TPC pulls and subsequently better PID. This correction is evaluated by taking the difference between the mean values of the pull between data and MC.

TPC PID Pull: In addition to the correction to the TPC energy loss, a further correction is applied so that the TPC pull is centered around 0.

Momentum Resolution: This correction applies an additional smearing to the TPC momentum as well as an overall smearing to the momentum of a global track. This correction was studied using a control sample of tracks which cross multiple TPCs and comparing the momentum in each TPC.

5.3 Event Generator Studies

The event generator NuWro was used to carry out an initial study on NCE interactions in ND280; it was chosen for this study as it was one of few generators which included a 2p-2h component in their NCE model. The purpose of this was to study whether a difference could be seen between models that include 2p-2h and models that do not. The study compared the predictions for nominal NuWro to NuWro with the Transverse Enhancement Model (TEM) turned on (details of the model can be found in [102]). The event topologies of interest were CCQE interactions with either 1 or 2 protons in the final state and NCE interaction with either 1 or 2 protons in the final state.

The NuWro events were generated using the pre-defined T2K beam specifications with carbon as target. The interactions which were included were CCQE and NC interactions along with CC and NC Meson Exchange Current (MEC) interactions. The BBBA05 dipole form factors are used. The results from these models were compared to the NuWro nominal model which does not include any MEC models. The generation of these events include no spectral function, no RPA and no flux correction but does include Pauli blocking.

Comparing the interactions in which there are two protons in the final state, as shown in figure 5.1, an enhancement of $\sim 90\%$ is observed in the CC channel. For the NC channel a smaller enhancement of $\sim 60\%$ is seen. The T2K collaboration have put extensive effort in measuring and understanding the the CC channel, but are yet to provide the complimentary measurement of the NC channel.

5.4 Samples

The analysis consists of a signal sample and two control samples which will now be discussed. The samples are based on simple cut based selections which veto unwanted events. The two control samples provide a way of measuring the dominant background to this analysis which will be seen to be out-of-fiducial-volume (OOFV) neutrons. The control samples will be discussed in section 5.4.2.

5.4.1 Signal Sample

The signal is defined to be one or more protons coming from a neutrino interaction in the FGD1 fiducial volume (FV) with no pion present. The main track is the highest momentum track which starts in the FGD and enters the TPC. The fiducial volume of FGD1 is defined

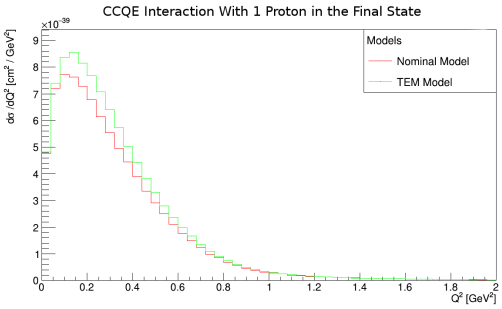

(a) CCQE with 1 proton in the final state.

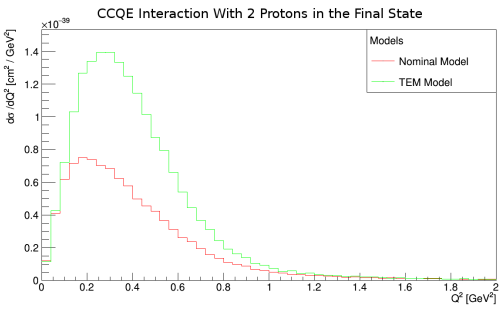

(b) CCQE with 2 protons in the final state.

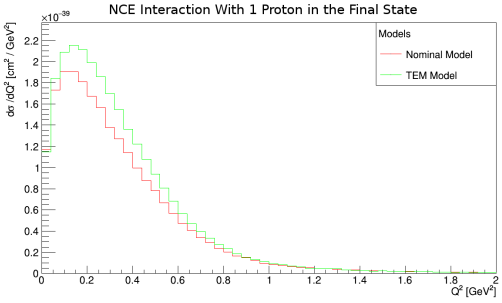

(c) NCE with 1 proton in the final state.

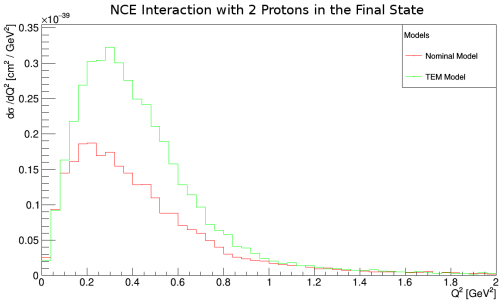

(d) NCE with 2 protons in the final state.

Figure 5.1: The differential cross section as a function of Q^2 for CCQE and NCE interactions with 1 and 2 protons in the final state. The red line shows the prediction of the nominal model in NuWro whereas the green line is the TEM implemented in NuWro.

to be $|x| < 87.51$ mm, $|y - 55| < 874.51$ mm and $136.875 < z < 447.375$ mm in the ND280 global co-ordinate system. The selection is as follows:

Data Quality: The ND280 group, as well as the beam group, monitor the data which is collected and assign flags to data to indicate whether or not it is good or bad. This includes monitoring all aspects of the beam via the beam monitors, the horns and the sub-detectors to ensure everything is working correctly. The data quality checks are done on a spill-by-spill basis. For a spill to make it past this cut and into the analysis the data must be good quality, which is denoted by being flagged as good.

Track Multiplicity: This cut ensures that only events in which there is at least one track reconstructed within a TPC enter the selection.

The next stage in the event selection is to look for one or more protons coming from the interaction vertex by applying cuts to the main track.

Positive TPC Track: One identifying feature of a proton in the detector is the presence of a positive track. The charge of the track is ascertained by its curvature caused by the magnetic field; forward going positive tracks in the detector curve upwards. Any event which contains a negatively charged track is rejected.

TPC Quality: A track must have at least 18 hits in a TPC in order for it to be identified as a good quality track. Fewer hits within the TPC leads to a less reliable measurement of the particle's momentum as well as a more uncertain PID. Short tracks therefore are not considered in this analysis.

TPC Proton PID: This cut is included to ensure only proton like tracks make it through to the analysis. The pull is defined to be

$$\delta_i = \frac{dE/dx^{meas} - dE/dx_i^{exp}}{\sigma_i^{exp}} \tag{5.2}$$

where dE/dx^{meas} is energy loss measured in the TPC. For any given particle hypothesis, i (i = muon, electron or proton), dE/dx_i^{exp} is the expected energy loss. The variable σ_i^{exp} is the resolution of the deposited energy. Using equation 5.2, only tracks with a pull value in the range of -3.5 to 3.5 make it past this cut as shown in figure 5.2.

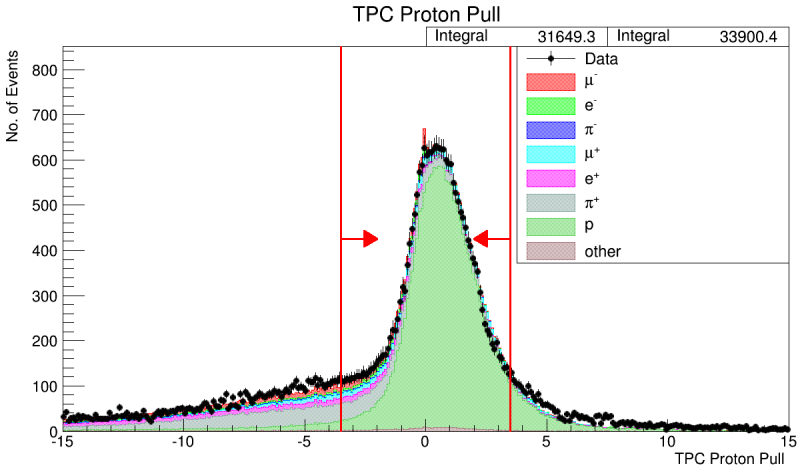

Figure 5.2: TPC proton pull for different particle types. The red arrows show the range in which tracks are accepted as being proton-like. The plot is POT normalised.

A number of events pass the previous cuts which are not protons produced in NCE interactions and enter the selection as background events. The remainder of the selection is intended to veto these unwanted events. Unlike the cuts which are used to select protons, the following vetoes unless stated, are applied to all tracks in an event.

Negative TPC Tracks Veto: From the definition of the signal used in this analysis, an NCE event should only contain positive tracks. If an event contains a negative track the event is identified as not a signal event and is vetoed from the selection.

TPC Muon Veto: Any event which contains a muon cannot be an NCE event and therefore is vetoed from the selection. Events containing muons are rejected by comparing the TPC response against the muon hypothesis as shown in figure 5.3.

ECal Veto: The ECal veto is defined to be events in which there is at least one track in the ECal and no tracks in either the FGDs or TPCs. Any such event is then vetoed from the selection.

FGD-to-ECal Veto: The FGD-to-ECal veto removes tracks in either FGD1 or FGD2 which have no TPC component but do contain a track in the ECal.

Michel Tag: Michel electrons are produced in muon decay as shown in figure 5.4. The

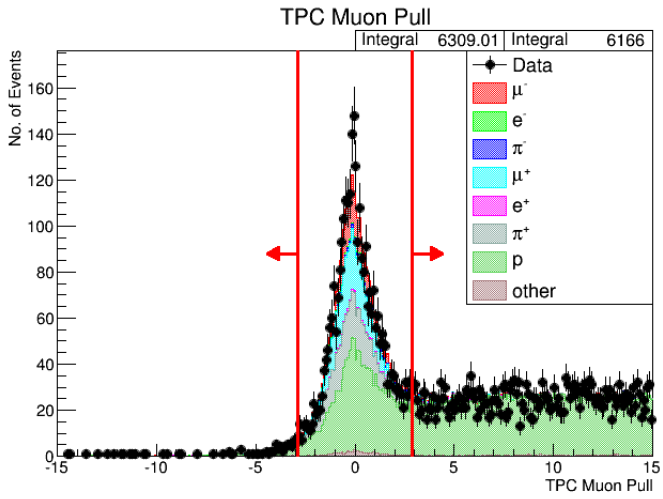

Figure 5.3: TPC muon pull plotted by different particle types. The red arrow shows where the cut is applied.

criteria for a Michel electron is defined separately for FGD1 and FGD2. If an event has at least one out-of-bunch FGD time bin, it can be considered to contain a Michel electron if it has 7 hits in FGD1 (5 hits in FGD2) and the event has occurred in the main track [103]. If an event is identified to contain a Michel electron the event is vetoed from the selection.

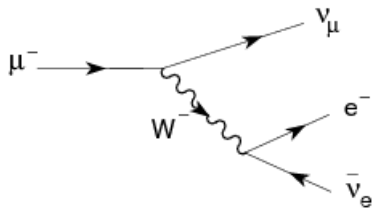

Figure 5.4: The muon decay process.

FGD Veto: This sample requires the proton to enter a TPC from the FGD. Any FGD event with no TPC component are vetoed from the selection.

P0D Veto: A number of OOFV neutrons were identified to have originated in the P0D. For an event to be successfully reconstructed in the P0D, the track must have four

hits. Vetoing all events with four or more hits from the P0D therefore reduced the OOFV neutron background.

P0D ECal Veto: Similar to the P0D veto, the P0D ECal veto removes events originating in the P0D ECal as a number of OOFV neutrons which entered the selection were produced in this sub-module.

Reduced Fiducial Volume: This cut is applied to the main track in the event and vetoes events in the last two layers of the FGD fiducial volume. The cut only accepts tracks with a start position of $z < 400.0$ mm in the ND280 global co-ordinate system.

5.4.1.1 NCE Selection

It is found by studying the MC, after all cuts are applied, that the purity of the signal sample is found to be 47.9% with an efficiency of 40.1%. The figures in 5.5 show how the purity and efficiency of the sample evolves with each cut. Table 5.3 shows the final purities for the signal and each background. The dominant background remains as OOFV neutrons making up 29.7% of selected the events. Figure 5.6 show the proton kinematics and $\cos\theta$ distributions for the selected proton in the signal sample. The variable $\cos\theta$ is defined to be the angle between the z-direction and the direction of motion of the proton produced at the interaction vertex.

Topology	Event Sample Fraction [%]
NC 0π	47.9
NC Background	8.4
CC Background	9.9
OOFV Neutrons	29.7
OOFV Protons	3.6
Other	0.1

Table 5.3: Table of purities by interaction topology.

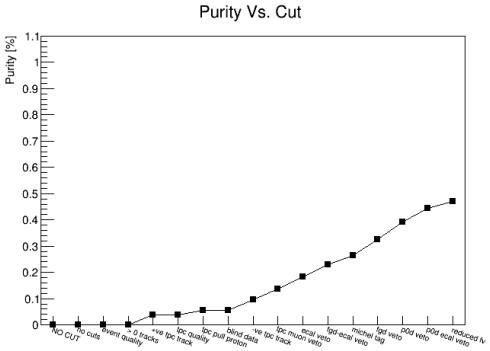

(a) Purity of the signal sample against cut

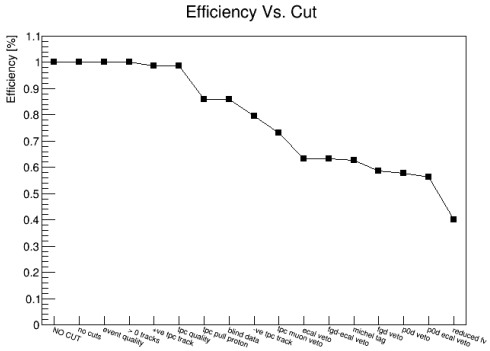

(b) Efficiency of the signal sample against cut

Figure 5.5: Plots showing how the purity and the efficiency of the signal sample evolves with each cut

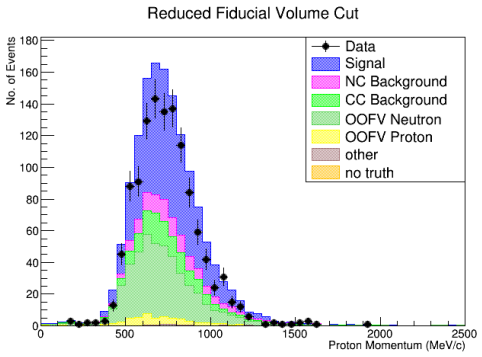

(a) Proton Kinematics

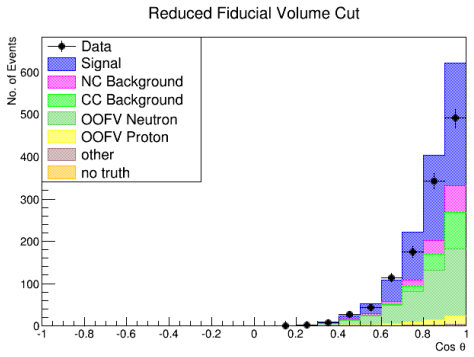

(b) Proton $\cos\theta$

Figure 5.6: Proton kinematics and $\cos\theta$ plots after all cuts for the signal sample

5.4.1.2 Timing

In an attempt to further remove OOFV neutrons from the selection, the time information of the events was studied shown in figure 5.7. The separation, in time, between signal events and events from the OOFV background is approximately 5 ns. The width due to the beam is approximately 12 ns. Due to the lack of sensitivity to the OOFV background timing information was deemed to be of little use to veto further OOFV background events.

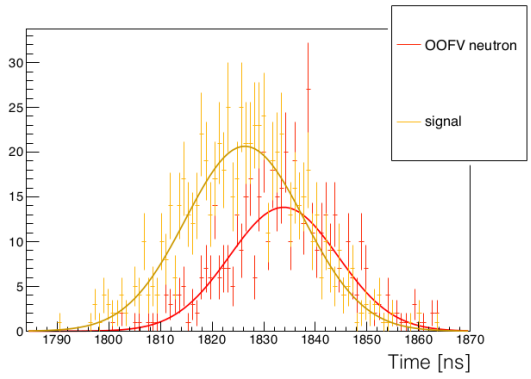

Figure 5.7: MC timing information for true signal events and true OOFV neutrons which dominate the background in the signal sample.

5.4.2 Control Samples

The two control samples are defined to contain the background with minimal signal contamination. The signal sample, P0D sample and SMRD sample all have a number of cuts in common, listed below:

- Data Quality
- Positive TPC Track
- TPC Quality
- TPC Proton PID
- Negative TPC Track
- TPC Muon Veto

These cuts are applied in the same order as in the signal sample. Only the final cuts in each control sample will now be presented.

5.4.2.1 P0D Control Sample

The P0D was identified as being one source of OOFV neutrons in the selection for the signal sample. These OOFV neutrons were vetoed from the selection using the P0D veto. The P0D control sample uses the P0D to define a sample which has a large number of these events with a small number of signal events entering the sample.

Inverted P0D Veto: The inverted P0D veto only allows tracks with at least one object reconstructed in the P0D to pass it. A number of OOFV events were seen to be coming from the P0D in the signal sample. Inverting the veto on the P0D events produces a P0D control sample. This contains sufficient P0D-induced OOFV background which will be able to be used as a constraint on this background source.

Below, figure 5.8 show the proton kinematics and $\cos\theta$ distributions for the P0D sample after all cuts. Table 5.4 breaks down the selected events in the P0D sample by event topology.

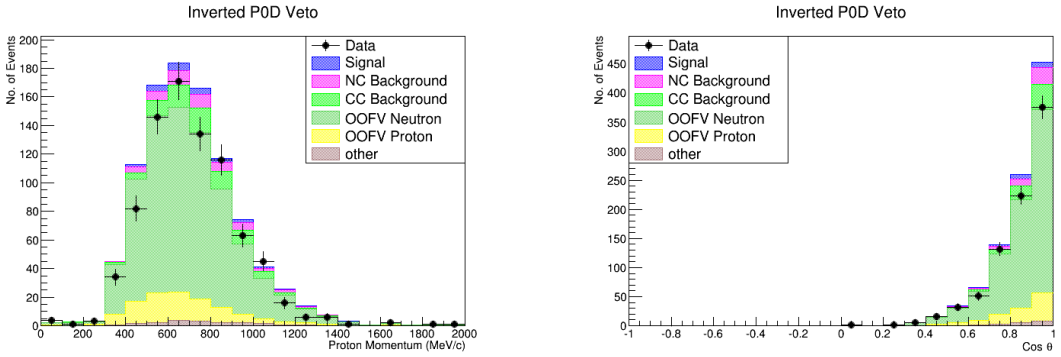

(a) Proton momentum distribution

(b) Proton angular distribution

Figure 5.8: Proton kinematics and $\cos\theta$ plots after all cuts for the P0D sample

5.4.2.2 SMRD Control Sample

The second control sample defined to experimentally measure the OOFV neutron background in the signal sample is the SMRD control sample. This sample contains recon-

Topology	Purity [%]
NC 0π	2.4
NC Background	5.0
CC Background	8.1
OOFV Neutrons	71.3
OOFV Protons	10.7
Other	2.1

Table 5.4: Table of purities by interaction topology for the P0D sample.

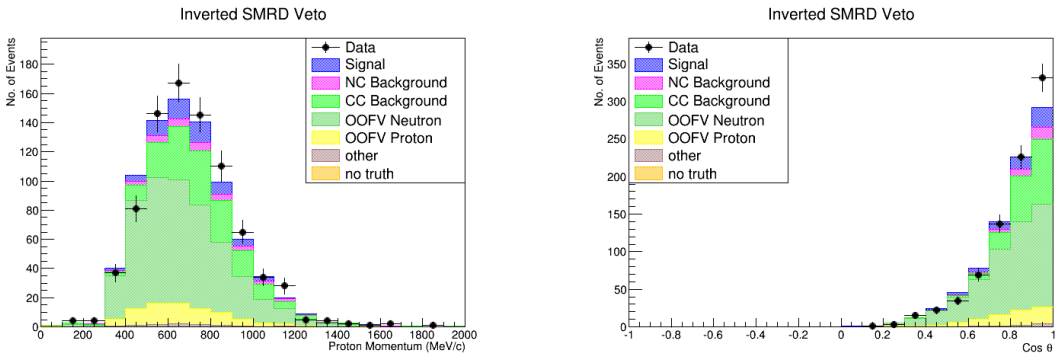

(a) Proton kinematics

(b) Proton $\cos\theta$

Figure 5.9: Proton kinematics and $\cos\theta$ plots after all cuts for the SMRD sample

structed upstream events in the SMRD.

P0D Veto: This is the same veto which appears in the signal sample and removes events which have a P0D component. It is used in the SMRD control sample to remove P0D events from the SMRD veto as these events appear in the P0D sample.

Inverted SMRD Veto: The veto selects events within ± 150 ns of the average SMRD time with a start position of $z < 136.0$ mm in the global ND280 co-ordinate system.

Figure 5.9 show the proton kinematics and $\cos\theta$ distributions for the SMRD sample after all cuts. Table 5.5 describes the SMRD event by the fraction of each event topology which enter the sample.

Topology	Purity [%]
NC 0π	7.5
NC Background	4.0
CC Background	21.9
OOFV Neutrons	56.1
OOFV Protons	9.3
Other	1.2

Table 5.5: Table of purities by interaction topology for the SMRD sample.

5.4.3 Data/MC Agreement in the Control Samples

In order for the OOFV neutron background to be measured using the control samples, good agreement between data and MC must exist. In the control samples detailed above, the data and MC show some disagreement which will affect the final result. The agreement between data and MC will be improved by fitting the number of events in the data in each control sample, this method will allow the MC to model the data better. Good agreement between the data and MC in the control samples will result in a better measurement of the OOFV neutron background which will be used in the final cross section extraction.

5.5 Evaluation of Systematics

The simulation of events within ND280 is not perfect, due to complexities of modelling the detector and the numerous interactions which take place within and around it. To account for these a number of systematic uncertainties are considered including the uncertainty on the flux, detector and theoretical model systematics. Fortunately a number of the systematics in this analysis have been extensively studied by previous analyses. Each type of systematics will now be presented.

5.5.1 Flux Systematic

The flux systematic accounts for the uncertainty on the energy of the neutrinos as well as the uncertainty around the number of each neutrino flavour present in the beam. There are a number of contributing systematics to the flux systematic which usually result in it being the largest for source of uncertainty in cross section measurements on T2K. The largest contribution to the flux systematic is the uncertainty in hadronic production pro-

cesses. In order to constrain this uncertainty and to fine tune the nominal flux, external data from NA61/SHINE at CERN is used [104]. The NA61/SHINE experiment studies hadron production from different interactions including hadron-proton, hadron-nucleon and nucleon-nucleon processes.

Pion production at the target can effect the flux of muon neutrinos in the beam. Kaon production, like pion production, can also have an effect on the beam composition by effecting the flux of electron neutrinos. Secondary interactions further effect the composition of the neutrino beam by effecting the number of pions and kaons there are. As neutral current interactions are flavour independent, the flux of electron and muon neutrinos in the beam should have no effect on the signal rate. The flux of each neutrino flavour in the beam can effect the background rate seen in the analysis and as a result can have an effect on the final result.

The number of protons on target must be correctly modelled as this can effect the total beam flux. However, incorrectly modelling the number of protons on target will not effect the energy of the neutrinos nor the total number of each flavour of neutrino that the beam is made of. As well as this the beam normalisation and shape can be affected by the total cross section of protons interacting with the target, therefore the uncertainty in correctly modelling proton interactions at the target must be taken into consideration.

As described in chapter 4, the ND280 detector is 2.5° off of the beam axis resulting in a more peaked energy spectrum for the neutrino beam. Deviation from this angle can effect the energy and the flux of the neutrino beam. The current which the horns are operating at, as well as the alignment of the horns can effect the beam flux. The horn current directly effects the focusing of the beam. Deviations from the operating current of the horn would effect the energy of the neutrino beam. Similarly, if the alignment of the horns differ to what is expected, the beam width and the off axis angle could change resulting in the neutrino energy being altered.

The flux uncertainties are parameterised using 50 parameters. The flux is parameters take into account the neutrino flavour, true energy and beam mode as shown in table 5.6. A covariance matrix is constructed to take into account the correlations between bins. Each bin is then varied within its own error and the resulting effect on the cross section allows for a systematic to be determined.

The T2K beam group provide official T2K flux files containing the flux and flux uncertainty for a different amounts of POT. The flux from these files are summed together and divided by the number of files used to get the correct flux. The flux uncertainty is

Flux	Energy Binning (GeV)	Bin Range in Matrix
ν_μ	[0.0; 0.4; 0.5; 0.6; 0.7; 1.0; 1.5; 2.5; 3.5; 5.0; 7.0; 30.0]	0-11
$\bar{\nu}_\mu$	[0.0; 0.7; 1.0; 1.5; 2.5; 30.0]	11-16
ν_e	[0.0; 0.5; 0.7; 0.8; 1.5; 2.5; 4.0; 30.0]	16-23
$\bar{\nu}_e$	[0.0; 2.5; 30.0]	23-25

Table 5.6: The binning used for the beam flux systematic in neutrino mode.

determined to be 8.58%. See table B.1 in appendix B for a breakdown of each uncertainty relating to the flux.

5.5.2 Detector Systematics

A number of detector effects can have an impact on the selected events. The HighLAND 2 software was used to evaluate how variations in detector properties can alter the events passing each cut in the selection. To evaluate the detector systematics a number of pseudo-experiments were carried out, with a property of the detector varied according to some distribution. For each toy the selection was re-run and the effect on the number of signal and background events was studied allowing for a systematic to be determined. HighLAND 2 categories the detector systematics into three categories which will now be discussed, further information on these systematics can be found in [105].

5.5.2.1 Variation Systematics

For variables where the data and the MC could have a different mean value or resolution, HighLAND 2 applies a type of uncertainty known as a variation systematic. This type of systematic is evaluated by altering the value of a variable and re-running the selection and studying how the total number of events has been affected. The variable is altered according to a distribution recommended by the experts in each detector subsystem and is usually Gaussian. A variable alteration can be described by

$$x^{'}_{rec} = x_{rec} + \delta_{var}\left(x^{alt}_{rec} - x_{rec}\right) \tag{5.3}$$

where x_{rec} and x^{alter}_{rec} is the reconstructed variable before and after it has been altered and δ_{var} is a random variable based on some distribution. The variation systematics which were taken into account will now be detailed.

Magnetic Field: The magnetic field systematic takes into account the fact that the magnetic field used by ND280 could have slight variations in field strength. This systematic was evaluated by varying the momentum of a particle in the TPC while keeping th radius of the track curvature constant.

TPC PID: The TPC PID systematics makes use of energy loss measurements and calculates pulls using equation 5.2. It is important to understand how well the detector is correctly identifying particles, as mis-identification could lead to events with the wrong topology passing the selection cuts. The systematic was evaluated by comparing data and MC pull distributions for each particle hypothesis; the different particle hypotheses are shown in figure 5.10. Estimations can be made using parameters from fits applied to the pull distributions. Comparing the ratio of the data and MC allows for an estimation of the smearing to apply in pseudo-experiments, and the ratio of the pull means gives an estimation of the overall TPC PID systematic.

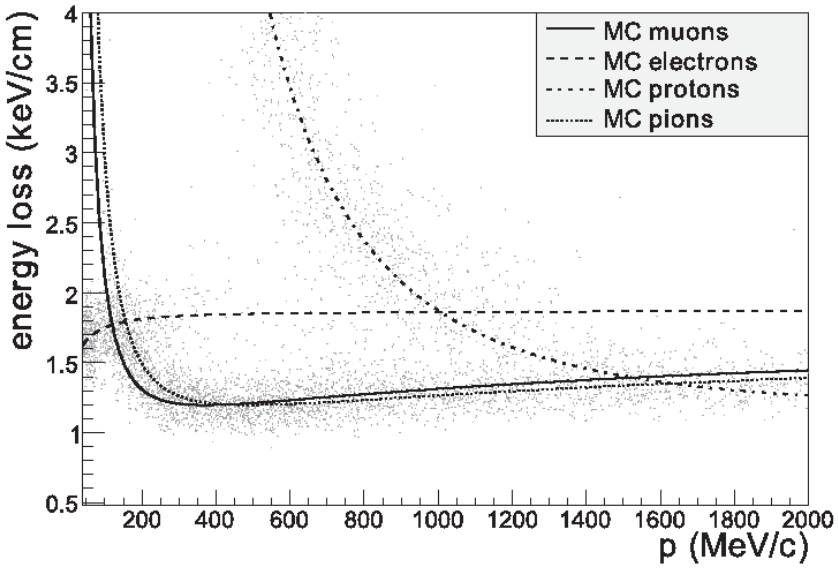

Figure 5.10: Each point shows measurements by a single TPC of the energy loss and momentum of positively charged particles produced in neutrino interactions. The expected relationships for muons, positrons, protons, and pions are shown by the curves. Figure taken from [85]

Momentum Resolution: A control sample is defined so that tracks cross multiple TPCs and by definition the intermediate FGD. The difference between the inverse momentum, $\Delta(1/p_T)$, which has been corrected for energy loss using the FGD, can be described by a Gaussian fit which is centered on 0. The momentum resolution of the TPC is extracted from the standard deviation and can be studied for different momenta, transverse momentum and track angle.

Momentum Scale: The momentum scale systematic is evaluated using a control sample of stopping cosmic muons in the FGD and comparing the momentum to the momentum in the TPC.

5.5.2.2 Efficiency Systematics

Using control samples that are well understood and are dependent on what systematic are being studied, efficiency-like systematics are evaluated by comparing data and MC. Differences in the data and MC efficiency arise due to imperfect modelling of the detector geometry and interactions within the detector. The efficiency for the MC control sample can be calculated using truth information, the efficiency for the data control sample is computed by

$$\varepsilon_{data} = \frac{\varepsilon^{CS}_{data}}{\varepsilon^{CS}_{MC}} \varepsilon_{MC} \tag{5.4}$$

where ε^{CS}_{data} and ε^{CS}_{MC} are the efficiency for the control samples (CS) for both data and MC respectively. The efficiency in the MC sample is denoted by ε_{MC}. Propagation of the systematic uncertainty must take into account the statistical uncertainty of the efficiency computed using the control samples denoted below by $\sigma_{\varepsilon^{CS}_{data}}$ and $\sigma_{\varepsilon^{CS}_{MC}}$ for data and MC respectively. The predicted data efficiency variation is

$$\varepsilon^{'}_{data} = \frac{\varepsilon^{CS}_{data} + \delta_{data} \cdot \sigma_{\varepsilon^{CS}_{data}}}{\varepsilon^{CS}_{MC} + \delta_{MC} \cdot \sigma_{\varepsilon^{CS}_{MC}}} \tag{5.5}$$

where the variations in the number of standard deviations in the data and MC control samples are δ_{data} and δ_{MC} respectively. Finally the weight applied to each event is

$$W_{eff} = \frac{\varepsilon^{'}_{data}}{\varepsilon_{MC}} \tag{5.6}$$

Events contribute to the inefficiency when the truth track is not reconstructed successfully. The inefficiency weight is

$$W_{ineff} = \frac{1 - \varepsilon^{'}_{data}}{1 - \varepsilon_{MC}} \tag{5.7}$$

The efficiency-like systematics taken into account in this analysis are

TPC Cluster Efficiency: The definition of a TPC cluster is a group of adjacent TPC pad hits which are the result of a charged particle ionising the TPC gas as it crosses the detector. The hits are clustered in two orientations: horizontally if the angle of the track relative to the z-axis is greater than 55°, otherwise the track is categorised as vertical. It is important to understand how often the clustering algorithm correctly clusters tracks together. This systematic is studied via data/MC comparisons of vertical and horizontal track control samples. A control sample of cosmic muons with a data quality cut requiring the event to have a TPC track containing 18 or more hits is used to compute the systematic. The number of events passing this cut will be affected by how well the clustering algorithm is working.

TPC Track Efficiency: This systematic takes into account how well the TPC reconstruction successfully reconstructs tracks which have a TPC component. It is evaluated using control samples consisting of through going muons from both beam and cosmic triggers. Studies have concluded that the TPC reconstruction performs well and is independent of momentum, angle and length of the track in the TPC as well as being unaffected by another track in the same TPC.

TPC-FGD Matching Efficiency: This systematic accounts for how often the reconstruction software correctly matches a track in the TPC to its counterpart in the FGD and accounts for any differences between data and MC. Incorrectly reconstructing events which pass from the FGD into the TPC could lead to signal events being vetoed from the selection. Through going muons are used to evaluated this systematic.

Charge Identification: The electric charge of a particle can be assigned the wrong sign by the global reconstruction. The probability that the global reconstruction misidentifies the charge of a track depends on the length of the track, the momentum, the curvature and the number of hit is a TPC segment. There is a correlation between the number of TPC segments and the charge identification of a global track, as the

identification is dependent on the segments predicting the same charge. The probability of the global track conserving the charge is calculated by data/MC comparisons for different number of TPC segments in the global track where the sign in one TPC segment is in disagreement. This allows for the determination of a weight to apply.

Michel Tag: As described in section 5.4.1, the identification of an event with at least one delayed out-of-bunch FGD time bin with a certain number of hits in the FGD, is considered to contain a Michel electron. The selection uses a Michel tag to identify and remove CC interactions. Misidentification of Michel electrons can lead to CC events making it into the selection. The efficiency for detecting Michel electrons is calculated using external background from in-magnet interactions.

5.5.2.3 Normalisation Systematics

Some sources of systematic uncertainty effect the global normalisation of the cross-section measurement; these are treated by re-weighting the event. The weight applied is

$$W = W_0 \left(1 + \delta \cdot \sigma_W\right) \tag{5.8}$$

where W is the calculated weight which will be applied to the MC and W_0 is the weight applied to MC in the absence of systematics. The two variables δ and σ_W are the variation in number of standard deviations and the systematic error on the normalisation respectively. The number of events after the normalisation has been applied, $N^{'}_{total}$, is calculated by

$$N^{'}_{total} = W \cdot N_{total} \tag{5.9}$$

The normalisation systematics are

FGD Mass: The number of interactions that occur is related to the number of nucleons present in the target material. The mass of the FGD is not precisely known and thereby there is some uncertainty associated with the mass of the FGD. This uncertainty has been determined to be less than 0.7%.

Pile Up: Interactions can occur in the material which surrounds the detector, known as sand muon events, which can cause tracks to be observed in the detector. Sand

muon events are not simulated in GENIE. The pile up systematic can be evaluated by calculating the efficiency of the number of bunches passing each veto cut

$$\varepsilon = \frac{\text{Number of bunches passing reconstruction cuts}}{\text{Number of bunches}} \tag{5.10}$$

A systematic can be computed from the difference between the efficiency in data and MC. Using this method the total pile up systematic is evaluated to be ∼7%. The results are broken down by veto cut in the table 5.7.

Cut	Data	MC	Difference
All Veto Cuts	0.80	0.87	-0.07
ECal Veto	0.88	0.91	-0.03
P0D ECal Veto	0.94	0.97	-0.03
P0D Veto	0.94	0.98	-0.04
FGD Veto	1.00	1.00	-0.00
Michel Tag	0.99	1.00	-0.01

Table 5.7: Evaluation of the efficiency of number of bunches passing each veto cut used to calculate the pile up systematic.

Secondary Interactions (SI): The secondary interactions systematic is separated into three categories: Neutron SI, Proton SI and Pion SI. Neutrons, protons and pions which are produced in interactions can undergo further interactions within the detector once they have left the nucleus. These interactions can cause the particle to not be observed resulting in the event being misidentified.

The pion and proton SI systematic is implemented with in the HighLAND 2 framework, whereas the neutron SI systematic is motivated by GEANT4 validation plots shown in figures 5.11. Approximately 20% of the neutron background in the signal sample undergo a secondary interaction before entering the FGD. The uncertainty on the neutron SI is determined to be 10% from the GEANT4 plots, resulting in a 2% effect on the total background normalisation.

5.5.3 Theory Systematics

A number of parameters are used in cross section models to describe neutrino interactions and these parameters have uncertainties associated with them. The uncertainties on the

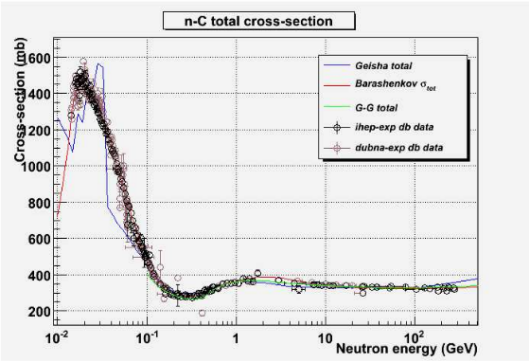

(a) GEANT validation plot of neutrons on carbon total scattering cross section.

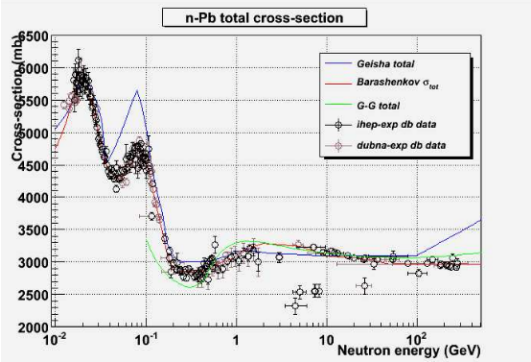

(b) GEANT validation plot of neutrons on lead total scattering cross section.

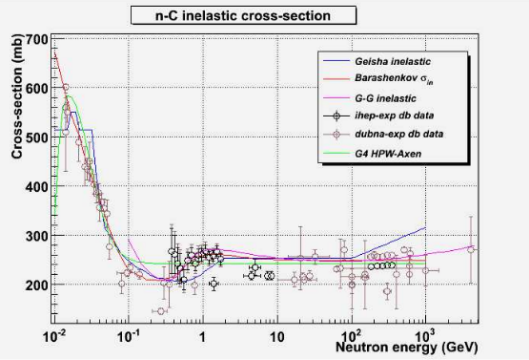

(c) GEANT validation plot of neutrons on carbon inelastic scattering cross section.

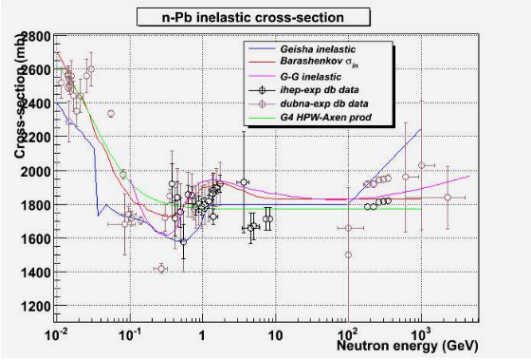

(d) GEANT validation plot of neutrons on lead inelastic scattering cross section.

Figure 5.11: GEANT4 validation plots used to motivate the neutron secondary interaction systematic. Data from the Dubna and IHEP experimental databases is compared to different cross section models in the GEANT4 package. Plots taken from T2K technical note 131 [106].

model predictions are propagated in a similar fashion to the detector systematics. Each physical parameter, P, in the model is varied by the following equation

$$P^{'} = P \cdot \left(1 + x_P \cdot \frac{\delta P}{P}\right) \tag{5.11}$$

Here the term, x_P, has been introduced to modify the value of the parameter. The events are reweighted using a value of x_P, calculated using a Gaussian distribution with the mean value set to 0 and a standard deviation of 1. The term δP is the estimated standard deviation of the nominal value of P. Altering a parameter will affect the probability that an interaction will occur by causing a change in the predicted cross section. Each event then has a weight applied to it

$$w = \frac{d^n\sigma_\nu^{'}/dK^n}{d^n\sigma_\nu/dK^n} \tag{5.12}$$

Here the numerator is the differential cross section for kinematic phase space K^n, such as Q^2, based on the altered input cross section parameters. The denominator is the nominal differential cross section. It is used to propagate the errors on the parameters of the cross section model, allowing the uncertainty on the input parameters without the need to re-run the MC simulation. The T2KReWeight software framework was used to determine the total uncertainty on the cross section model.

This analysis made use of the GENIE uncertainties which are provided for the numerous parameters found in the generator. For a full list of the uncertainties included in GENIE see [107]. In chapter 3, the NCE axial form factor was parameterised in terms of the axial mass of NC elastic interactions and a strange axial form factor. These parameters are included in GENIE and are assigned relative uncertainties, $\delta P/P$, of $\pm 25\%$ for the NCE axial mass and $\pm 30\%$ for the strange axial form factor.

There may be some double counting of uncertainties due to the correlation of the uncertainty between the efficiency and background term being ignored in the final cross section calculation. The signal parameters can contribute to the error on the background, for example, an OOFV neutron background might be caused by an external NCE event so that the M_A for NCE interactions could effect the value of N_{bkgd} in equation 5.1.

5.5.4 Signal Efficiency

The absolute efficiency, computed using the Python analysis framework, is $(8.8 \pm 2.4)\%$. This value was calculated by

$$\varepsilon_{abs} = \frac{\text{Total number of NC0}\pi \text{ events selected}}{\text{Total number of NC0}\pi \text{ events}} \tag{5.13}$$

The signal efficiency uncertainty was studied by comparing the GENIE sample to NuWro in four different combinations: Nominal, No FSI, SF and TEM. To evaluate the uncertainty on the signal efficiency the HighLAND 2 analysis framework was used. The efficiency was calculated by

$$\varepsilon_{rel} = \frac{\text{Total number of NC0}\pi \text{ events selected with a TPC component}}{\text{Total number of NC0}\pi \text{ events with a TPC component}} \tag{5.14}$$

The difference between the relative efficiencies in the GENIE sample and the different NuWro samples was taken to be the uncertainty. The NuWro files were generated using NuWro 11o, simulating 500,000 events in the FGD 1 fiducial volume, with the following parameters as default:

- QE: Dipole form factors with the CC axial mass parameter defined to be 1.2 GeV (this value is different than the one used in GENIE due to NuWro using the dipole form factor and GENIE using BBBA05 parameterisation)
- RES: Dipole form factors with the axial mass parameter defined to be 0.94 GeV
- Nuclear Model: Local Fermi gas
- MEC/np-nh model: Nieves (CC interactions only, no NC MEC implemented)
- FSI: Cascade using formation zone

A description of each NuWro configuration can be found below. All other parameters are kept unaltered:

Nominal: This sample refers to NuWro with its settings set to their default values as described above.

No FSI: This sample is simulated without FSI/cascade mode turned on.

SF: This sample uses the spectral function instead of the default local Fermi gas as nuclear model.

TEM: The NC MEC/np-nh model implemented in NuWro is the TEM model. This sample has this model turned on.

Sample	Signal Efficiency [%]
GENIE	40.1
NuWro - Nominal	52.4
NuWro - No FSI	53.8
NuWro - Spectral Function	51.3
NuWro - TEM	52.1

Table 5.8: The signal efficiencies for the GENIE sample and NuWro samples.

Table 5.8 shows the signal efficiency for each sample after all selection cuts. The greatest difference is between the GENIE sample and NuWro with no FSI which is approximately 14%. The NuWro files only have events generated starting in the FGD1 fiducial volume, however, a number of vetoes remove events with starting positions outside of this detector volume. The GENIE/NuWro comparison is therefore not a fair comparison and the signal efficiency study was repeated with these vetoes removed from all samples.

Sample	Signal Efficiency [%]
GENIE	47.8
NuWro - Nominal	54.9
NuWro - No FSI	56.1
NuWro - Spectral Function	53.7
NuWro - TEM	54.6

Table 5.9: The signal efficiencies for the GENIE sample and NuWro samples.

The results of removing the vetoes with events starting outside of the FGD1 fiducial volume is shown in table 5.9. The greatest difference between the samples is approximately 8%. The difference between the GENIE sample and the NuWro sample with the TEM model is $\sim$7%. Using this study, the signal efficiency uncertainty in the cross section calculation will be 7%.

5.5.5 Sideband Efficiencies

The efficiency of the two control samples, P0D control sample and SMRD control sample, defined in this analysis must also be taken into account.

5.5.5.1 P0D Sample Efficiency

A number of previous analyses have studied the efficiency of the P0D such as the P0D CC0π analysis [108]. This analysis studied the P0D-TPC track matching efficiency using FGD triggered cosmic muons. The criteria for events for this study are as follows

- A single global PID object with a TPC1 component
- Number of nodes in TPC1 must exceed 18 to eliminate short tracks from the sample
- Using the ND280 global co-ordinate system a cut is placed on TPC1 reconstructed front position, $z < -755$ mm, corresponding to the first few layers
- The linearly projected position to $z = -1100$ mm in the P0D is within the P0D xy-fiducial plane
- The reconstructed front momentum in TPC1 is greater than 250 MeV

The study looked at samples divided into water-in and water-out and concluded that there were negligible differences between them. Using Corsika-generated cosmics, the study was able to show an "exact 100% MC efficiency". The inefficiency in data was smaller than 0.2% [109].

5.5.5.2 SMRD Sample Efficiency

The efficiency of the SMRD sample is studied by defining a sample of cosmic muons. To select a sample of cosmic muons the FGD cosmic trigger is used to avoid trigger bias from the Trip-t trigger. Muon-like tracks, which have good TPC quality, are selected using the TPC PID. The selected events must also have an ECal energy deposition consistent with a minimum ionising particle and must exit the barrel ECal. The TPC track end, closest to the ECal segment, is extrapolated to the SMRD. Finally, the TPC momentum must exceed 1 GeV to ensure reliable straight line track extrapolation as well as ensuring the

	Data [%]	MC [%]	Data - MC [%]
All Events	84.64 ± 0.04	75.5 ± 0.5	9.2 ± 0.5
Top	80.11 ± 0.06	70.6 ± 0.8	9.6 ± 0.8
Bottom	84.72 ± 0.06	78.5 ± 0.8	6.2 ± 0.8
Left	98.59 ± 0.05	100 ± 0	-1.41 ± 0.05
Right	98.60 ± 0.05	99.3 ± 0.7	-0.7 ± 0.7

Table 5.10: The efficiencies for the SMRD control sample for data and MC evaluated using cosmic muons.

muon candidate reaches the SMRD. In order to evaluate the efficiency systematic for the SMRD sideband, data is compared to MC.

Table 5.10 shows the results from the SMRD efficiency study broken down into four modules: top, bottom, left and right. The side modules (left and right) show little difference in the efficiency between data and MC. The top and bottom modules however show a larger difference between the data and MC. Using the same selection criteria, a sample of sand muons was also used to cross check the SMRD efficiency study. The results are shown in 5.11.

	Data [%]	MC [%]	Data - MC [%]
All Events	77.5 ± 0.05	75.9 ± 0.4	1.7 ± 0.7
Top	52.0 ± 2.0	46.0 ± 1.0	6.0 ± 2.0
Bottom	74.8 ± 0.8	65.6 ± 0.8	9.1 ± 1.1
Left	91.6 ± 0.8	94.0 ± 0.5	-2.5 ± 0.9
Right	92.1 ± 0.8	93.4 ± 0.5	-1.4 ± 1.0

Table 5.11: The efficiencies for the SMRD control sample for data and MC evaluated using sand muon.

The results from the sand muon sample are consistent when broken down by SMRD module. In order to account for the differences in the top and bottom modules an efficiency systematic of 10% is assigned to the SMRD. This uncertainty is comparable with the statistical uncertainty in the SMRD control sample, which will limit the power of the SMRD sample to constrain the background.

5.5.6 Summary of Systematics

A number of systematics have been evaluated for this analysis, the results of which are presented below. The total systematic uncertainty can be divided into three categories: flux, detector and theory systematics. Each systematic is shown in table 5.12. The statistical uncertainty is approximately 4%. The theory systematic is the dominant uncertainty in this analysis.

Systematic	Value [%]
Neutrino Flux	8.6
Theory	22.7
Detector Response	8.3
Total	25.7

Table 5.12: Table of total systematics for the signal sample in the NCE analysis which are added in quadrature.

The total systematic on the detector response for each sample is shown in table 5.13. The SMRD control sample has the largest systematic associated with it due to the SMRD efficiency systematic which is of the order of 10%.

Sample	Value [%]
Signal Sample	8.3
P0D Sample	8.3
SMRD Sample	12.7

Table 5.13: Table of detector systematics for each sample in the NCE analysis.

5.6 Fitting Procedure

The OOFV background is constrained by performing a MINUIT fit [110] to the control samples. The fit is a maximum likelihood fit to the number of events in each control sample. A MINUIT fit minimises a function with respect to a set of parameters. The fit uses the flux, the detector systematics and the default GENIE model parameters as input. Four further parameters are included: OOFV Neutron Scale Carbon/Oxygen, OOFV Neutron Scale Iron/Brass, OOFV Neutron Scale Aluminium and OOFV Neutron Scale Lead. These parameters scale the rate of production of OOFV neutrons on each nucleus without prior

knowledge of how the cross section scales with atomic number. They are ad hoc parameters and do not relate to any physical parameter of the model, they are included so that the MC is not relied upon to get the scaling of the OOFV neutron cross section on various targets correct. The parameters are empirical normalisation parameters that just scale the event rate predicted by the MC. A Gaussian prior is chosen for these four parameters with 100% error to allow the constraint on them to be dominated by the ND280 data.

The likelihood fit is a function of the set of input parameters, θ, and is the sum of the prior likelihood and the data likelihood. It is defined by

$$-2\ln(\theta) = (y-\mu(\theta))^T V^{-1} (y-\mu(\theta)) + 2\sum_{i=1}^{N} [-x_i + n_i \ln(x_i)] \tag{5.15}$$

where the first term is the prior likelihood and the second is the likelihood determined from the data. The prior likelihood contains the following parameters: V^{-1} is the inverse of the covariance matrix of all parameters, y is a 1D matrix of the current parameter values and μ is the 1D matrix of the mean values of the Gaussian priors. The matrix contains the flux parameters described by the T2K flux matrix and is highly correlated bin to bin, the cross section parameters which are uncorrelated and the detector parameters. Each sub-matrix is uncorrelated pre-fit. In the second term, the summation is over each sample which is being fitted (i = P0D sample, SMRD sample). The expected number of events in each sample is denoted by x_i and n_i is the number of observed events.

The signal sample and the SMRD control sample are not disjoint, meaning that they have a number of events in common; the samples share about 100 events. The fit sorts each event into one of the three samples. It is first ascertained whether or not events are part of the signal sample before they are categorised into one of the other samples. Once an event has been sorted into a sample, it cannot be categorised into another sample.

Both the pre-fit and post-fit parameters along with their associated uncertainties can be found in tables B.1 and B.2 respectively in appendix B. A description of each parameter can also be found in table B.3. Examining the table shows sensible parameter values after the fit is completed along with reasonable uncertainties.

5.7 Results

Table 5.14 shows the total number of events for all samples, for data, MC and the MC after the fit has been applied. The MC over predicted the data in the P0D sample pre-fit and under predicted the data in the SMRD sample. Before fitting, the SMRD sample had a data-MC agreement of approximately 90%, post-fit this agreement is $\sim 97\%$. The P0D sample has 5% more MC than data pre-fit equating to 39 events. Fitting this sample reduces the difference in number of events between data and MC to 24; post-fit the P0D sample MC over predicts the data by approximately 3%. The fitting procedure has resulted in the agreement between data and MC to improve in both samples.

Sample	Data	MC	MC Post Fit
Signal	717 ± 26	856 ± 199	942 ± 168
P0D	772 ± 27	811 ± 211	794 ± 56
SMRD	553 ± 23	496 ± 137	538 ± 45

Table 5.14: Total number of events for each sample in the analysis in data as well as MC before and after fitting. These numbers include signal as well as background.

The number of events in the table contain signal as well as background. In order to calculate the NCE cross section using equation 5.1, the number of background events must be extracted from the total number of events. Before the fitting procedure the number of background events in the signal sample is 475 ± 110. Post-fit the number of background events in the signal sample is 526 ± 65.

The number of events post-fit in the signal sample has increased by more than what was expected. The number of events in the control samples have increased by approximately 50 events post-fit. The number of events in the signal sample would be expected to increase by fewer events than this, however from table 5.14 it can be seen that the signal sample has increased by nearly 100 events. This increase can be explained by changes in the post-fit parameters. For example, the parameter $GXSec\_M_ANCEL$ has changed by approximately 30% post-fit (this can be seen by comparing tables B.1 and B.2 in appendix B). This parameter is the axial mass parameter for neutral current elastic interactions and it changes the normalisation and Q^2 shape of the cross section. A larger value of this parameter means that more NCE events are likely to happen. The control samples will also be affected by this parameter increasing as OOFV neutron background event may be caused by an external NCE event.

The final result for the NCE neutrino-nucleon cross section is

$$(2.72 \pm 0.41) \times 10^{-40}\text{cm}^2 \text{ nucleon}^{-1} \tag{5.16}$$

The total error on the measurement is approximately 15%; the uncertainties are broken down in table 5.15. The largest uncertainty on the cross section measurement is the uncertainty on the background.

	Percentage Uncertainty [%]
Statistical	3.63
Flux	8.16
Efficiency	7.00
Background	10.04
Total	15.15

Table 5.15: The errors which contribute to the NCE cross section measurement broken down by each uncertainty.

The GENIE 2.8.0 prediction is $(4.83 \pm 2.38) \times 10^{-40}\text{cm}^2$ nucleon^{-1}. The measured cross section is ∼30% below the GENIE prediction. However, this measured cross section falls within the uncertainty provided by the GENIE 2.8.0 prediction. There are large theoretical uncertainties on the predictions of neutral current elastic cross section on nuclear targets. These uncertainties include large uncertainties on the elastic axial mass parameter and Δs as well as uncertainties on final state interactions. In addition, there are processes that are not accurately modelled (such as the use of the relativistic Fermi gas nuclear model, known to be insufficient to describe electron and charged current scattering measurements) and also some processes that are not modelled at all (such as 2p-2h interactions).

5.7.1 Future Developments

Due to time constraints, a differential cross section measurement as a function of Q^2 was not performed for this thesis as further development of the analysis is still needed. The analysis will be developed to the point where a differential cross section measurement will be possible.

A differential cross section measurement will allow for a further study in which a comparison between the CCQE and the NCE differential cross sections. This will provide a cross-check for modelling neutrino interactions; a model that describes CCQE data should

also describe NCE data. In addition to this, different processes produce different final states in NCE and CCQE, giving rise to the potential to break degeneracy between models.

The differential measurement may also allow for a measurement of the strange contribution to the proton spin to be determined using ND280. As described in chapter 3, a ratio of the CCQE and NCE cross sections is sensitive to Δs, which denotes the strange contribution to the proton spin in the form factors.

There are areas in which this analysis can be improved if the future developments discussed above are to be realised. For example, the OOFV neutron background posed one of the largest challenges to this analysis. Further studies into this background could lead to improved purity in the signal sample and better efficiency in selecting NC0π events. Greater understanding of these OOFV neutrons would help reduce the uncertainty on the background. One way in which a better knowledge of this background can be obtained is by reducing the systematic on the SMRD sample. The total detector systematic for the SMRD control sample is larger than either of the other samples in the analysis; this is due to the SMRD efficiency being 10%. Reducing this systematic would improve the SMRD sample's ability to constrain the OOFV neutron background.

Neutral current elastic interactions with two protons in the final state are primarily the result of final state interactions. Studying this interaction would provide a complimentary measurement to T2K's charged current analysis with two protons in the final state. It is expected that the event rates for this type of interaction will be lower than those for one proton in the final state. Studying multi-proton final states may allow for various nuclear effects to be disentangled, however it is unclear at this stage whether or not this would be possible.

Chapter 6

Conclusion

The subject of this thesis was making a measurement of the NCE cross section using the T2K off-axis near detector, ND280. At the time of writing this thesis, few measurements of this interaction process are available. The focus was on providing a single binned total cross section for the NCE process. Though further development of this analysis is still needed, it has been able to give the first indications of a NCE cross section as measured by T2K. It is hoped that, after further development of this analysis, a differential cross section can be presented and a comparison between the CCQE and NCE cross sections can be made using the T2K data sets. Using the FGD as target for neutrino interactions, the analysis was able to determine a NCE cross section of $(2.72 \pm 0.41) \times 10^{-40}\text{cm}^2$ nucleon^{-1}.

Additionally, this thesis provided a study on the degradation of the plastic scintillator bars used in ND280's electromagnetic calorimeters. The analysis has lead to a better understanding of the detector which will allow for better measurements in future. Quantifying the ageing of the plastic scintillators allows for predictions to be made on how the detector will perform in the future. This information can help determine if the sub-detector will be operating at an acceptable level during Hyper-Kamiokande's data taking life time. It also has made it possible for a calibration to be implemented in the software to correct for the effect.

Appendix A

Independent ECal Ageing Study

In addition to the study on the degradation of the ECals discussed in the main study, an addition independent analysis of the ageing of the ECal was carried out in parallel to it. This study first compressed data from oaAnalysis files, official files generated by the ND280 software group, into ntuples to analyse to allow for a faster running time.

A.1 Control Samples

For this study, like the study detailed in the main text, cosmic muons were exploited to study the degradation of the ECals. Cosmic muons were selected from the data using the Trip-t cosmic trigger with a cut of 300 MeV placed on the TPC momentum to ensure that the cosmics acted as MIPs.

A.2 Analysis Method

This study looks at both the DS and the barrel ECals. The barrel module is divided up into six sub-modules and are studied independently of each other. The six barrel modules are top left, left, bottom left, top right, right and bottom right.

This study only looked included data from run 2 to 4; this time period was divided up into a number of time bins. A histogram of the total charge deposited per track length is plotted for each time bin for both Monte Carlo and data. Both the Monte Carlo and data are fitted with a Gaussian convoluted with a Landau fit as shown in figure A.1. The MPV and the error on the MPV is taken from these fits and plotted in the corresponding

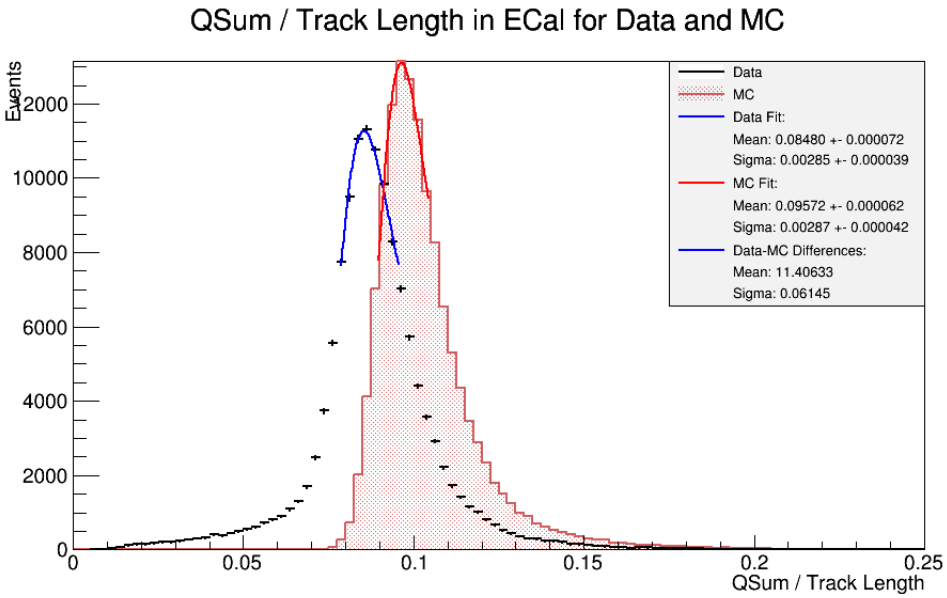

Figure A.1: Total charge deposited per track length plotted for the bottom right barrel module including cosmic muon data from runs 2-4.

time bin. Once this is done for all time bins the plot is scaled so that the first bin for both the Monte Carlo and data are equal to one. Note that the first bin must therefore not be empty.

The light output of a plastic scintillator as a function of time should follow an exponential decay due to the ageing of the plastic. An exponential of the form shown in equation A.1 is fitted to the data points on the time plot, where A is a scaling factor, t_0 is the time offset, τ is the decay constant and C is the y-offset, the minimum the scintillator will decay to.

$$y = A \exp\left(\left(t - t_0\right)/\tau\right) + C \tag{A.1}$$

This fit function was taken from the long term performance of the MINOS calibration procedure and stability of the MINOS detectors paper [97]. This method sets the initial time of the bins to zero and studies the decay from that point so that in equation A.1 t_0 is equal to zero. The last parameter, the y-offset, is the parameter of most interest as this shows how the scintillator bars will perform in the future.

A.3 Results

By examining the function of time plots below, figures A.2 and A.3, it is clear to see that the data points decrease with time showing that the plastic scintillator bars in the ECals are degrading and therefore are emitting less light. The fit shows how the trend follows an exponential decay.

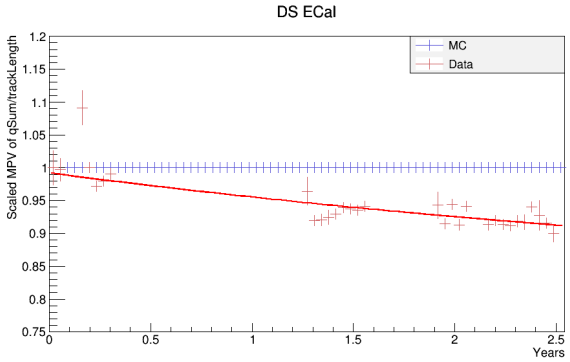

Figure A.2: Scintillator ageing result for the DS ECal.

Figure A.2 shows response degradation of the DS ECal using both the sand muon sample and the cosmic muon sample to produce the plots. Both plots clearly show a decreasing response for the data points compared to the MC points, which remain constant.

Figure A.3 contains all six of the barrel ECal plots. These plots show the same decreasing trend as was seen in the DS ECal. All the plots are fitted with the the exponential fit as described in equation A.1 and the parameters of interest, the decay constant and the y-offset, are taken from this fit. It should be noted that in the bottom left barrel ECal module, for run 3, the data appears to have increased relative to the previous run, this is currently unexplained. Also the data for the top right barrel ECal module is also less well described by the exponential fit than the other modules and includes a data point with a very large error, the reason behind this is also unknown. The implications of this is that the results for the bottom left and top right barrel ECal modules must only be taken as a rough estimate of the ageing effect in these modules.

Table A.1 summaries the results of the second method used to study the ageing of the ECal scintillator bars. As can be seen from this table, the response of the ECal is expected to decrease by 20-30% over time which is in agreement found from the first

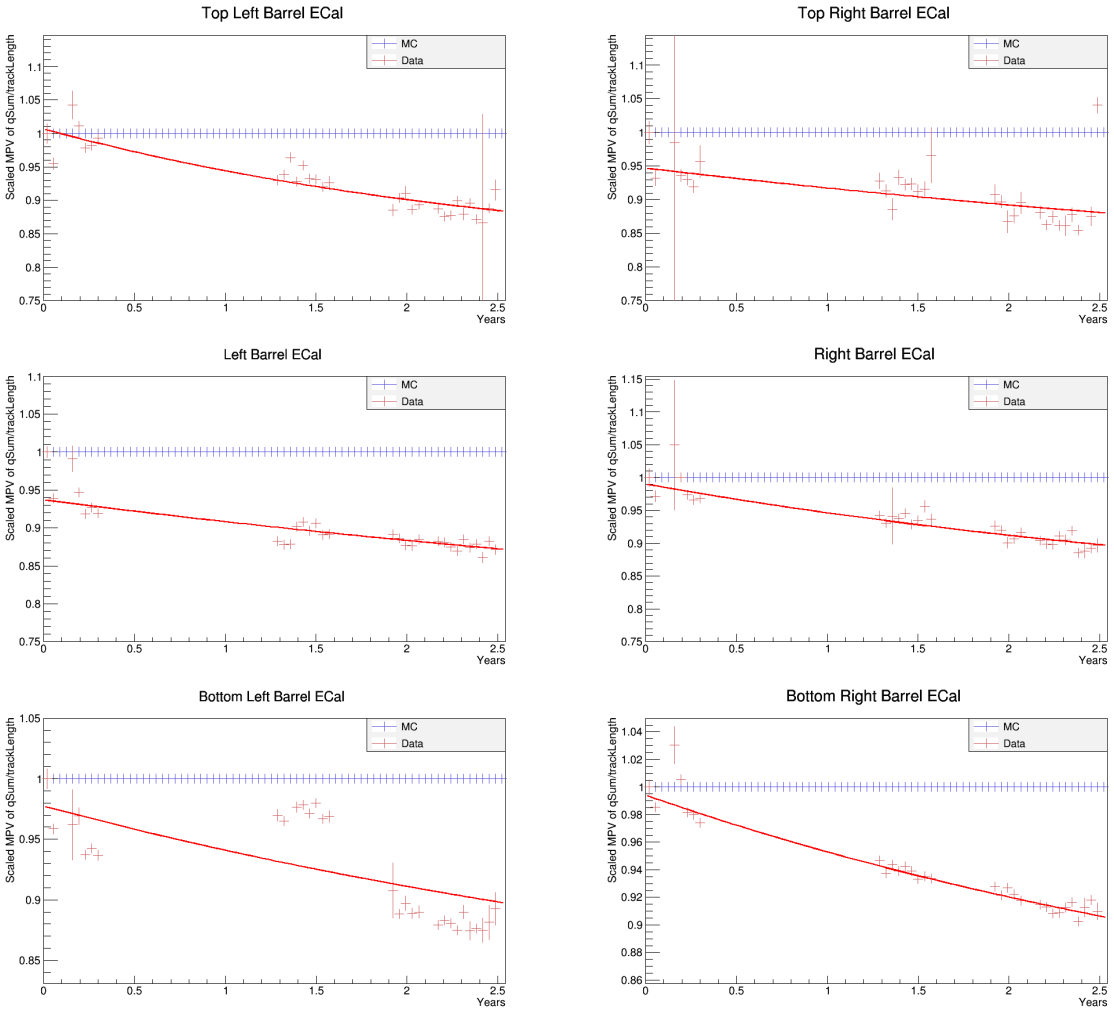

Figure A.3: Scintillator ageing plots for the barrel ECal.

ND280 Plastic Scintillator Ageing Study		
ECal Module	Y-Offset (% of Original Response)	Decay Constant (Years)
DS (Cosmic Muon Sample)	79.10 ± 0.40	4.96 ± 0.42
Top Left	80.38 ± 0.34	2.65 ± 0.14
Left	73.63 ± 0.14	6.44 ± 0.23
Bottom Left	77.65 ± 0.18	4.99 ± 0.19
Top Right	75.64 ± 0.52	5.26 ± 0.59
Right	78.90 ± 0.29	4.07 ± 0.22
Bottom Right	79.32 ± 0.12	4.36 ± 0.10

Table A.1: A summary of the y-offset and decay constant taken from the exponential fits for all ECal modules.

study.

Appendix B

Fit Parameters

B.1 Pre-Fit Parameters Table

Parameter Name	Value	Parameter Error
OOFVNeutronScale_Iron/Brass	1	1
OOFVNeutronScale_Carbon/Oxygen	1	1
OOFVNeutronScale_Lead	1	1
OOFVNeutronScale_Aluminium	1	1
GHadrAGKY_pT1pi	0	1
GHadrAGKY_xF1pi	0	1
GINuke_FrAbs_N	0	1
GINuke_FrAbs_pi	0	1
GINuke_FrCEx_N	0	1
GINuke_FrCEx_pi	0	1
GINuke_FrInel_N	0	1
GINuke_FrInel_pi	0	1
GINuke_FrPiProd_N	0	1
GINuke_FrPiProd_pi	0	1
GINuke_MFP_N	0	1
GINuke_MFP_pi	0	1
GRDcy_BR1eta	0	1
GRDcy_BR1gamma	0	1
GRDcy_Theta_Delta2Npi	0	1
GSystNucl_CCQEMomDistroFGtoSF	0	1
GSystNucl_CCQEPauliSupViaKF	0	1
GXSec_AhtBY	0	1
GXSec_AhtBYshape	0	1
GXSec_BhtBY	0	1
GXSec_BhtBYshape	0	1
GXSec_CV1uBY	0	1
GXSec_CV1uBYshape	0	1
GXSec_CV2uBY	0	1
GXSec_CV2uBYshape	0	1
GXSec_DISNuclMod	0	1
GXSec_EtaNCEL	0	1
GXSec_MaCCQE	0	1
GXSec_MaCCRES	0	1
GXSec_MaCCRESshape	0	1
GXSec_MaCOHpi	0	1
GXSec_MaNCEL	0	1
GXSec_MaNCRES	0	1

Parameter Name	Value	Parameter Error
GXSec_MaNCRESshape	0	1
GXSec_MvCCRES	0	1
GXSec_MvCCRESshape	0	1
GXSec_MvNCRES	0	1
GXSec_MvNCRESshape	0	1
GXSec_NormCCRES	0	1
GXSec_NormDISCC	0	1
GXSec_NormNCRES	0	1
GXSec_R0COHpi	0	1
GXSec_RnubarnuCC	0	1
GXSec_RvbarnCC1pi	0	1
GXSec_RvbarnCC2pi	0	1
GXSec_RvbarnNC1pi	0	1
GXSec_RvbarnNC2pi	0	1
GXSec_RvbarpCC1pi	0	1
GXSec_RvbarpCC2pi	0	1
GXSec_RvbarpNC1pi	0	1
GXSec_RvbarpNC2pi	0	1
GXSec_RvnCC1pi	0	1
GXSec_RvnCC2pi	0	1
GXSec_RvnNC1pi	0	1
GXSec_RvnNC2pi	0	1
GXSec_RvpCC1pi	0	1
GXSec_RvpCC2pi	0	1
GXSec_RvpNC1pi	0	1
GXSec_RvpNC2pi	0	1
GXSec_VecFFCCQEshape	0	1
xsec_neutronsi	1	0.1
det_sample000_signalnorm	1	0.045
det_sample001_p0dnorm	1	0.045
det_sample002_smrdnorm	1	0.11
f_numu_0	1	0.097
f_numu_1	1	0.1
f_numu_2	1	0.094
f_numu_3	1	0.088
f_numu_4	1	0.11
f_numu_5	1	0.11
f_numu_6	1	0.074
f_numu_7	1	0.069
f_numu_8	1	0.083
f_numu_9	1	0.098
f_numu_10	1	0.11
f_numubar_0	1	0.1
f_numubar_1	1	0.081
f_numubar_2	1	0.078
f_numubar_3	1	0.083
f_numubar_4	1	0.087
f_nue_0	1	0.09
f_nue_1	1	0.092
f_nue_2	1	0.09
f_nue_3	1	0.088
f_nue_4	1	0.088
f_nue_5	1	0.083
f_nue_6	1	0.096
f_nuebar_0	1	0.074
f_nuebar_1	1	0.14

Table B.1: Table of the values and their errors for each parameter used in the fit before the fitting procedure has been carried out.

B.2 Post-Fit Parameters Table

Name	Value	Parameter Error
OOFVNeutronScale_Iron/Brass	1.098	0.6602
OOFVNeutronScale_Carbon/Oxygen	0.9275	0.3859
OOFVNeutronScale_Lead	1.017	0.9479
OOFVNeutronScale_Aluminium	1.026	0.954
GHadrAGKY_pT1pi	0.006893	0.9992
GHadrAGKY_xF1pi	-0.008105	0.9935
GINuke_FrAbs_N	-0.008665	0.9956
GINuke_FrAbs_pi	0.9697	0.9991
GINuke_FrCEx_N	-0.002562	0.9998
GINuke_FrCEx_pi	-0.0005318	0.9383
GINuke_FrInel_N	0.9862	0.9991
GINuke_FrInel_pi	0.9917	0.9983
GINuke_FrPiProd_N	0.0006189	0.9996
GINuke_FrPiProd_pi	-0.002378	0.9999
GINuke_MFP_N	9.039E-07	0.6209
GINuke_MFP_pi	-0.1865	0.9996
GRDcy_BR1eta	0.0006792	0.9999
GRDcy_BR1gamma	-0.0001933	1
GRDcy_Theta_Delta2Npi	0.00121	0.9999
GSystNucl_CCQEMomDistroFGtoSF	-5.719E-06	1
GSystNucl_CCQEPauliSupViaKF	-0.0001375	0.818
GXSec_AhtBY	-0.182	0.9994
GXSec_AhtBYshape	-5.719E-06	1
GXSec_BhtBY	0.1181	0.9989
GXSec_BhtBYshape	-5.719E-06	1
GXSec_CV1uBY	0.1374	0.9996
GXSec_CV1uBYshape	-5.719E-06	1
GXSec_CV2uBY	-0.1655	0.9996
GXSec_CV2uBYshape	-5.719E-06	1
GXSec_DISNuclMod	-5.719E-06	1
GXSec_EtaNCEL	0.0007047	1.004
GXSec_MaCCQE	0.8014	0.9696
GXSec_MaCCRES	-5.719E-06	1
GXSec_MaCCRESshape	0.00232	0.9996
GXSec_MaCOHpi	0.0001666	0.3367
GXSec_MaNCEL	0.2829	0.997
GXSec_MaNCRES	-5.719E-06	1
GXSec_MaNCRESshape	-0.0008629	1.011
GXSec_MvCCRES	-5.719E-06	1
GXSec_MvCCRESshape	0.0007761	1.02
GXSec_MvNCRES	-5.719E-06	1
GXSec_MvNCRESshape	7.56E-05	1.004
GXSec_NormCCRES	0.009801	0.9925
GXSec_NormDISCC	-5.719E-06	1
GXSec_NormNCRES	-0.001852	0.9981
GXSec_R0COHpi	-0.0005272	0.7551
GXSec_RnubarnuCC	-5.719E-06	1
GXSec_RvbarnCC1pi	-3.127E-05	1
GXSec_RvbarnCC2pi	0.0001806	1
GXSec_RvbarnNC1pi	-6.333E-05	1
GXSec_RvbarnNC2pi	-9.202E-05	1
GXSec_RvbarpCC1pi	0.0005799	1
GXSec_RvbarpCC2pi	0.0002704	1
GXSec_RvbarpNC1pi	4.424E-05	1
GXSec_RvbarpNC2pi	-5.904E-05	1
GXSec_RvnCC1pi	0.01011	0.9881
GXSec_RvnCC2pi	0.002597	0.9993
GXSec_RvnNC1pi	0.0008581	0.9992
GXSec_RvnNC2pi	-0.0002821	1
GXSec_RvpCC1pi	0.0005254	0.9999

Name	Value	Parameter Error
GXSec_RvpCC2pi	0.0005671	0.9997
GXSec_RvpNC1pi	-0.0005301	0.9999
GXSec_RvpNC2pi	-0.0006271	0.9998
GXSec_VecFFCCQEshape	-0.001895	0.9998
xsec_neutronsi	1	0.09972
det_sample000_signalnorm	1	0.04518
det_sample001_p0dnorm	0.9999	0.04447
det_sample002_smrdnorm	1.005	0.09805
f_numu_0	1.001	0.09575
f_numu_1	1.001	0.09931
f_numu_2	1.001	0.09195
f_numu_3	1.001	0.08531
f_numu_4	1.002	0.1048
f_numu_5	1.001	0.103
f_numu_6	1.001	0.0721
f_numu_7	1.001	0.0672
f_numu_8	1.001	0.08055
f_numu_9	1.001	0.09551
f_numu_10	1.001	0.1123
f_numubar_0	1.001	0.1007
f_numubar_1	1.001	0.08015
f_numubar_2	1.001	0.07702
f_numubar_3	1.001	0.08222
f_numubar_4	1.001	0.086
f_nue_0	1.001	0.08853
f_nue_1	1.001	0.09038
f_nue_2	1.001	0.08823
f_nue_3	1.001	0.08572
f_nue_4	1.001	0.08589
f_nue_5	1.001	0.08049
f_nue_6	1.001	0.09405
f_nuebar_0	1.001	0.07276
f_nuebar_1	1.001	0.1396

Table B.2: Table of the values and their errors for each parameter used in the fit after the fitting procedure has been carried out.

B.3 Description of the Fit Parameters

Parameter Name	Description
OOFVNeutronScale_Iron/Brass	Ad hoc parameter that scale OOFV neutron production on iron and brass
OOFVNeutronScale_Carbon/Oxygen	Ad hoc parameter that scale OOFV neutron production on carbon and oxygen
OOFVNeutronScale_Lead	Ad hoc parameter that scale OOFV neutron production on lead
OOFVNeutronScale_Aluminium	Ad hoc parameter that scale OOFV neutron production on aluminium
GHadrAGKY_pT1pi	Pion transverse momentum PDF for Nπ states in AGKY (hadronisation model)
GHadrAGKY_xF1pi	Pion Feynman-x PDF for Nπ states in AGKY (hadronisation model)
GINuke_FrAbs_N	Nucleon absorption probability
GINuke_FrAbs_pi	Pion absorption probability
GINuke_FrCEx_N	Nucleon charge exchange probability
GINuke_FrCEx_pi	Pion charge exchange probability
GINuke_FrInel_N	Nucleon inelastic reaction probability
GINuke_FrInel_pi	Pion inelastic reaction probability
GINuke_FrPiProd_N	Nucleon probability
GINuke_FrPiProd_pi	Pion probability
GINuke_MFP_N	Nucleon mean free path (total rescattering probability)
GINuke_MFP_pi	Pion mean free path (total rescattering probability)
GRDcy_BR1eta	Branching ratio for single-η resonance decays
GRDcy_BR1gamma	Branching ratio for radiative resonance decays
GRDcy_Theta_Delta2Npi	Choice of pion angular distribution in $\Delta \rightarrow \pi N$ (isotropic / Rein-Sehgal)
GSystNucl_CCQEMomDistroFGtoSF	CCQE momentum distribution
GSystNucl_CCQEPauliSupViaKF	CCQE Pauli suppression
GXSec_AhtBY	A_{HT} parameter in Bodek-Yang (DIS) model scaling variable ξ_W
GXSec_AhtBYshape	Shape of A_{HT} parameter in Bodek-Yang (DIS) model scaling variable ξ_W
GXSec_BhtBY	B_{HT} parameter in Bodek-Yang (DIS) model scaling variable ξ_W
GXSec_BhtBYshape	Shape of B_{HT} parameter in Bodek-Yang (DIS) model scaling variable ξ_W
GXSec_CV1uBY	C_{V1u} u-quark valence GRV98 PDF correction parameter in Bodek-Yang (DIS) model
GXSec_CV1uBYshape	Shape of C_{V1u} u-quark valence GRV98 PDF correction parameter in Bodek-Yang (DIS) model
GXSec_CV2uBY	C_{V2u} u-quark valence GRV98 PDF correction parameter in Bodek-Yang (DIS) model
GXSec_CV2uBYshape	Shape of C_{V2u} u-quark valence GRV98 PDF correction parameter in Bodek-Yang (DIS) model
GXSec_DISNuclMod	DIS nuclear modle
GXSec_EtaNCEL	η NC elastic
GXSec_MaCCQE	The axial mass parameter for CCQE interactions
GXSec_MaCCRES	The axial mass parameter for CC resonant interactions
GXSec_MaCCRESshape	The shape of the axial mass parameter for CC resonant interactions
GXSec_MaCOHpi	The axial mass parameter for
GXSec_MaNCEL	The axial mass parameter for NCE interactions
GXSec_MaNCRES	The axial mass parameter for NC resonant interactions
GXSec_MaNCRESshape	The shape of the axial mass parameter for NC resonant interactions
GXSec_MvCCRES	Parameter in CC resonance vector form-factor
GXSec_MvCCRESshape	Shape parameter in CC resonance vector form-factor
GXSec_MvNCRES	Parameter in NC resonance vector form-factor
GXSec_MvNCRESshape	Shape parameter in NC resonance vector form-factor
GXSec_NormCCRES	CC resonance normalisation
GXSec_NormDISCC	CC DIS normalisation
GXSec_NormNCRES	NC resonance normalisation
GXSec_R0COHpi	Ratio of coherent pion production
GXSec_RnubarnuCC	Ratio of $\bar{\nu}$ to ν CC interactions
GXSec_RvbarnCC1pi	Non-resonance $\bar{\nu}$ CC1π
GXSec_RvbarnCC2pi	Non-resonance $\bar{\nu}$ CC2π
GXSec_RvbarnNC1pi	Non-resonance $\bar{\nu}$ NC1π
GXSec_RvbarnNC2pi	Non-resonance $\bar{\nu}$ NC2π
GXSec_RvbarpCC1pi	Non-resonance $\bar{\nu}$ CC1π
GXSec_RvbarpCC2pi	Non-resonance $\bar{\nu}$ CC2π
GXSec_RvbarpNC1pi	Non-resonance $\bar{\nu}$ NC1π
GXSec_RvbarpNC2pi	Non-resonance $\bar{\nu}$ NC2π
GXSec_RvnCC1pi	Non-resonance ν CC1π
GXSec_RvnCC2pi	Non-resonance ν CC2π
GXSec_RvnNC1pi	Non-resonance ν NC1π
GXSec_RvnNC2pi	Non-resonance ν NC2π
GXSec_RvpCC1pi	Non-resonance ν CC1π

Parameter Name	Description
GXSec_RvpCC2pi	Non-resonance ν CC1π
GXSec_RvpNC1pi	Non-resonance ν NC1π
GXSec_RvpNC2pi	Non-resonance ν NC2π
GXSec_VecFFCCQEshape	Choice of CCQE vector form-factors (BBA05 / dipole)
xsec_neutronsi	Neutron SI parameter
det_sample000_signalnorm	The detector systematics for the signal sample
det_sample001_p0dnorm	The detector systematics for the P0D sample
det_sample002_smrdnorm	The detector systematics for the SMRD sample
f_numu_0	Flux parameters
f_numu_1	Flux parameters
f_numu_2	Flux parameters
f_numu_3	Flux parameters
f_numu_4	Flux parameters
f_numu_5	Flux parameters
f_numu_6	Flux parameters
f_numu_7	Flux parameters
f_numu_8	Flux parameters
f_numu_9	Flux parameters
f_numu_10	Flux parameters
f_numubar_0	Flux parameters
f_numubar_1	Flux parameters
f_numubar_2	Flux parameters
f_numubar_3	Flux parameters
f_numubar_4	Flux parameters
f_nue_0	Flux parameters
f_nue_1	Flux parameters
f_nue_2	Flux parameters
f_nue_3	Flux parameters
f_nue_4	Flux parameters
f_nue_5	Flux parameters
f_nue_6	Flux parameters
f_nuebar_0	Flux parameters
f_nuebar_1	Flux parameters

Table B.3: A description of each parameter used in the fitting procedure.

Bibliography

[1] https://en.wikipedia.org/wiki/Standard_Model

[2] I. Aitchison A. Hey. Gauge Theories in Particle Physics, A Practical Introduction, Volume 2, Non-Abelian Gauge Theories, QCD and the Electroweak Theory, Fourth Edition, p. 238. 2013

[3] L. M. Brown. The idea of the neutrino. Physics today, 31(9):23, 1978.

[4] C. L. Cowan, Jr., F. Reines, F. B. Harrison, H. W. Kruse, and A. D. McGuire. Detection of the Free Neutrino: A Confirmation. Science, 124:103104, July 1956. doi: 10.1126/science.124.3212.103.

[5] Tomasz Golan. Modeling nuclear effects in NuWro Monte Carlo neutrino event generator. http://neutrino.ift.uni.wroc.pl/files/phd_tomasz_golan.pdf, 2014.

[6] G. Danby, J-M. Gaillard, K. Goulianos, L. M. Lederman, N. Mistry, M. Schwartz, and J. Steinberger. Observation of high-energy neutrino reactions and the existence of two kinds of neutrinos. Phys. Rev. Lett., 9:3644, Jul 1962. doi: 10.1103/PhysRevLett.9.36.

[7] K. Kodama et al. Observation of tau neutrino interactions. Phys. Lett. B., 504(3):218 224, 2001. ISSN 0370-2693. doi: http://dx.doi.org/10.1016/S0370-2693(01)00307-0.

[8] The ALEPH Collaboration, The DELPHI Collaboration, The L3 Collaboration, The OPAL Collaboration and The SLD Collaboration, Precision electroweak measurements on the Z resonance, Physics Reports, vol. 427, no. 5-6, pp. 257454, 2006.

[9] N. Vinyoles, et al. A New Generation of Standard Solar Models. arXiv:1611.09867v4 [astro-ph.SR], 2017.

[10] R. Davis, D. S. Harmer, and K. C. Hoffman, Phys. Rev. Lett. 20, 1205 (1968).

[11] J. N. Abdurashitov et al. (SAGE), Phys. Rev. C60, 055801 (1999), arXiv:astro-ph/9907113 [astro-ph].

[12] W. Hampel et al. (GALLEX), Phys. Lett. B447, 127 (1999).

[13] B. Pontecorvo. Neutrino experiments and the problem of conservaton of leptonic charge. Sov. Phys. JETP, 26, 1968.

[14] Q. Ahmad et al. (SNO Collaboration), Phys.Rev.Lett. 89, 011301 (2002), arXiv:nucl-ex/0204008 [nucl-ex].

[15] Q. Ahmad et al. (SNO Collaboration), Phys.Rev.Lett. 87, 071301 (2001), arXiv:nucl-ex/0106015 [nucl-ex].

[16] https://www.nobelprize.org/nobel_prizes/physics/laureates/2015/

[17] Z. Maik, M. Nakagawa, and S. Sakata, Remarks on the unified model of elementary particles, Progress of Theoretical Physics, vol. 28, pp. 870880, Nov 1962.

[18] L. Wolfenstein. Neutrino oscillations in matter. Phys. Rev. D 17, 23692374, May 1978. doi: 10.1103/PhysRevD.17.2369.

[19] S. F. King and C. Luhn, Neutrino mass and mixing with discrete symmetry, Reports on Progress in Physics, vol. 76, no. 5, p. 056201, 2013.

[20] Julien Lesgourgues and Sergio Pastor. Neutrino cosmology and Planck. New J. Phys., 16:065002, 2014.

[21] B. Bornschein. Determination of neutrino mass from tritium beta decay. Fusion Science and Technology, 54(1):5966, 2008.

[22] J. D. Vergados, H. Ejiri, and F. Simkovic. Neutrinoless double beta decay and neutrino mass. Int. J. Mod. Phys., E25(11):1630007, 2016

[23] Francesco Capozzi, Eleonora Di Valentino, Eligio Lisi, Antonio Marrone, Alessandro Melchiorri, and Antonio Palazzo. Global constraints on absolute neutrino masses and their ordering. Phys. Rev., D95(9):096014, 2017

[24] A. D. Sakharov, Pisma Zh. Eksp. Teor. Fiz. 5, 32 (1967), [Usp. Fiz.Nauk161,61(1991)].

[25] W. Marciano, Z. Parsa, Intense Neutrino Beams and Leptonic CP Violation. arXiv:hep-ph/0610258v1, 2006.

[26] M. G. Aartsen, et al., Measurement of Atmospheric Neutrino Oscillations at 6-56 GeV with IceCube DeepCore. arXiv:1707.07081v1 [hep-ex], 2017.

[27] M. Apollonio, et al., Limits on Neutrino Oscillations from the CHOOZ Experiment. arXiv:hep-ex/9907037v1, 1999.

[28] J.I Crespo-Anadón, Double Chooz: Latest Results. arXiv:1412.3698v1 [hep-ex], 2014.

[29] A. Gando, et al. (KamLAND), Phys. Rev. D83, 052002 (2011), arXiv:1009.4771 [hep-ex].

[30] F. P. An, et al., Measurement of Electron Antineutrino Oscillation Based on 1230 Days of Operation of the Daya Bay Experiment. arXiv:1610.04802v1 [hep-ex], 2016.

[31] S.-H. Seo (RENO), Proceedings, 26th International Conference on Neutrino Physics and Astrophysics (Neutrino 2014), AIP Conf. Proc. 1666, 080002 (2015), arXiv:1410.7987 [hep-ex].

[32] M. Ahn, et al. (K2K Collaboration), Phys.Rev. D74, 072003 (2006), arXiv:hep-ex/0606032 [hep-ex].

[33] Simon De Rijck, for the MINOS and MINOS+ Collaborations, Latest Results from MINOS and MINOS+. J. Phys.: Conf. Ser. 873 012032, 2017.

[34] K. Abe, et al. Updated T2K Meausrements of Muon Neutrino and Antineutrino Disappearance Using 1.5×10^{21} Protons on Target. arXiv:1704.06409v2 [hep-ex], 2017.

[35] P. Adamson, et al. Measurement of the Neutrino Mixing Angel θ_{23} in NOνA. arXiv:1701.05891v2 [hep-ex], 2017.

[36] A. Aguilar-Arevalo et al. (LSND Collaboration), Phys.Rev. D64, 112007 (2001), arXiv:hep-ex/0104049 [hep-ex].

[37] A. Aguilar-Arevalo et al. (MiniBooNE Collaboration), Phys.Rev.Lett. 110, 161801 (2013), arXiv:1303.2588 [hep-ex].

[38] K. Abe, et al. Letter of intent: The hyper-kamiokande experiment detector design and physics potential. arXiv:1109.3262, 2011.

[39] K. Abe, et al. Proposal for an Extended Run of T2K to 20×10^{21} POT. arXiv:1609.0411v1, 2016.

[40] C. Adams, et al. The long-baseline neutrino experiment: Exploring fundamental symmetries of the universe. arXiv:1307.7335v3, 2014.

[41] P. F. de Salas, et al. Status of Neutrino Oscillations 2017. arXiv:1708.01186v1 [hep-ph], 2017.

[42] Bethe, H., and Peierls, R., 1934, Nature 133, 532.

[43] S.L. Glashow, Nucl. Phys. 22:579588 (1961).

[44] S. Weinberg, Phys. Rev. Lett. 19:12641266 (1967).

[45] A. Salam Originally printed in *Svartholm: Elementary Particle Theory, Proceedings Of The Nobel Symposium Held 1968 At Lerum, Sweden*, Stockholm 1968, 367-377.

[46] D. Griffiths. Introduction to Elementary Particles (2nd edition). Wiley-VCH, 2008.

[47] F. Halzen and A. Martin, Quarks & Leptons, John Wiley & Sons (1984)

[48] Particle Data Group. Review of Particle Physics. Phys. Rev. D 86, 010001, doi:10.1103/PhysRevD.86.010001, 2012.

[49] C.S. Wu, E. Ambler, R.W. Hayward, D.D. Hoppes, and R.P. Hudson. Experimental test of parity conservation in beta decay. Phys. Rev., 105:14131415, Feb 1957. doi: 10.1103/PhysRev.105.1413

[50] J.A. Formaggio and G.P. Zeller. From eV to EeV: Neutrino cross sections across energy scales. Rev. Mod. Phys., 84:13071341, Sep 2012. doi: 10.1103/RevModPhys.84.1307

[51] J. A. Formaggio and G. P. Zeller. From eV to EeV: Neutrino cross sections across energy scales. Rev. Mod. Phys., 84:13071341, Sep 2012. doi: 10.1103 RevModPhys.84.1307.

[52] C. H. Llewellyn-Smith, Phys. Rep. 3C:261 (1972).

[53] F. Halzen and A. Martin, Quarks & Leptons, John Wiley & Sons (1984).

[54] O. Gayou et al. (Jefferson Lab Hall A Collaboration), Measurement of G_{E_p}/G_{M_p} in ep $\rightarrow$ ep to $Q^2 = 5.6 GeV^2$, Phys. Rev. Lett. 88, 092301(2002), doi:10.1103/PhysRevLett.88.092301

[55] V. Bernard, L. Elouadrhiri, and U-G. Meiner. Axial structure of the nucleon. Journal of Physics G: Nuclear and Particle Physics, 28(1):R1, 2002.

[56] A. A. Aguilar-Areval, et al. (MiniBooNE Collaboration), First Measurement of the Muon Neutrino Charged Current Quasielastic Double Differential Cross Section, Phys.Rev. D81, 092005 (2010), doi:10.1103/PhysRevD.81.092005

[57] M. Martini, M. Ericson, G. Chanfray, and J. Marteau, A unified approach for nucleon knock-out, coherent and incoherent pion production in neutrino interactions with nuclei, Phys. Rev. C80 065501 (2009), doi:10.1103/PhysRevC.80.065501

[58] J. Nieves, I. R. Simo, and M. J. V. Vacas, Inclusive charged-current neutrino-nucleus reactions, Phys. Rev. C 83 045501 (2011), doi:10.1103/PhysRevC.83.045501

[59] A. Bodek, H. S. Budd, and E. Christy, Neutrino quasi-elastic scattering on nuclear targets, Eur. Phys. J. C 71 (2011) 1726, oi:10.1140/epjc/s10052-011-1726-y

[60] J. Nieves, I. R. Simo, and M. V. Vacas, The nucleon axial mass and the MiniBooNE quasielastic neutrinonucleus scattering problem, Phys. Lett. B 707, 72 (2012), doi:10.1016/j.physletb.2011.11.061

[61] K. Abe, et al. (T2K Collaboration), Measurement of the ν_μ CCQE cross section on carbon with the ND280 detector at T2K, Phys. Rev. D 92, 112003 (2015), doi:10.1103/PhysRevD.92.112003

[62] K. Abe, et al. (T2K Collaboration), Measurement of the ν_μ charged current quasielastic cross-section on carbon with the T2K on-axis neutrino beam, Phys. Rev. D 91, 112002 (2015), doi:10.1103/PhysRevD.91.112002

[63] D. Rein and L.M. Sehgal. Neutrino-excitation of baryon resonances and single pion production. Annals of Physics, 133(1):79153, 1981. ISSN 0003-4916. doi: http://dx.doi.org/10.1016/0003-4916(81)90242-6

[64] R.A. Smith and E.J. Moniz. Neutrino reactions on nuclear targets. Nuclear Physics B, 43:605 622, 1972.

[65] P.K.A. de Witt Huberts. Proton spectral functions and momentum distributions in nuclei from high resolution (e, e-prime p) experiments. J.Phys. G16, pp. 507544 (1990), doi:10.1088/0954-3899/16/4/004

[66] A. De R ujula, R. Petronzio, and A. Savoy-Navarro. Radiative corrections to high-energy neutrino scattering. Nuclear Physics B, 154(3):394-426, 1979. ISSN 0550-3213. doi: http://dx.doi.org/10.1016/0550-3213(79)90039-7.

[67] C. Andreopoulos et al. The GENIE Neutrino Monte Carlo Generator. Nucl. Instrum. Meth., A614:87104, 2010. doi: 10.1016/j.nima.2009.12.009.

[68] Y. Hayato. Neut. Nuclear Physics B - Proceedings Supplements, 112(13):171 176, 2002.

[69] C. Juszczak, J. A. Nowak, and J. T. Sobczyk. Simulations from a new neutrino event generator. Nuclear Physics B - Proceedings Supplements, 159(0):211 216, 2006. ISSN 0920-5632. doi: http://dx.doi.org/10.1016/j.nuclphysbps.2006.08.069.

[70] Nuwro, 2014. URL http://borg.ift.uni.wroc.pl/nuwro/.

[71] D. Casper. The NUANCE Neutrino Physics Simulation, and the Future. Nuclear Physics B - Proceedings Supplements, 112(13):161170, 2002. ISSN 0920-5632. doi: http://dx.doi.org/10.1016/S0920-5632(02)01756-5.

[72] O. Buss, T. Gaitanos, K. Gallmeister, H. van Hees, M. Kaskulov, et al., Transport-theoretical description of nuclear reactions, Phys. Rept. 512 1124 (2012), doi:10.1016/j.physrep.2011.12.001

[73] M.M. Block et al., Phys. Lett. 12:281285 (1964).

[74] F. J. Hasert, et. al. Observation of Neutrino-Like Interactions Without Muon Or Electron in The Gargamelle Neutrino Experiment. Physics Letters, Volume 46B, 1973.

[75] Gargamelle Neutrino collaboration, F.J. Hasert et al., Phys. Lett. B46:138140 (1973)

[76] W. Lee et al., Phys. Rev. Lett. 37:186 (1976).

[77] A.C. Benvenuti and e. al., Phys. Rev. Lett. 32:800803 (1974).

[78] E. Pachos, Electroweak Theory, cambridge University Press (2007).

[79] G. Garvey, E. Kolbe, K. Langanke, and S. Krewald, Phys. Rev. C48:19191925 (1993).

[80] L.A. Ahrens et al., Phys. Rev. D 35:785 (1987).

[81] European Muon collaboration, J. Ashman et al., Nucl. Phys. B328:1 (1989).

[82] S. Pate and D. Trujillo. Strangeness Vector and Axial-Vector Form Factors of the Nucleon. arXiv:1308.56694v1 [hep-ph], 2013.

[83] K. Abe, et al., Precision Measurement of the Proton Spin Structure Function g_1^p. Physical Review Letters, American Physical Society, 74, pp.346-350, 1995.

[84] A. A. Aguilar-Arevalo, et al. Measurement of the Neutrino Neutral-Current Elastic Differential Cross Section. arXiv:1007.4730v1 [hep-ex], 2010.

[85] K. Abe, et al. The T2K Experiment. arXiv:1106.1238v2 [physics.ins-det], 2011.

[86] K. Matsuoka, et al. Design and Performance of the Muon Monitor for the T2K Neutrino Oscillation Experiment. arXiv:1008.4077v2 [physics.ins-det], 2010.

[87] P.-A. Amaudruz, et al. The T2K Fine-Grained Detectors. arXiv:1204.3666v1 [physics.ins-det], 2012.

[88] K. Abe et al. (T2K Collaboration), The T2K Experiment, Nucl. Instrum. Meth. A 659, 106 (2011), doi:10.1016/j.nima.2011.06.067

[89] G. Charpak, J. Derre, Y. Giomataris and P. Rebourgeard MICROMEGAS, a multi-purpose gaseous detector, Nucl. Instrum. Meth. A 560, 405 (2006), doi:10.1016/S0168-9002(01)01713-2

[90] N. Abgrall, et al. Time Projection Chambers for the T2K Near Detectors. arXiv:1012.0865v1 [physics.ins-det], 2010.

[91] S. Assylbekov, et al. The T2K ND280 Off-Axis Pi-Zero Detector. arXiv:1111.5030v2 [phyics.ins-det], 2012.

[92] D. Allan, et al. The Electromagnetic Calorimeter for the T2K Near Detector ND280. arXiv:1308.3445v2 [physics-ins.det], 2013.

[93] S. Aoki, et al. The T2K Side Muon Range Detector (SMRD). arXiv:1206.3553v2 [physics.ins-det], 2012.

[94] Y. Fukuda et al. The Super-Kamiokande detector. Nucl. Instrum. Meth., A501:418462, 2003.

[95] L. Radel and C. Wiebusch. Calculation of the Cherenkov Light Yield from Low Energetic Secondary Particles Accompanying High-Energy Muons in Ice and Water with Geant4 Simulations. arXiv:1206.5530v2 [astro-ph.IM], 2012.

[96] http://www-sk.icrr.u-tokyo.ac.jp/sk/detector/display-e.html

[97] M. Mathis. Long term performance of the MINOS calibration procedure and stability of the MINOS detectors. http://iopscience.iop.org/17426596/404/1/012039, 2012

[98] D. Green. The Physics of Particle Detectors. Cambridge University Press, 2000.

[99] Z. Tianafu, et al. The Long-Term Stability of Plastic Scintillator for Electromagnetic Particle Detectors. DOI: 10.7529/ICR2011/V04/0267, 2011.

[100] C. Patrignani et al. (Particle Data Group), Chin. Phys. C, 40, 100001 (2016).

[101] Y. Hatano, Y. Katsumura, A. Mozumber. Charged Particle and Photon Interactions with Matter: Recent Advances, Applications, and Interfaces. CRC Press, 2011.

[102] J. T. Sobczyk. Transverse Enhancement Model and MiniBooNE Charge Current Quasi-Elastic Neutrino Scattering Data. arXiv:1109.1081v1 [hep-ex], 2011.

[103] J. Kim, C. Nielsen M. Wilking. Michel Electron Tagging in the FGDs. `https://t2k.org/docs/technotes/104/michel-electron-tagging-efficiency_v2`. T2K-TN-104, only accessible to T2K collaborators, 2015.

[104] N. Abgrall, et al. (NA61 Collaboration). NA61/SHINE facility at the CERN SPS: beams and detector system. arXiv:1401.4699 [physics.ins-det], 2014.

[105] P.Bartet, et. al. ν_μ CC Event Selections in the ND280 Tracker Using Run 2+3+4 Data. https://t2k.org/docs/technotes/212/tn-212-v-2-1.1. T2KTN-212, only accessible to T2K collaborators, 2015.

[106] D. Ruterbories. Measurement of NCE Production with the T2K π^0 Detector (P0D). https://t2k.org/docs/technotes/131/final. T2K-TN-131, only accessible to T2K collaborators, 2013.

[107] C. Andreopoulos, et. al. The GENIE Neutrino Monte Carlo Generator Physics User Manual. arXiv:1510.05494 [hep-ph], 2015.

[108] A. Garcia, F. Sanchez. Measurement of the Flux Integrated ν_μ Inclusive Charge Current Cross Section in FGD1. https://t2k.org/docs/technotes/310/tn310v1r0. T2K-TN-310, only accessible to T2K collaborators, 2017.

[109] T. Yuan, J. Lopez A. Marino. A Double Differential Measurement of the Flux Averaged ν_μ CC0π Cross Section on Water. https://t2k.org/docs/technotes/258/TN258v4r6p1. T2K-TN-258, only accessible to T2K collaborators, 2016.

[110] F. James. MINUIT Function Minimization and Error Analysis Reference Manual Version 94.1. https://root.cern.ch/download/minuit.pdf.

[111] S. Oser. Elemental Comparison of the FGD XY Modules. https://www.t2k.org/docs/technotes/091/xy-chemcomp-v1.2.pdf. T2K-TN-91, only acessible to T2K collaborators, 2010.

[112] K. Abe, et al. Measurement of Double-Differential Muon Neutrino Charged-Current Interactions on C_8H_8 Without Pions in the Final State Using the T2K Off-Axis Beam. arXiv:1602.03652v2 [hep-ex], 2016.

[113] D. Cox. A Measurement of the Neutral Current Neutrino-Nucleon Elastic Cross Section at MiniBooNE. PhD thesis, Indiana University. http://lss.fnal.gov/archive/thesis/2000/fermilab-thesis-2009-47.pdf, 2008.